DOCTOR OF PHILOSOPHY

Fabrication and Characterisation of 45⁰ and Ex 45⁰

Tilted Fibre Gratings and Their Applications in Fibre Lasers and Sensors

Chengbo Mou

2012

Aston University

Fabrication and Characterisation of 45º and Ex 45º- Tilted Fibre Gratings and Their Applications in Fibre Lasers and Sensors

Chengbo Mou

Doctor of Philosophy

Aston University

February 2012

<center>Aston University</center>

Fabrication and Characterisation of 45º and Ex 45º Tilted Fibre Gratings and Their Applications in Fibre Lasers and Sensors

<center>Chengbo Mou
Doctor of Philosophy
February 2012</center>

In this thesis, I present the studies on fabrication, spectral and polarisation characterisation of fibre gratings with tilted structures at 45º and > 45º (namely 45º-TFGs and ex 45º-TFGs throughout this thesis) and a range of novel applications with these two types of grating.

One of the major contributions made in this thesis is the systematic investigation of the grating structures, inscription analysis and spectral and polarisation properties of both types of TFGs. I have inscribed 45º-TFGs in standard telecom and polarisation maintaining (PM) fibres. Two wavelength regions of interest have been explored including 1.55 μm and 1.06 μm. Detailed analysis on fabrication and characterisation of 45º-TFGs on PM fibres have also been carried out for the first time. For ex 45º-TFGs, fabrication has been investigated only on low-cost standard telecom fibre. Furthermore, thermal responses have been measured and analysed showing that both types of TFG have low responsivity to temperature change. More importantly, their refractive index (RI) responses have been characterised to verify the high responsivity to surrounding medium.

Based on the unique polarisation properties, both types of TFG have been applied in fibre laser systems to improve the laser performance, which forms another major contribution of the research presented in this thesis. The integration of a 45º-TFG to the Erbium doped fibre laser (EDFL) enables single polarisation laser output at a single wavelength. When combing with ex 45º-TFGs, the EDFL can be transformed to a multi-wavelength switchable laser with single polarisation output. Furthermore, by utilising the polarisation property of the TFGs, a 45º-TFG based mode locked fibre laser is implemented. This laser can produce laser pulses at femtosecond scale and is the first application of TFG in the field of nonlinear optics.

Another important contribution from the studies is the development of TFG based passive and active optical sensor systems. An ex 45º-TFG has been successfully developed into a liquid level sensor showing high sensitivity to water based solvents. Strain and twist sensors have been demonstrated via a fibre laser system using both 45°- and ex 45º-TFG with capability identifying not just the twist rate but also the direction. The sensor systems have shown the added advantage of low cost signal demodulation. In addition, load sensor applications have been demonstrated using the 45º-TFG based single polarisation EDFL and the experimental results show good agreement with the theoretical simulation.

Key words: fibre Bragg grating, tilted fibre grating, fibre laser, optical sensor, fibre sensor

Acknowledgments

First of all, I would like to express my deepest gratitude to my supervisor, Prof Lin Zhang, who offered me a great opportunity to do research in the field of optical fibre gratings and kindly guided me throughout my time at Aston University. Her enthusiasm for science and tireless attention to the research have set me an icon and motivated me through out my Ph.D and will inspire me in future. She always gave me a lot of encouragements to my work, especially in some difficult time periods. Because of her recommendation, I was awarded the outstanding overseas student award by the Chinese government, which is the first such an award winner at Aston University. I would like to thank Dr Youfang Hu, Mr Chi Zhang, Prof Tianxin Yang (Tianjin University, China) and Dr Bruce Sinclair (University of St Andrews, UK) who recommend me as a Ph.D candidate to the Photonics Research Group at Aston University.

I would like to thank Dr Xianfeng Chen and Dr Kaiming Zhou, who I have been worked very closely with and helped me to master the fibre grating fabrication and measurement techniques. Their endeavour in research inspired me to study and work hard and learn more knowledge and skills.

I would like to thank Prof Shenghui Fu, Prof Ian Bennion, Dr Xuwen Shu, Dr Wei Zhang, Dr Yicheng Lai, Dr Thomas Allsop, Dr Kalli Kyriacos, Dr Jovanic Petrovich, Dr Amos Martinez, Dr Paul Harper, Dr Rui Suo, Dr Hongyan Fu and Dr Hua Wang for their ideas, fruitful discussion and helps throught my Ph.D. I also would like to thank Dr Pouneh Saffari, Dr Edward Davies, Mr Ian Johnson, Mr Graham Lee, Mr Zhijun Yan and Dr Guchun Zhang who helped and supported me during my study at Aston University.

I would like to thank Dr Kate Sudgen who supported me for part of the studentship during my Ph.D programme.

Particularly, I am deeply grateful to Mr Bert Biggs and Mr Andrew Abbot for their great help in using lab facilities. Without their help, all the labs and experiments could not run so smoothly. My thanks also go to Mrs Helen Yard and Ms Yuen Chu for their kindest support during my study. Overall, I would like to thank all the Photonics Research Group members who create such a great place to work and study.

Finally, I would like to express my deepest gratitude to my parents. They made me the first University student within my whole family. They devotedly supported my undergraduate education in China and postgraduate education in the UK. Their love and spirits always encourage me to be diligent. I also would like to thank all my friends from all over the world for their greatest support and friendship.

<div align="center">CONTENTS</div>

LIST OF FIGURES

Chapter 1

Introduction and Thesis Structure

1.1 Introduction

Following the development of in-fibre Bragg gratings proposed by Hill *et al* in 1978 [1], various fibre components, systems and applications based on such a technology have been investigated and developed. Numerous lightwave applications have been demonstrated using optical fibre grating based optical components such as fibre Bragg gratings (FBGs), long period gratings (LPGs), sampled fibre Bragg gratings (SFBGs) and tilted fibre gratings (TFGs).

Clearly, as an in-fibre reflector, FBGs have found applications in optical filters, signal processing, dispersion management, fibre lasers and smart sensing etc. LPGs have been applied as gain equaliser in Erbium doped fibre amplifiers. SFBGs have been utilised providing access to multichannel filtering and communication source. In recent years, another important application of fibre gratings has been identified, which is the fibre grating based optical sensors.

Various fibre optic sensors have been demonstrated using FBGs and LPGs to monitor and measure a wide range of physical parameters, such as axial strain, temperature, pressure, loading, bending etc. Based on the cladding modes coupling property, LPGs have shown unique sensor functionality in biological, medical and life science areas due to their inherent sensitivity to the refractive index of the external medium. Moreover, the research on new types of gratings and their corresponding applications has never slowed in pace. Compared to the conventional FBGs and LPGs, TFGs are a kind of relatively novel type of grating. These tilted structures are capable of coupling the forward propagating core mode into either forward or backward propagating cladding modes. Their potential applications include spectrum analysis [2], wavelength division multiplexing channel monitoring [3], EDFA gain flattening [4] and optical sensor interrogation systems [5-8]. Due to grating induced asymmetry of waveguide structures, TFGs normally exhibit a certain amount of polarisation dependency. With this unique property, various polarimetry device and systems have been implemented, i.e. in fibre polarimeter [9-10], polarisation dependent loss equaliser [11-12], in-fibre polariser [13] and various sensors [14-15].

Nevertheless, more systematic investigation of TFGs especially gratings tilted at 45º and >45º are less common. This thesis summarises the work carried out for

fabrication, characterisation and application of 45°-TFGs and ex-45° TFGs. It presents detailed information on the inscription technique, spectral characteristics and polarisation properties. Inscription of both types of gratings in conventional single mode fibres have been conducted. For 45°-TFGs, inscription in both photosensitive and polarisation maintaining fibres has also been studied. This thesis firstly discloses the application of 45°-TFG and ex-45° TFG in fibre laser systems. Both continuous wave and pulse regimes have been covered. Furthermore, the roles of 45°-TFGs and ex 45°-TFGs in optical sensor systems have been investigated and presented.

1.2 Overview of Thesis Structure

This thesis consists of 6 chapters and detailed contents are listed below:

Chapter 1 briefly mentions the development of in-fibre grating technologies and illustrates the motivation for the work carried out for my Ph.D research, followed by the thesis structure description.

Chapter 2 serves as the literature review of the theoretical background of fibre grating technologies. This chapter reviews the photosensitivity theory of optical fibres followed by fundamental coupled-mode theory of fibre gratings including FBG, LPG and TFG. Recently developed Green function method for explaining TFG has been briefly reviewed. Subsequently, major grating fabrication techniques have been introduced followed by a general description of the fibre grating applications.

Chapter 3 details the inscription and characterisation of both 45° and ex- 45° TFGs. Comprehensive analysis of the 45°-TFG inscription has been provided. A detailed report of the polarisation properties of both types of gratings is provided in this chapter. The grating reproducibility, thermal characteristics and refractive index responses are presented. Furthermore, the investigation of inscription of 45°-TFGs at 1.06 μm region and in standard photosensitive, non-photosensitive and polarisation maintaining fibres with results on polarisation dependent loss and spectral characteristics have been given.

Chapter 4 introduces the application of 45º and ex-45º TFGs in fibre lasers. With the application of the polarisation property of TFGs, various novel laser configurations have been developed, such as single-polarisation single-wavelength fibre laser and single-polarisation switchable multiwavelength fibre laser. Furthermore, a mode locked fibre laser using 45º-TFG has been demonstrated which deems to be the first demonstration of application of tilted gratings in nonlinear science. The laser can give out femtosecond scale pulses.

Chapter 5 reports the application of 45º and ex-45º TFGs in optical fibre sensors. A passive liquid level sensor has been implemented using an ex-45º TFG. Then, fibre laser consists of an ex-45º TFG has been used as both strain sensor and twist sensor with further demonstration of low cost time domain signal demodulation method to interrogate the sensing signals. Finally, a loading sensor was described using a 45º-TFG based fibre laser.

Chapter 6 presents concluding remarks of this thesis and suggestions for future work. Finally, appendix with fibres used in this thesis followed by a list of reference and publications are presented.

Chapter 2

Review-Theory, Fabrication Methods and Applications of Fibre Gratings

2.1 Introduction

This chapter will introduce the fundamental theoretical background, fabrication methods and applications of fibre gratings. The photosensitivity of optical fibre will be reviewed in the beginning of this chapter describing the mechanism of photosensitivity and methods for photosensitisation of optical fibres. After that, the coupled mode theory explaining the physics of FBG and TFGs will be given. Specifically, Green function method, as an alternative interpretation, will be employed to explain the behaviour of the TFGs, followed by the discussion on phase matching condition for the mode coupling mechanism of fibre gratings. Subsequently, a brief summary of fibre grating inscription techniques will be discussed, including two-beam holographic, phase mask scanning and point-by-point technique. Finally, a short review of applications of fibre gratings will be presented followed by the conclusion of this chapter.

2.2 Photosensitivity in Optical Fibres

Photosensitivity generally indicates the chemical reaction, photoelectric reaction etc. undergoing when the matter expose to light energy. In optical fibres, photosensitivity mainly refers to the permanent change of refractive index in optical fibre resulting from UV radiation on the fibre core. The very first observation of photosensitivity in germanosilicate (Ge-Si) doped optical fibre was reported by Hill *et al* in 1978 [1]. Hill *et al* have also implemented a distributed feedback gas laser operating in the visible range of the optical spectrum with UV formed FBG. Since then, a couple of theories were reported to elucidate the mechanism. It has been found that the photosensitivity has dependency on wavelength and intensity of the irradiated light and the fibre core material. So far, there is still no sole model which could explain the phenomenon for all cases. The following sections will introduce the major theories of photosensitivity and routes to achieve photosensitivity enhancement.

2.2.1 Point Defects

Point defects are critical to optical fibres as they are strongly associated with the absorption band which may affect the transmission loss, nonlinear transmission [16-17] and fibre fusing effect [18]. The defects are also believed to be the cause for the

photosensitivity phenomenon (colour centre model [19]) which will be discussed in the photosensitivity mechanism section.

2.2.1.1 Point Defects in Silica Glass

The point defect of amorphous silica was firstly reported by Weeks in 1956 via the observation of narrow resonance in neutron irradiated quartz and silica using electron spin resonance (ESR) spectroscopy [20]. The E' centre was then identified [21]. By using ESR, Griscom pointed out three intrinsic defects in silica which are nonbonding Oxygen hole centre, peroxy radical and E' centre [22]. Several prominent absorption bands related to the intrinsic defects have been identified such as 180 nm (7.6eV), 173 nm (7.2eV), 215 nm (5.8eV), 245 nm (5eV), 260 nm (4.8eV). It is also well known that fibre drawing induced defect has a characteristic absorption band at 630nm (2eV) [23].

2.2.1.2 Point Defects in Germanosilicate Fibres

Early investigation on defect centres in germanosilicate fibres was carried out by Friebele *et al* in 1974 through ESR [24]. This primary experiment proposed the so called Ge(n) defect centres in addition to the well known SiE' centres. Three absorption bands in germanosilicate fibres have been presented at 213 nm(5.8eV), 281 nm (4.4eV) and 517 nm(2.4eV) whereby the 213 nm and 281 nm bands have been assigned to Ge(1) and Ge(2) centres respectively [25]. Recently, Hosono *et al* correlated the 195 nm (6.3eV) absorption band to GeE' centre in germanosilicate glass using a ArF laser [26]. It is noticed that Germanium is well known for its two stable oxides GeO and GeO_2. Thermodynamic prediction anticipates the Germanium Oxygen deficiency defects (GODC) centres are proportional to the concentration of GeO_2. The suboxide GeO, stable at high temperature, may also exist as discrete molecules which was originally assigned to explain the strong UV absorption at 240nm [27]. It is believed that the breakage of wrong bonds is the precursor of GeE' defect centre. The schematic description of various GODC candidates is presented below in Figure 2.1.
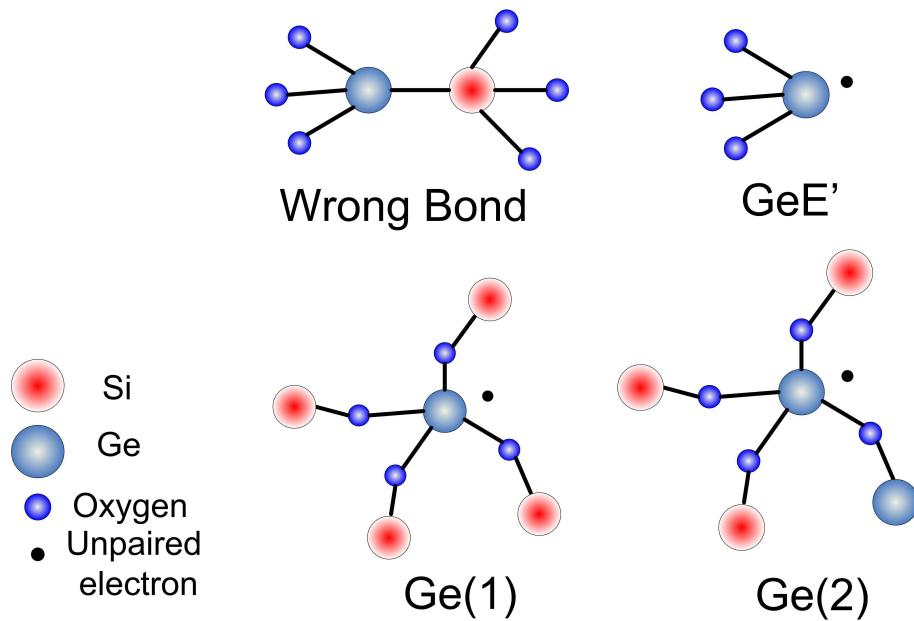
Figure 2.1 Potential GODC varieties.

2.2.2 Photosensitivity Mechanisms

To date, various models have been established to explain photosensitivity phenomenon, such as ionic migration [28-29], electron charge migration [30], stress relief [31], permanent electric dipole [32], colour centre [19] and compaction/densification [33]. Among these, colour centre model and compaction/densification model are the two commonly accepted mechanisms of illustrating the photosensitivity in germanosilicate fibres. In this section, stress-relief model has also been briefly reviewed in the end.

2.2.2.1 Colour Centre Model

The colour centre model, initially proposed by Hand and Russell [19], states that a two-photon absorption (TPA) induced GODC (Ge-Si wrong bond in this case) breakage is related with the refractive index change in the germanosilicate fibres. The Ge-Si bond breakage partially bleaches out the UV absorption at 240 nm in the fibre. The free electrons produced by this effect can be trapped at other defect sites thus manifesting defect centres at longer wavelength (i.e. Ge(1)) and stronger transition (i.e. Ge(2)) with newly formed absorption band at 281 nm and 213 nm individually. The corresponding photo induced refractive index change follows the Kramers-Kronig principle [34], expressed as following in Equation 2.1.

Equation 2.1 $\Delta n_{eff}(\omega) = \dfrac{2 \cdot c}{\pi} \cdot \displaystyle\int_0^\infty \dfrac{\Delta \alpha_{eff}(\omega')}{\omega'^2 - \omega^2} d\omega'$

Where $\Delta n_{eff}(\omega)$ is the effective refractive index change at frequency ω which is far from resonance, $\Delta \alpha_{eff}(\omega')$ is the effective change of absorption. The model demonstrated that the absorption change at 213 nm, 240nm and 281 nm bands can be used to explain and fit the refractive index change in the visible spectrum in the optical fibre under UV illumination. This model, describing the Ge-Si wrong bond breakage results in a change in absorption spectrum owing to the newly formed GeE' centre, has been supported by various experimental measurements after its debut. Simmons *et al* [35] demonstrated a similar wavelength-dependent response for production of GeE' centres and formation of Bragg gratings in germanosilicate fibres. Williams *et al* [36] reported the observation of UV bleached 240 nm absorption band in germanosilicate fibres and correlated the corresponding refractive index change via the Kramers-Kronig relationship. Further evidence on refractive index change related with absorption change was carried out by direct observation of 240 nm band bleaching under UV illumination in germanosilicate fibres [36] and UV irradiation induced UV spectral change in germanosilicate fibre preform [37-38]. Both experimental data were well fitted through the Kramers-Kronig principle. Additionally, Tsai *et al* [39] experimentally correlated the thermal stability of GeE' centres and grating reflectivity indicating that GeE' is related with the refractive index change in UV induced gratings. While Dong *et al* [40] performed a comprehensive examination of the photoinduced absorption change in germanosilicate preform providing support evidence to the colour centre model which can explain refractive index as high as $\sim 3 \times 10^{-4}$. The colour centre model utilising the Kramers-Kronig principle provides great contributions in understanding the photosensitivity in germanosilicate fibres including the photosensitivity in Hydrogen loaded germanosilicate fibres. Tsai *et al* reported the contribution of GeH centre in refractive index change during FBG formation in Hydrogen loaded germanosilicate fibres using colour centre model [41]. Leconte *et al* [42] demonstrated a modified Kramers-Kronig analysis describing the

refractive index change as a function of pulse energy density. However, it does not explain all the experimental observations especially for large value refractive index change [43-45].

2.2.2.2 Compaction/Densification Model

The compaction/densification model manifests the laser irradiation induced material density change leading to refractive index change of optical fibres. Fiori & Devine [33, 46] firstly presented that the existence of thermally reversible linear compaction in a 100 nm thin-film amorphous silica samples grown on Si wafers. Using a KrF excimer laser irradiation to examine the sample below the macroscopic damage threshold, the thickness is found to reduce by ~16%. A linear increase in refractive index up to 20% has also been observed in the meantime. After annealing at 950 ℃ for ~1hour in vacuum, the sample restored to its original thickness and refractive index value. This had been proved to be a general case for film thickness from 25 nm to 420 nm. Further exposure can result in irreversible compaction of the material. The obtained maximum compaction of ~ 36 % of the sample exhibits similarity to sample under hydrostatic pressure of 17 GPa. It also shows many physical characteristics resemble high density crystalline form of silica. Fiori & Devine demonstrated that the refractive index evolution of silica under hydrostatic pressure leads to good agreement with laser treated silica sample [46]. This indicates that the compaction induced by two different methods may share similar physical mechanism from which internal structure rearrangement in the material dominates the effect and not primarily through defect creation process. Rothschild et al [47] identified the laser induced microscopic volume change and colour centre absorption in fused silica at 193 nm irradiation. A permanent refractive index change of ~ 5×10^{-5} was observed regardless of the absorption due to the colour centre at 215 nm. Allan et al [48] reported an elastic theory model to characterise the intrinsic densification of fused silica implied by excimer laser at 193nm.

The knowledge of compaction/densification in bulk fused silica opens the access to understand the refractive index change mechanism during the formation of fibre gratings. Poumellec et al [49] investigated the Bragg grating inscription in germanosilicate preform via interferometric microscopy. The refractive index modulation shows similar behaviour for both the fibre and preform. The conclusion is

that densification via the UV inscription could contribute ~ 7% of the refractive index increase of the sample. Using atomic force microscopy, Poumellec *et al* [50] also shows ~26% of refractive index increase of the germanosilicate preform sample can be counted as densification under CW UV radiation for Bragg grating inscription. Cordier *et al* [51] presented the first observation of densification by FBGs via transmission electron macroscopy. The results show that UV irradiated sections of nonhydrogenated germanosilicate fibre and Sn co-doped fibre exhibit dense areas inducing from the UV compaction. Hydrogenated fibre samples do not present densification. This suggests that photosensitivity enhancement in hydrogenated fibre is not mainly due to the densification of the optical fibre. Meanwhile, Sn co-doped fibre samples manifest a less densification than germanosliciate fibres. Fonjallaz *et al* [52] reported the UV induced tension increase during the inscription of FBG does not reduce the refractive index due to a large refractive index increment from possible glass matrix compaction. Limberger *et al* [53] quantified the stress and compaction induced refractive index change during the process of UV inscribed FBG. Their experimental results indicated that the compaction could raise the refractive index as large as 1.7×10^{-3} in a 12 % Germanium doped fibre from which this value is reduced by the photoelastic effect through the UV irradiation. A comprehensive review of densification involved photosensitivity in optical fibres is given by Douay *et al* [54].

2.2.2.3 Stress-relief Model

In a typical germanosilicate fibre, because of the difference of the thermal expansion of the core and cladding, the core is under higher tensile stress as the fibre is cooled below the glass fictive temperature during the drawing procedure. It is well known that the refractive index will decrease through the stress-optic effect while stress-relief would, on the contrary, increase the refractive index. The postulation based on reduction of built-in thermo-elastic stress in the fibre core for explaining UV induced refractive index increase is called stress-relief model. It was first reported by Sceats *et al* [55] that during the UV irradiation, the wrong bonds breakage occurs to allow sufficient thermal energy to dilate the glass network so as to relax the tension therefore reducing the frozen-in stress in the fibre core. Considering the bonds have been stretched, this leads to a change in the electronic band gap in glass hence resulting in change in the refractive index. This index change could then be illustrated

by Kramers-Kronig relation. Further calculation of refractive index change based on stress-relief can be described by stress-optic effect. It is demonstrated that the refractive index change can be as high as 10^{-3} in a highly stresses fibre. This model has been experimentally proved by Wong *et al* [31]. However, Fonjallaz *et al* [52] and Limberger *et al* [53] later reported observation of a strong increase in the fibre tension during the UV inscription process which contradicts the model.

2.2.3 Photosensitivity Enhancement of Optical Fibres

Since the discovery of photosensitivity and realisation of fibre gratings in germanosilicate fibres, exceptional efforts have been made to enhance the photosensitivity in optical fibres. Three major techniques have been considered as the effective approaches to increase the photosensitivity in optical fibres including Hydrogen loading [56], co-doping [57], and flame brushing [58], which will be reviewed in this section. A recently reported photosensitivity increase by thermal treatment has also been briefly introduced [59].

2.2.3.1 Hydrogen Loading

Hydrogen loading, also known as hydrogenation, was firstly reported by Lemaire *et al* [56]. This simple technique provides a highly effective way to enhance UV photosensitivity in optical fibres by employing low temperature, high pressure Hydrogen loading prior to grating fabrication. It does not require fibres with specific dopants or other special treatment. The temperature for soaking the fibres in Hydrogen gas ranges from ~21 ℃ to ~75℃ with pressures from ~20 atm to ~750 atm. This results in Hydrogen molecules diffusing into the fibre core area to achieve at least 95 % of equilibrium when giving enough time for the soaking. The consequent average refractive index change of Hydrogen loaded optical fibre (standard fibre with ~3 mol% germania and ~3.3 mol% Hydrogen) under UV exposure can increase by ~3.4×10^{-3}. Large index increment has also been observed in heated Hydrogen loaded phoshosilicate and alumnio-phosphosilicate core fibres. Almost every Hydrogen molecule interacts with each Germanium atom via UV light or thermal treatment via the OH absorption. This has also been proved to be independent on fibre or preform processing with similar germania concentration and could be applicable to any germanosilicate fibres. Loading phosphor-doped fibre with D2 (deuterium) and

applying thermal treatment proved the photosensitivity at 248 nm in this fibre for the first time [60]. Results have shown that due to the diffusion of molecular Hydrogen, there will be absorption peak at 1.24 µm when the fibres had been exposed to 1 atm pressure at 100 ºC [61]. One advantage of this method is in the non-UV exposed sections of the fibre, the residual Hydrogen can be diffused out afterwards leaving negligible loss at the telecom transmission band.

Atkins *et al* have confirmed that thermal and photolytic treatment of the fibre can increase the OH level compared to photolytic treated only sample, for which no OH formation had been observed when using non-hydrogenated fibres under similar exposed conditions [62]. A simple mechanism to explain the photosensitivity is the forming of the GODC centres (240 nm band) via thermal treatment followed by UV bleaching of the GODC centres. However, other observations suggest that a more complex model might be required. In the beginning, the 240 nm band gets stronger (~ 6 times) after thermally anneal a UV-radiated hydrogenated fibre sample at 800 °C while the non-hydrogenated sample only shows 240 nm band recovery to a lower or equal level of the sample prior to the UV treatment. Then, rapid and complete UV bleaching of the 240 nm band only occur in the hydrogenated sample indicates direct reaction of the Hydrogen with the defects. Moreover, hydrogenation induced OH formation was shown to introduce two closely spaced absorption bands which are 1390 nm (Si-OH) and 1410 nm (Ge-OH) due to the involvement of both thermal and photolytic mechanisms [61, 63]. These two loss bands obviously generate extra losses in the modern telecom network window which is unwanted. Nevertheless, it has been found that deuterium loaded optical fibre could shift the UV-induced absorption band out of the telecom band. This is due to the OD (Oxygen deuterium) can shift the water absorption peak to ~ 1.9 µm [64]. Mizrahi *et al* have successfully demonstrated ~ 10 nm wide Bragg grating in a deuterium loaded Erbium doped fibre with high Germanium concentration. The gratings exhibited low loss i.e. < 0.2 dB at the designated wavelength region [65]. However, practically speaking, the cost of deuterium in enhancing photosensitivity limits its application.

2.2.3.2 Co-Doping

Photosensitivity enhancement can be achieved by addition of other co-dopants into the germanosilicate fibre. A practical and widely used type of photosensitive fibre is

Boron-Germanium co-doped fibre. Williams *et al* [57] firstly reported that after CW argon ion laser irradiation, the Boron co-doped fibre (~15 mol% Ge) has a saturated index modulation of ~7×10^{-4} which is much higher than that of the standard fibre (~4mol% Ge) and high index fibre (~20 mol% Ge) from which the saturated index modulations are 3.4×10^{-5} and 2.5×10^{-4} respectively. Furthermore, the saturated index change was achieved much quicker in Boron co-doped fibres (~10 mins) compared to that in other type of fibres (>1hour). This suggests other mechanism exists for photosensitivity enhancement in Boron-Germanium co-doped fibres. UV absorption experiments confirm that the characteristic GODC absorption peak at 240 nm is independent of the involvement of Boron co-dopant. Neither the peak absorption nor the shape of the 240 nm band has been affected. This indicates that the Boron co-dopant does not increase the photosensitivity by introducing extra GODC centres. This is supported by the fact that no other absorption peaks were observed in the UV region.

It is well known that the introduction of Boron to silica glass can decrease the refractive index [66]. As such, Boron is normally added to the fibre cladding to form the waveguide with lower refractive index cladding area surrounding the high refractive index core region [67-68]. Experimental results state that lower refractive index in Boron doped silica glass can be obtained when the glass is quenched. Observation of refractive index drop from 0.025 to 0.003 was obtained when the preform was drawn into the optical fibre [57]. This can be well explained by the quenching effect because the drawing procedure induces natural quench of the optical fibres. The large difference in terms of thermo-mechanical properties between the Boron-doped fibre core and silica cladding may result in building-up of the thermo-elastic stress which could further reduce the refractive index of the fibre core. Therefore, it is believed that the stress relaxation of UV induced wrong bonds breaking gives out refractive index increase leading to photosensitivity enhancement in Boron-Germanium co-doped fibres [52].

By balancing the Boron and Germanium concentrations, fibre suppliers are able to manufacture Boron-Germanium co-doped ultra-photosensitive fibres with matched numerical aperture to standard telecom fibres. However, owing to the co-doping of Boron, the co-doped fibres may exhibit an increase of birefringence by the Boron

induced stress resulting in difficulties in manufacturing the fibres [69]. Gratings written with CW lasers in Boron-Germanium (B-Ge) co-doped fibres also have a faster decay rate than low Germanium doped fibres [70]. Moreover, Boron induced loss (~0.1 dB/m) at 1550nm telecom window is also undesirable. However, for short gratings, this may not be of concern.

As an alternative dopant, Tin can increase the photosensitivity with similar saturated refractive index change as of B-Ge co-doped. The reported experimental results indicate that Sn-Ge fibres based gratings exhibit similar thermal stability to germanosilicate fibre which is much more stable than B-Ge co-doped fibres. The negligible transmission loss at telecom window is another advantage of the Sn-Ge co-doped fibre. The deduced refractive index change ($\sim1.4\times10^{-4}$) from inscribing a grating into such fibres shows 3 times larger refractive index change than in pure germanosilicate fibres [71]. Recently, K Oh *et al* [72] showed that Sb co-doped gernamosilicate optical fibre can exhibit ultra high photosensitivity compareable to B-Ge co-doped fibre with higher thermal stability. The UV induced refractive index change more than 5×10^{-4} can be obtained. However, such fibres tend to produce high transmission loss (~5dB/m) at the telecom window region.

2.2.3.3 Flame Brushing

Another simple and effective technique for photosensitising optical fibres is flame brushing [58]. This technique was reported almost at the same time as the Hydrogen loading method. At the temperature of approximate 1700 ºC, the photosensitivity enhancement can be obtained through flame brushing at the designated region of optical fibre by a flame fuelled with Hydrogen and a small amount of Oxygen. The whole process takes ~ 20 mins to finish photosensitisation with a maximum effect under the laboratory condition. The high temperature allows Hydrogen to diffuse into the fibre core quickly forming GODC defect centres. A strong absorption band at 240nm has been therefore created with enhancement of the photosensitivity of the fibre core area. This method has been proved to enhance the photosensitivity of standard telecom fibre by a factor of 10, resulting in refractive index changes of 1.7×10^{-3} from which only 1.6×10^{-4} refractive index change can be obtained in the standard telecom fibre under the same UV fabrication condition. This technique also benefits from negligible low loss at the desired telecom transmission window.

The photosensitivity enhancement techniques of both flame brushing and hydrogenation basically share the same principle. Under both situations, Hydrogen is adopted as an active medium in a chemical reaction with optical fibres to form the GODC centres. Nevertheless, flame brushing offers permanent enhancement of photosensitivity, whereas in hydrogenation, the Hydrogen diffusion could reverse the photosensitisation process. Furthermore, as high temperature treatment is necessary for flame brushing, the fibre may suffer material weakening which could seriously limit the application of the devices for long term usage.

2.2.3.4 Thermal Treatment of Co-doped Fibre for Photosensitivity Enhancement

Very recently, Brambilla and Pruneri [59] reported enhanced photosensitivity in silicate optical fibres with various co-dopants by thermal treatments. The sample fibres were heated at 1800 °C in a furnace for 1 min followed by rapidly cooling down at room temperature. A pulsed KrF laser radiated at 248 nm was adopted to inscribe gratings in order to test the photosensitivity enhancement after the thermal treatment. This method shows large refractive index change in most of the Germanium or Tin co-doped silica fibres. With Germanium and Tin co-doped fibre, the UV induced refractive index change can be obtained as large as $\sim 1.48 \times 10^{-3}$. This is mainly because at high temperature, complicated chemical reactions facilitate the formation of GODC centres and other defects which will be then frozen in the glass network after cooling to room temperature therefore increase the UV absorption. UV absorption spectrum indicates the appearance of SnODC centres in fibre preform. This gives hint that SnODC could undergo similar effects as for GODC. However, this implementation does not seem to work with Ce and rare earth co-doped optical fibres.

2.3 Fibre Grating Theory

Theoretical analysis of fibre gratings is important for understanding and designing the gratings. Various mathematical treatments have been developed to model the grating behaviour. Coupled mode theory (CMT) is a widely adopted method to solve the problems [73-76]. This approach represents the grating behaviours via solving a set of first-order differential equations. Yamada *et al* [77] proposed a simulation technique using the transfer matrix. The principle of this method is to consider any grating

structure as a concatenation of definite small sections of uniform gratings therefore offering a fast and simple analysis tool for complex grating structures. Weller-Brophy and Hall [78] applied a technique presented by Rouard [79] for multilayer dielectric thin film to simulate fibre gratings. However, this method can not meet the need of modelling arbitrary refractive index modulation shape. Another alternative approach to grating simulation is Bloch wave method [80] which gives the exact eigenmodes solutions of the grating structure. In this section, CMT will be reviewed to interpret the grating behaviour. The derivations follow the work done by Erdogan [75]. Green function for modelling tilted grating will also be briefly reviewed at the end of this section.

2.3.1 Coupled Mode Theory

In an ideal case, the transverse component of the electric field of the propagating mode in an optical fibre can be written as a superposition of modes labelled with μ. Without any perturbation i.e. index modulation in a fibre grating or other non-uniformity, the electric field is shown as following:

Equation 2.2 $\vec{E}_t(x, y, z, t) = \sum_{\mu} \left[A_{\mu}(z) \cdot e^{i \cdot \beta_{\mu} \cdot z} + B_{\mu}(z) \cdot e^{-i \cdot \beta_{\mu} \cdot z} \right] \cdot \vec{e}_{\mu t}(x, y) \cdot e^{-i \cdot \omega \cdot t}$

where $A_{\mu}(z)$ and $B_{\mu}(z)$ are slowly varying field amplitudes of the μ th mode propagating along the z direction forward and backward, individually. The transverse mode field $\vec{e}_{\mu t}(x, y)$ represents the bound-core, radiation mode or cladding mode. While in an ideal waveguide, the modes are orthogonal so that no energy exchange occurs. Nevertheless, the presence of a dielectric perturbation can facilitate the modes to couple such that A_{μ} and B_{μ} of the μ th mode evolve along the z axis according to:

Equation 2.3 $\frac{dA_\mu}{dz} = i \cdot \sum_\upsilon A_\upsilon \cdot (K^t_{\upsilon\mu} + K^z_{\upsilon\mu}) \cdot e^{i \cdot (\beta_\upsilon - \beta_\mu) \cdot z} + i \cdot \sum_\upsilon B_\mu \cdot (K^t_{\upsilon\mu} - K^z_{\upsilon\mu}) \cdot e^{-i \cdot (\beta_\upsilon + \beta_\mu) \cdot z}$

Equation 2.4 $\frac{dB_\mu}{dz} = -i \cdot \sum_\upsilon A_\upsilon \cdot (K^t_{\upsilon\mu} - K^z_{\upsilon\mu}) \cdot e^{i \cdot (\beta_\upsilon + \beta_\mu) \cdot z} - i \cdot \sum_\upsilon B_\mu \cdot (K^t_{\upsilon\mu} + K^z_{\upsilon\mu}) \cdot e^{-i \cdot (\beta_\upsilon - \beta_\mu) \cdot z}$

In Equation 2.3 and Equation 2.4, $K^t_{\upsilon\mu}$ stands for the transverse coupling coefficient between modes μ and υ given by:

Equation 2.5 $K^t_{\upsilon\mu}(z) = \frac{\omega}{4} \cdot \iint_\infty dx \cdot dy \cdot \Delta\varepsilon(x, y, z) \cdot \vec{e}_{\upsilon t}(x, y) \cdot \vec{e}^*_{\mu t}(x, y)$

Where $\Delta\varepsilon$ is the perturbation of the permittivity which roughly equals $2 \cdot n \cdot \delta n$ when assuming $\delta n \ll n$. $K^z_{\upsilon\mu}$, the longitudinal coupling coefficient, generally obeys $K^z_{\upsilon\mu} \ll K^t_{\upsilon\mu}$ hence can usually be ignored.

For most UV inscribed gratings, the refractive index modulation can be expressed as:

Equation 2.6 $\delta n_{eff}(z) = \overline{\delta n}_{eff}(z) \cdot \left[1 + v \cdot \cos\left[\frac{2\pi}{\Lambda} \cdot z + \phi(z) \right] \right]$

Where $\overline{\delta n}_{eff}(z)$ is the "dc" index variation spatially averaged over the grating period, v is the fringe visibility of the index variation, Λ is the grating period and $\phi(z)$ indicates the grating chirp.

For most fibre gratings considered, the UV induced refractive index change $\delta n(x, y, z)$ can be regarded as uniform across the whole core area. Therefore, the core index $\overline{\delta n}_{eff}(z)$ can be replaced by $\overline{\delta n}_{co}(z)$. Similar to Equation 2.6, we can write the

coupling coefficient as:

Equation 2.7 $K_{\upsilon\mu}^{t}(z) = \Gamma_{\upsilon\mu}(z) + 2 \cdot \kappa_{\upsilon\mu}(z) \cdot \cos\left[\dfrac{2\pi}{\Lambda} \cdot z + \phi(z)\right]$

Where the following definition applies, $\Gamma_{\upsilon\mu}(z)$ is the "dc" coupling coefficient and $\kappa_{\upsilon\mu}(z)$ is the "ac" coupling coefficient.

Equation 2.8 $\Gamma_{\upsilon\mu}(z) = \dfrac{\omega \cdot n_{co}}{2} \cdot \overline{\delta n}_{co}(z) \cdot \displaystyle\iint_{core} dx \cdot dy \cdot \vec{e}_{\upsilon t}(x,y) \cdot \vec{e}^{\,*}{}_{\mu t}(x,y)$

Equation 2.9 $\kappa_{\upsilon\mu}(z) = \dfrac{v}{2} \cdot \Gamma_{\upsilon\mu}(z)$

2.3.1.1 Bragg Gratings

For a uniform Bragg grating, the schematic of mode coupling is shown in Figure 2.2. The mode coupling occurs at phase match wavelength for which a forward propagating mode with amplitude $A(z)$ reflects into an identical backward propagating mode with amplitude $B(z)$.
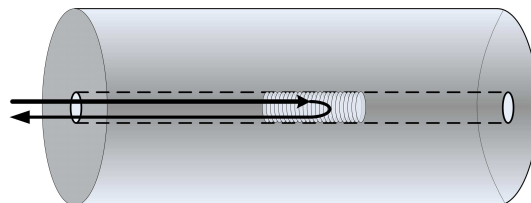
Figure 2.2 Schematic of mode coupling of an FBG, showing light coupled from forward-propagating core mode to backward-propagating core mode.

With this in mind, Equation 2.3 and Equation 2.4 can be simplified to the following expressions [75]:

Equation 2.10 $\dfrac{dA^+}{dz} = i \cdot \Gamma^+ \cdot A^+(z) + i \cdot \kappa \cdot B^+(z)$

Equation 2.11 $\dfrac{dB^+}{dz} = -i \cdot \Gamma^+ \cdot B^+(z) - i \cdot \kappa^* \cdot A^+(z)$

Where the amplitudes are defined as:

Equation 2.12 $A^+(z) = A(z) \cdot e^{i \cdot \delta \cdot z - \frac{\phi}{2}}$

Equation 2.13 $B^+(z) = B(z) \cdot e^{-i \cdot \delta \cdot z + \frac{\phi}{2}}$

The coupling coefficient is given by :

Equation 2.14 $\Gamma^+ = \delta + \Gamma - \dfrac{1}{2} \cdot \dfrac{d\phi}{dz}$

While the detuning is shown as:

Equation 2.15 $\delta = \beta - \dfrac{\pi}{\Lambda} = \beta - \beta_D = 2 \cdot \pi \cdot n_{eff} \cdot \left(\dfrac{1}{\lambda} - \dfrac{1}{\lambda_D} \right)$

In Equation 2.15, $\lambda_D = 2 \cdot n_{eff} \cdot \Lambda$ is the design Bragg reflection peak for an infinitesimally weak index of refraction change grating i.e. $\delta n_{eff} \rightarrow 0$. For a single mode Bragg grating, the coupling coefficients can be simplified as following:

Equation 2.16 $\Gamma^+ = \dfrac{2\pi}{\lambda} \cdot \overline{\delta n}_{eff}$

Equation 2.17 $\kappa = \kappa^* = \dfrac{\pi}{\lambda} \cdot v \cdot \overline{\delta n}_{eff}$

For a grating with uniform structure along the z direction, δn_{eff} is constant and $\dfrac{d\phi}{dz} = 0$ for grating without any chirp. Hence, the coupling coefficients are all constants. Equation 2.10 and Equation 2.11 can then evolve into first order ordinary differential equations. For a uniform fibre grating with a length L, the reflectivity can be calculated from the equation below:

Equation 2.18 $R = \dfrac{\sinh^2 \sqrt{(\kappa \cdot L)^2 - (\Gamma^+ \cdot L)^2}}{-\left(\dfrac{\Gamma^+}{\kappa}\right)^2 + \cosh^2 \sqrt{(\kappa \cdot L)^2 - (\Gamma^+ \cdot L)^2}}$

The maximum reflectivity occurs when $\Gamma^+ = 0$ where

Equation 2.19 $R_{max} = \tanh^2(\kappa \cdot L)$

The bandwidth of a uniform FBG is defined by the wavelength difference between the first minimum on either side of the maximum reflectivity. The bandwidth is then given by :

Equation 2.20 $\frac{\Delta\lambda}{\lambda} = \frac{v \cdot \overline{\delta n_{eff}}}{n_{eff}} \cdot \sqrt{1 + \left(\frac{\lambda_D}{L \cdot v \cdot \overline{\delta n_{eff}}}\right)^2}$

In the weak grating condition where $v \cdot \overline{\delta n_{eff}}$ is very small, we can then infer

Equation 2.21 $\frac{\Delta\lambda}{\lambda} \cong \frac{\lambda_D}{n_{eff} \cdot L}$

The bandwidth of a weak grating is then correlated with the grating length. In the case of strong grating condition where $v \cdot \overline{\delta n_{eff}}$ is large enough, the bandwidth can be obtained as:

Equation 2.22 $\frac{\Delta\lambda}{\lambda} \cong \frac{v \cdot \overline{\delta n_{eff}}}{n_{eff}}$

It can be clearly seen that in strong grating condition, the bandwidth is independent of the grating length. Physically speaking, the incident beam may not propagate through the whole length of the grating as the mode complete Bragg diffraction may finish before it penetrate the full length.

2.3.1.2 Long Period Gratings

For long period gratings (LPG), also known as transmission gratings, the mode coupling occurs close to the wavelength at which a forward propagating mode with amplitude $A_1(z)$ is strongly coupled into a co-propagating cladding mode with amplitude $A_2(z)$. Figure 2.3 shows the mode coupling scheme of a standard LPG.
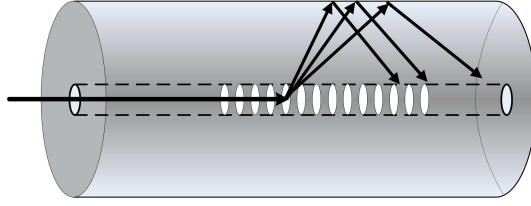
Figure 2.3 Schematic of mode coupling of an LPG, showing the light couples from forward-propagating core mode to co-propagating cladding modes.

Therefore, Equation 2.3 and Equation 2.4 can be simplified by retaining terms that only involve in the coupling behaviour of these two modes. Applying the usual synchronous approximation, the coupled mode equations now evolve into:

Equation 2.23 $\dfrac{dA^+}{dz} = i \cdot \Gamma^+ \cdot A^+(z) + i \cdot \kappa \cdot B^+(z)$

Equation 2.24 $\dfrac{dB^+}{dz} = -i \cdot \Gamma^+ \cdot B^+(z) + i \cdot \kappa^* \cdot A^+(z)$

Where the new mode amplitudes defined as:

Equation 2.25 $A^+(z) = A_1 \cdot e^{-i \cdot (\Gamma_{11}+\Gamma_{22}) \cdot \frac{z}{2}} \cdot e^{i \cdot \delta \cdot z - \frac{\phi}{2}}$

Equation 2.26 $B^+(z) = A_2 \cdot e^{-i \cdot (\Gamma_{11}+\Gamma_{22}) \cdot \frac{z}{2}} \cdot e^{-i \cdot \delta \cdot z + \frac{\phi}{2}}$

In Equation 2.25 and Equation 2.26, Γ_{11} and Γ_{22} are the "dc" coupling coefficients defined in Equation 2.8. $\kappa = \kappa_{21} = \kappa_{21}^*$ is the "ac" coupling coefficient with which the general coupling coefficient can now be written as:

Equation 2.27 $\Gamma^{+} = \delta + \dfrac{\Gamma_{11} + \Gamma_{22}}{2} - \dfrac{1}{2} \cdot \dfrac{d\phi}{dz}$

The detuning is assumed to be constant, such that:

Equation 2.28 $\delta = \dfrac{\beta_1 - \beta_2}{2} - \dfrac{\pi}{\Lambda} = \pi \cdot \Delta n_{eff} \cdot \left(\dfrac{1}{\lambda} - \dfrac{1}{\lambda_D} \right)$

Where $\lambda_D = \Delta n_{eff} \cdot \Lambda$ is the design wavelength for an infinitesimally weak grating. As of the case for Bragg gratings, $\delta = 0$ corresponds to the grating condition predicted by the qualitative picture of grating diffraction.

For a uniform LPG, Γ^{+} and κ are all constants, hence, when applying the appropriate boundary conditions, the transmission of LPG can be evaluated through:

Equation 2.29 $\dfrac{\left| A^{+}(z) \right|^2}{\left| A^{+}(0) \right|^2} = \cos^2 \sqrt{\kappa^2 + \Gamma^{+2}} \cdot z + \dfrac{\Gamma^{+2}}{\kappa^2 + \Gamma^{+2}} \cdot \sin^2 \sqrt{\kappa^2 + \Gamma^{+2}} \cdot z$

Equation 2.30 $\dfrac{\left| B^{+}(z) \right|^2}{\left| A^{+}(0) \right|^2} = \dfrac{\kappa^2}{\kappa^2 + \Gamma^{+2}} \cdot \sin^2 \sqrt{\kappa^2 + \Gamma^{+2}} \cdot z$

Where $\dfrac{\left| A^{+}(z) \right|^2}{\left| A^{+}(0) \right|^2}$ indicates the transmission response of the bound-core mode due to the core-cladding mode coupling regime. $\dfrac{\left| B^{+}(z) \right|^2}{\left| A^{+}(0) \right|^2}$ refers to the ratio of the power coupled into the cladding mode from the core mode.

2.3.1.3 Tilted Fibre Gratings

As a special category of fibre gratings, tilted fibre gratings are capable of coupling the core mode into both radiation modes and cladding modes. This type of gratings generally involves three regimes including tilted angle at < 45º, = 45º and > 45º. Figure 2.4 shows the schematic of mode coupling in tilted fibre gratings in three regimes.
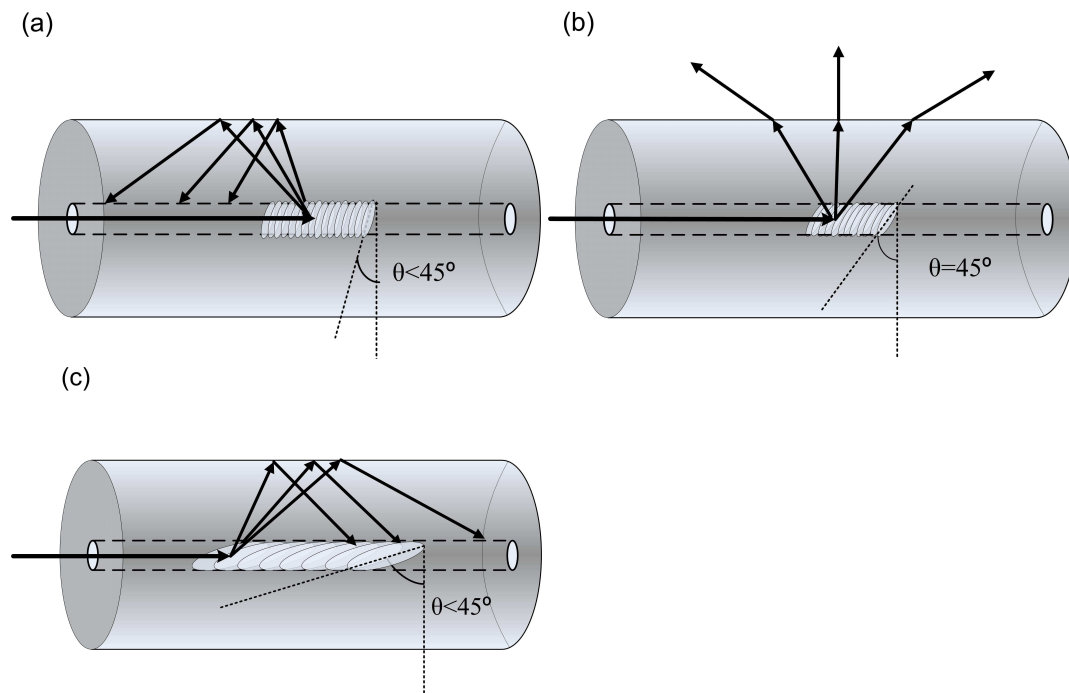
Figure 2.4 Different coupling regimes in tilted fibre gratings for tilted angle (a) < 45º, (b) = 45º and (c) > 45º.

From Figure 2.4 we can see that, when the tilt angle is smaller than 45º, the grating is capable of coupling the forward propagating core mode into backward propagating core and cladding modes. When this angle is larger than 45º, co-propagating coupling occurs. At 45º, different from the other two regimes, the grating will couple the core mode into radiation mode normal to the fibre axis.
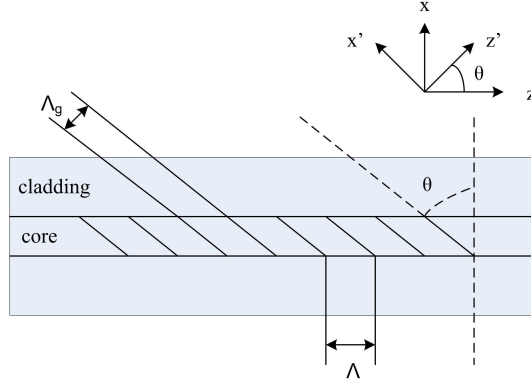
Figure 2.5 Schematic description of tilted fibre grating in an optical fibre

Figure 2.5 shows the schematic diagram of a typical tilted fibre grating structure. Due to the rotation of the grating plane, the index change is now defined as:

$$\text{Equation 2.31} \quad \delta n_{co}(x,z) = \overline{\delta n}_{co}(z') \cdot \left[1 + v \cdot \cos\left[\frac{2\pi}{\Lambda_g} \cdot z' + \phi(z') \right] \right]$$

Where $z' = x \cdot \sin\theta + z \cdot \cos\theta$, $\Lambda = \dfrac{\Lambda_g}{\cos\theta}$ is the grating period along the fibre axis where resonant wavelength for coupling is determined. By taking projections of the grating parameters i.e. $\overline{\delta n}_{co}(z')$, $\phi(z')$ into the fibre axis, the general coupling coefficient turns to be:

$$\text{Equation 2.32} \quad K^t_{\mp\pm}(z) = \Gamma_{\nu\mu}(z) + 2 \cdot \kappa_{\mp\pm}(z) \cdot \cos\left[\frac{2\pi}{\Lambda} \cdot z + \phi \cdot z \cdot \cos\theta \right]$$

Where the forward propagating mode (+) is associated with mode number μ in Equation 2.3 and the backward propagating mode (-) is associated with mode

number υ. The "dc" and "ac" coupling coefficient can then be written in the form of Equation 2.33 and Equation 2.34:

Equation 2.33 $\Gamma(z) = \dfrac{\omega \cdot n_{co}}{2} \cdot \overline{\delta n}_{co}(z \cdot \cos\theta) \cdot \displaystyle\iint_{core} dx \cdot dy \cdot \vec{e}_{\mp}(x,y) \cdot \vec{e}^{\,*}_{\pm}(x,y)$

Equation 2.34

$$\kappa_{\mp\pm}(z,\theta) = \dfrac{v}{2} \cdot \dfrac{\omega \cdot n_{co}}{2} \cdot \overline{\delta n}_{co}(z \cdot \cos\theta) \cdot \iint_{core} dx \cdot dy \cdot e^{\pm i \cdot \frac{2\pi}{\Lambda} \cdot x \cdot \tan\theta} \cdot \vec{e}_{\mp}(x,y) \cdot \vec{e}^{\,*}_{\pm}(x,y)$$

It is found that $\kappa_{\pm} = \kappa_{\mp}^{*}$. Furthermore, the grating tilt can be represented by "effective fringe" in terms of visibility $v_{\mp\pm}(\theta)$ which is given by:

Equation 2.35 $\dfrac{v_{\mp\pm}(\theta)}{v} = \dfrac{\displaystyle\iint_{core} dx \cdot dy \cdot e^{\pm i \cdot \frac{2\pi}{\Lambda} \cdot x \cdot \tan\theta} \cdot \vec{e}_{\mp}(x,y) \cdot \vec{e}^{\,*}_{\pm}(x,y)}{\displaystyle\iint_{core} dx \cdot dy \cdot \vec{e}_{\mp}(x,y) \cdot \vec{e}^{\,*}_{\pm}(x,y)}$

Therefore, Equation 2.34 can be rewritten in a similar form to Equation 2.9 as:

Equation 2.36 $\kappa_{\mp\pm}(z,\theta) = \dfrac{v_{\mp\pm}(\theta)}{2} \cdot \Gamma(z)$

This result states that how effective the grating perturbation is in backward Bragg reflection. It also shows that how grating tilt can reduce the effective fringe visibility according to Equation 2.35. Detailed analysis on tilted Bragg gratings using CMT have been reported recently by various groups. Xu *et al* [81] simulated the spectral

behaviour including polarisation consideration for TFGs with tilted angle <45°. Later, Xu *et al* developed a method using both CMT and Mueller matrix to examine the spectral dependence in terms of polarisation dependent loss (PDL) and degree of polarisation (DOP) after light passes through a TFG with tilted angle ≤45° [82]. While Lu *et al* [83] from the same group investigated the radiation mode coupling from the TFGs using simplified CMT. For grating with a tilted angle >45°, known as excessively tilted fibre gratings (Ex 45°-TFGs), there is still no clear theoretical analysis. Since its large period and strong asymmetry, the polarisation effect has to be taken into consideration with CMT which is believed to play an important role for TFG characteristics. More detailed analysis for TFGs will be considered for future work.

2.3.2 Volume Current Method for Analysing Tilted Fibre Gratings

One of the other recently developed treatments to explain tilted fibre gratings is Volume Current method, also referred as Green Function method [13, 84]. Although CMT offers a rigorous approach to describe the mode coupling between forward propagated core mode and backward propagated radiation mode, it does not show the radiation pattern of the TFGs. By deriving an explicit expression of the Poynting vector of the radiated fields, VCM provides an easy route to predict the radiation properties of the light coupled out of the optical fibre, presenting an insight on how the tilted gratings could be designed to obtain desired radiation response. In an ideal tilted grating, with infinite cladding thickness, the core mode loss produced by the tilted structure hence forms the radiation mode. This loss of the core mode propagating through a small section of TFG in a single mode fibre can be written as:

Equation 2.37 $Loss = -\sigma \cdot \delta l$

Where δl is the grating section and σ is the loss coefficient. The loss coefficient is given by [13]:

Equation 2.38 $\sigma = -\dfrac{k_0^3 \cdot \delta n^2}{4 \cdot n} \cdot \dfrac{1}{1 + \dfrac{u^2}{w^2}} \cdot \dfrac{K_1^2(a \cdot w)}{K_0^2(a \cdot u)} \cdot f$

Where $k_0 = \dfrac{2\pi}{\lambda_0}$ is the wave vector of the incident light in vacuum and δn and n are

the index perturbation of the grating and original index of the fibre core, respectively.

a is the radius of the fibre core. K_0 and K_1 are the zero order and 1st order of

$K - bessel$ function. u and w are the well known fibre waveguide parameters defined

by:

Equation 2.39 $u = \sqrt{(k_0 \cdot n)^2 - (k_0 \cdot n_{eff})^2}$

Equation 2.40 $w = \sqrt{(k_0 \cdot n_{eff})^2 - (k_0 \cdot n_{clad})^2}$

Where n_{eff} is the effective index of the propagating modes and n_{clad} is the refractive

index of the cladding of the fibre. The integral parameter f in Equation 2.38 is given

as below [13]:

Equation 2.41

$$f = \int_0^{2\pi} [1 - \sin^2\theta \cdot \cos^2(\psi - \varphi)] \cdot \left[\frac{K_{new} \cdot J_0(a \cdot u) \cdot J_1(a \cdot K_{new}) - u \cdot J_0(a \cdot K_{new}) \cdot J_1(a \cdot u)}{K_{new}^2 - u^2} \right] \cdot d\varphi$$

In Equation 2.41, ψ is the grating tilt angle and J_0 and J_1 are the zero order and 1st

order of the $J - bessel$ function, K_{new} is given by:

Equation 2.42 $K_{new} = \sqrt{K_t^2 + k_0^2 \cdot n_{clad}^2 \cdot \sin^2\theta + 2 \cdot K_t \cdot k_0 \cdot n_{clad} \cdot \sin\theta \cdot \cos\varphi}$

Where θ is the angel between the radiation beam, and the fibre axis which satisfies the following equation:

Equation 2.43 $K_g - n_{eff} \cdot k_0 + k_0 \cdot n_{clad} \cdot \cos\theta = 0$

K_g and K_t are the wave vector of the grating in longitudinal and transverse direction individually which are defined by:

Equation 2.44 $K_g = \dfrac{2\pi}{\Lambda} \cdot \cos\psi$

Equation 2.45 $K_t = \dfrac{2\pi}{\Lambda} \cdot \sin\psi$

Using the formulas above, it is then possible to evaluate the polarisation properties of the TFGs. The simulated results of the polarisation performance for TFGs are shown in Figure 2.6. In Figure 2.6(a), the core radius is set at 4.5 µm which is close to the practical condition of a standard telecom fibre; the resonance wavelength has been set at 1.55 µm. The grating length is assumed to be 25 mm. It can be seen that for various tilted angles, the grating shows maximum polarisation extinction ratio (PER) or PDL at 45°. One may notice that for small tilted angles (i.e. <20°), the loss for both *s*- and *p*-light becomes very high. This can be explained that at small tilted angles *s*- and *p*-

light degenerate. Both *s*- and *p*-light are actually reflected by the grating which shows very high transmission loss at tilted structure. The high transmission loss for large tilted angle (i.e. >70°) in the simulation may be interpreted by different types of mode coupling regime through the grating which might be forward propagating mode coupling or radiation mode coupling.
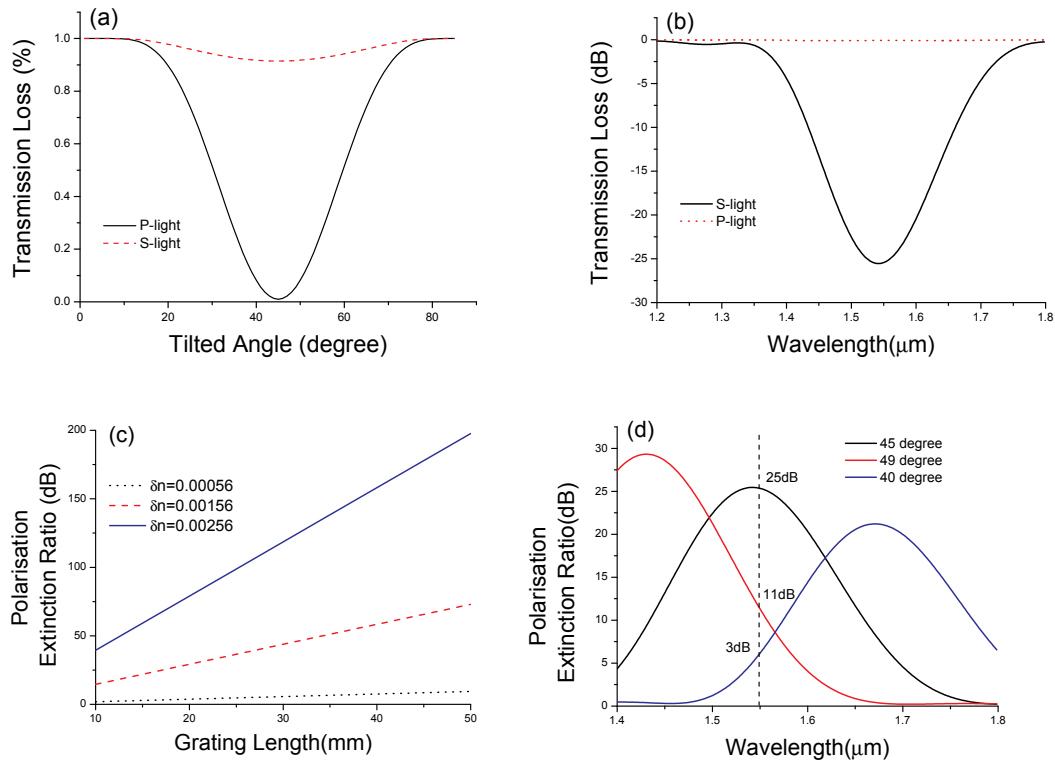
Figure 2.6 (a) Transmission loss against grating tilted angle for *s*- (red dotted line) and *p*-light (black solid line) of TFG; (b) spectral response for *s*-(black solid line) and *p*- (red dotted line) light of a 45°-TFG from 1200 nm to 1800 nm;(c) PER of for 45°-TFG at various lengths with different UV induced refractive index modulations; (d) spectral response of TFG of PER against tilt angles.

Figure 2.6(b) describes the spectral response for a 45°-TFG from 1200 nm to 1800 nm for *s*- and *p*- light. It shows a Gaussian-like shape, ~ 100 nm effect bandwidth of high PER which is centred at 1550 nm. In Figure 2.6(c), as particularly interesting, the relationship between the grating length and core refractive index change with respect to the PER has also been examined for a 45°-TFG. It can be clearly seen that the PER

increases linearly with the grating length. It also shows that for different grating modulation levels i.e $\delta n = 0.00056, 0.00156, 0.00256$, the PER varies significantly indicating that higher refractive index change gives higher PER. Figure 2.6(d) illustrates the spectral change of a 45°-TFG against tilt angle variation in terms of PER. It show that for a designed grating with resonance wavelength at 1550 nm if the tilt angle increase (49°) or decrease (40°) with respect to 45°, the resonance wavelength will have a blue or red shift of about ~100 nm. Furthermore, it is noticed that the PER could drop to 11 dB or 3 dB individually at the desired resonance wavelength. Therefore, care has to be taken when inscribe the 45°-TFGs. One may also notice that, in the simulation, when the tilt angle is at 49°, the grating exhibits higher PER than grating tilted at 45°. This may be because a 49°-TFG is capable of coupling out more *s*-light. However, the loss of *p*-light is minimised when the grating is tilted at 45° therefore making 45°-TFG an ideal candidate for in-fibre polariser. A high PER polariser may be then achieved by inscribing strong 45°-TFG. The simulated results have thus motivated us to examine the polarisation properties of the 45°-TFGs. A more detailed derivation of this method is given by Li *et al* [84].

2.3.3 Phase matching condition of mode coupling for fibre gratings

Another useful approach to understand the mode coupling mechanism in fibre gratings is the phase matching condition. We hereby define the following wave vector relationship for mode coupling in a fibre grating which is commonly regarded as the phase matching condition:

Equation 2.46 $K_{out} = K_{in} + K_{G}$

All K described in this section are vectors. $K_{in} = \dfrac{2\pi}{\lambda} \cdot n_{co}$ is the wave vector of the incident light and $K_{G} = \dfrac{2 \cdot \pi}{\Lambda_{G}}$ is the grating vector. The phase matching condition of a fibre grating can then be described in a vectorial plane in Figure 2.7 and Figure 2.8. For the case of FBG mode coupling, as shown in Figure 2.7(a), the relationship

$K_{out} = K_{in} = \dfrac{2 \cdot \pi}{\lambda} \cdot n_{co}$ applies as an FBG structure will couple the light from a

forward propagating core mode into an identical backward propagating core mode.

For the case of LPG mode coupling, as shown in Figure 2.7(b), the grating can couple

the incident light into forward propagating cladding modes with $K_{out} = \dfrac{2\pi}{\lambda} \cdot n_{clad}$

indicating the cladding modes.

(a)   (b)
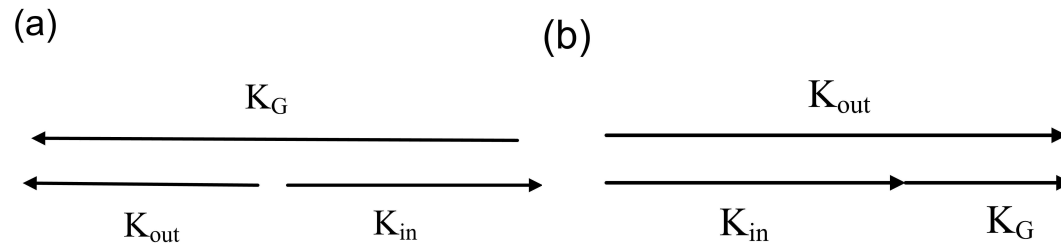
Figure 2.7 Vectorial descriptions of phase matching conditions of (a) FBG and (b) LPG.

For TFGs, as the grating has the ability to couple the forward propagating core mode

into radiation mode, it is hence to have $K_{out} = \dfrac{2\pi}{\lambda} \cdot n_{clad}$ which is similar to LPG. With

the condition $n_{co} \cong n_{clad}$, the following relationship $K_{in} \cong K_{out}$ therefore applies.

Hence, similar to Figure 2.4, the phase matching condition of TFGs can be depicted in

the vector plane which is shown in Figure 2.8, where θ indicates the tilted angle of the

grating with respect to the fibre axis. In Figure 2.8(a), we can simply infer that when

the tilted angle is minimised to zero, the phase matching illustration evolved into the

standard FBG condition from which a forward propagating mode has been coupled

into an identical backward propagating mode via Bragg diffraction. Figure 2.8(b)

shows the special case of 45°-TFG which is capable of coupling out light

perpendicular to the fibre axis or incident beam propagation direction. While Figure

2.8(c) shows the mechanism of an incident beam couples into a forward propagating

mode through an excessively titled grating structure. Although the phase matching

condition gives very good approximation for interpretation of mode coupling

mechanism inside the TFGs, it does not involve the polarisation effect which is

actually one of the key properties of the TFGs.
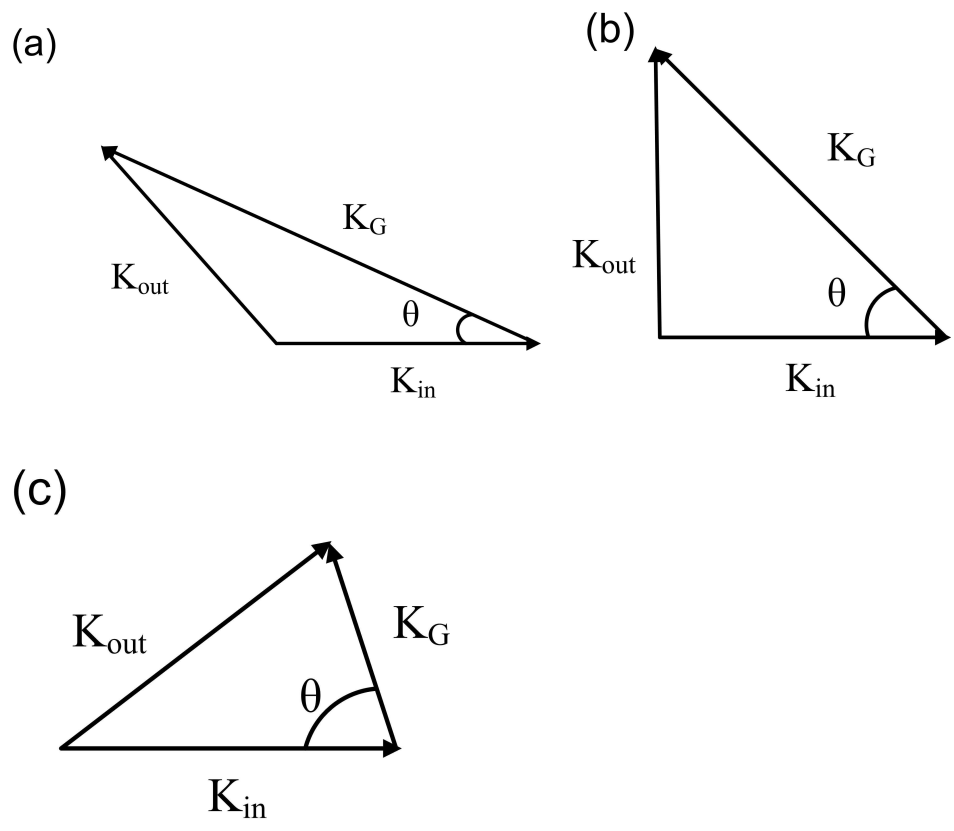
Figure 2.8 Vectorial description of phase matching conditions for TFGs with titled angles at (a) < 45°, (b) = 45°and (c) > 45°.

2.4 Overview of Fibre Grating Fabrication Techniques

Inscription of in-fibre FBG using photosensitivity of optical fibre was discovered by Hill *et al* in 1978 during the experimental investigation of non-linear effect in the optical fibre [1, 85]. In this very first FBG inscription, Germania-doped silica fibre and visible Ar^+ laser (488 or 514.5nm) were used in the experiment. Due to the Fresnel reflection (nominal value ~4%) of the cleaved fibre end, incident light reflected by this could thus interfere with the propagating beam thereby creating a standing wave within the fibre core. The standing wave pattern of refractive index was therefore inscribed in the fibre core because of the intrinsic photosensitivity of the optical fibre. This kind of FBG was lack of wavelength tunability and very much incident light wavelength dependent, although they could be inscribed through self-organised formation of incident laser beam or referred as internal writing technique.

Consequently, more versatile fabrication techniques are required. Various UV inscription methods (i.e. external writing techniques) have been reported since then which are able to provide grating fabrication with flexible Bragg wavelength [86-88]. The widely adopted grating fabrication methods including two-beam holographic [86], point-by-point inscription [89] and mask scanning [87-88] are discussed below.

2.4.1 Two-Beam Holographic

The two-beam holographic fabrication technique for UV written fibre gratings was initially demonstrated by Meltz *et al* in 1989 [86]. This grating inscription system requires amplitude-splitting interferometer and gratings can be fabricated over a wide range of wavelengths - typically from 600 nm to 1700 nm, and independent of incident laser wavelength. The original system used by Meltz *et al* [86] was used to fabricated FBG in the visible region. Figure 2.9 illustrates the schematic of a typical two-beam holographic grating inscription system in our lab. Such a system normally employs a beam splitter with preferable 50:50 splitting ratio. The divided two beams are reflected by two mirrors (M1, M2) with similar reflectivity, and then focused by two similar cylindrical lenses (L1, L2), therefore producing interference fringes in the fibre core when the two beams are recombined. The application of cylindrical lenses is to focus the UV beam thereby allowing high intensity UV irradiation on fibre over which effective and strong gratings could be inscribed. The period of the holographically produced grating is described below:

Equation 2.47 $\Lambda = \dfrac{\lambda_{uv}}{2 \cdot \sin \alpha}$

Where λ_{uv} is the incident UV wavelength, α is the angle between the reflected beam and the beam splitter plane as shown in Figure 2.9. The Bragg wavelength can then be given as:

Equation 2.48 $\lambda_{Bragg} = \dfrac{n_{eff} \cdot \lambda_{uv}}{\sin \alpha}$
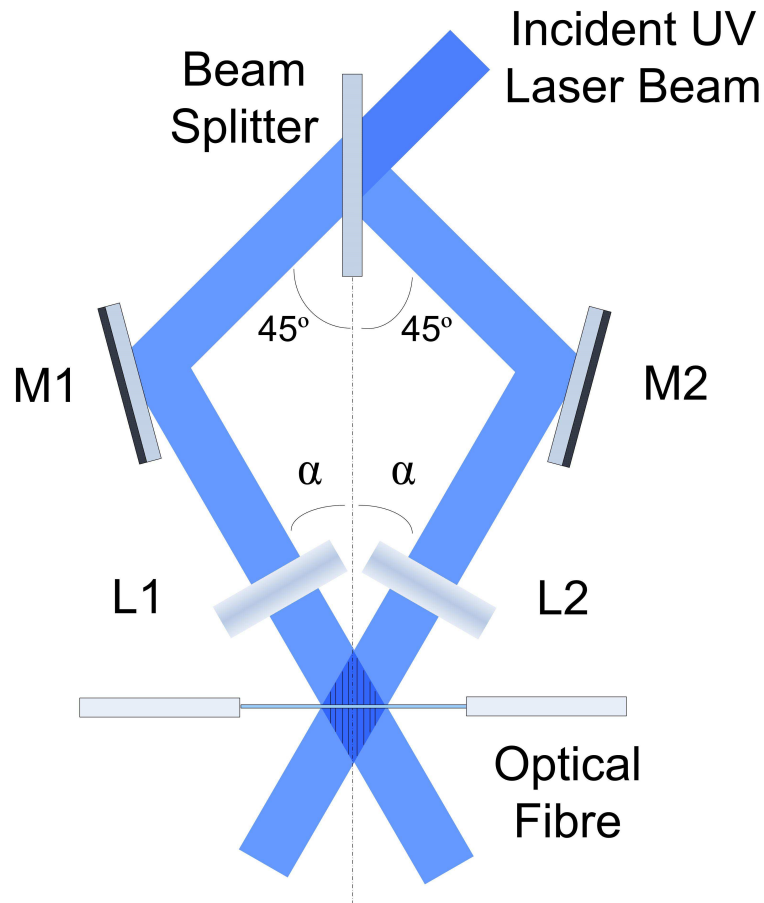
Figure 2.9 Schematic illustration of two-beam holographic inscription of fibre grating

where n_{eff} is effective refractive index for propagation mode in the fibre. λ_{Bragg} is the general description of Bragg wavelength for non-tilted FBG. The most advantage of this technique is the ability to inscribe FBG at arbitrary resonance wavelength by changing the UV wavelength and the angle of the intersecting beams α. By tilting the optical fibre, this method provides possibility for inscribing titled FBGs. It is worthy to note that the system setup shown in Figure 2.9 is only valid for UV light source with a long coherence length, for instance, ~60mm in the case of Ar^+ laser. For UV light produced by low coherence source such as excimer laser, an additional plate is necessary to compensate the optical path difference induced by the beam splitter.

Nevertheless, this system is subject to environmental vibration significantly due to its relatively long exposure time (typically is a few mins). Fringes quality is apt to degrade by even submicron displacement induced through any components in the system. Another limitation of the two-beam holographic method is the grating length

is limited to the UV beam size, which is typically a few mm. Such short FBGs would result in large reflection bandwidth which may not suitable for some applications.

Because the standard two-beam holographic system normally uses more optical components, other interferometer systems based on wavefront splitting using prism interferometer [90-91] and Lloyd interferometer [92] have been developed to overcome this disadvantage while reducing the sensitivity to mechanical stability dependence. Although these two methods provide a more stable inscription by using less components, they are lack of tunability and limited length of inscribed grating significantly restricts their popularity. Note, it is demonstrated that chirped FBG can be fabricated using the two-beam holographic method [93-94]. It is also shown that TFGs can be fabricated with this method [95].

2.4.2 Point-by-point Fabrication

Point-by-point inscription was firstly reported by Malo *et al.* [89]. In their system, a KrF excimer laser and a 15 µm slit were used. A lens was used to project the image of the slit on the fibre core. Because the focused UV beam spot size is normally larger than the period of a standard Bragg grating period (~500 nm for 1550 nm region) resulting in ~700 nm of the width of the photoinduced perturbation area, it is hence generally difficult to inscribe 1st order Bragg grating although in principle the diffraction limit of 244 nm is ~250 nm. A 3rd order micro Bragg grating has been fabricated with a significantly short length of ~360 µm, exhibiting 70% peak reflectivity at 1536 nm in a D-shape fibre [89].
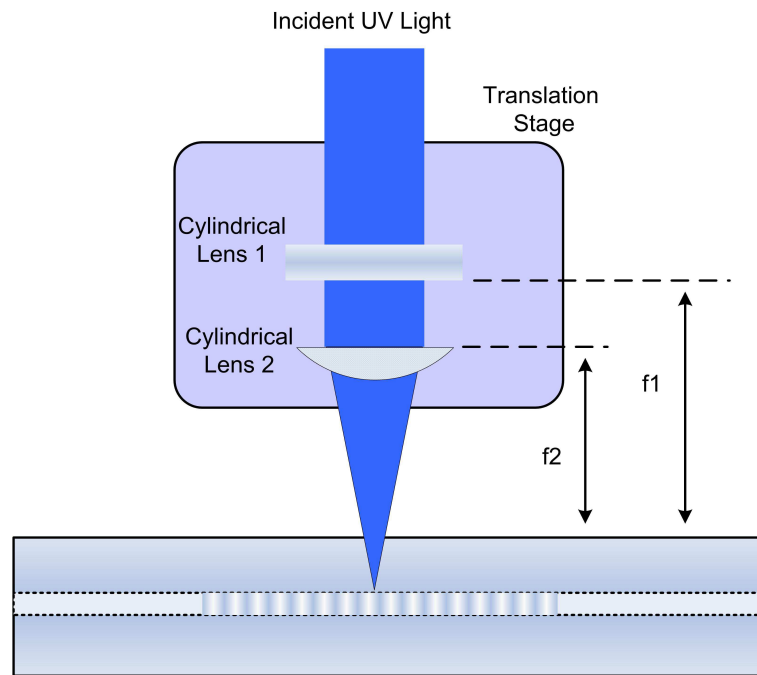
Figure 2.10 Schematic diagram of point-by-point fibre grating inscription.

Figure 2.10 shows the schematic diagram of point-by-point fabrication system in our lab. In our system, rather than using a slit, a second cylindrical lens was adopted in the system to focus the beam along the fibre axis. Various parameters such as grating period, grating length can be controlled through computer programme. This method is widely used for long period fibre grating fabrication from which high flexibility can be obtained for various parameters. The disadvantage of this technique is that it normally requires long fabrication time, environmentally induced grating stitch errors. Positional accuracy of the motion stage may also dominate the quality of the gratings. The point-by-point technique has been reported for the fabrication of rocking filter or polarisation mode converter [96-97] and mode converter [98-99].

2.4.3 Mask Scanning

A major step of fibre grating inscription improvement is the development of phase mask scanning method. This technique is reported firstly by Anderson and Hill [87-88] in 1993 at the same time. Since then, it has been accepted as the most effective way of fabricating fibre gratings. Compared to holographic methods, fewer components are used providing robust and stable solution to grating inscription thus greatly reducing the complexity of the fabrication system.
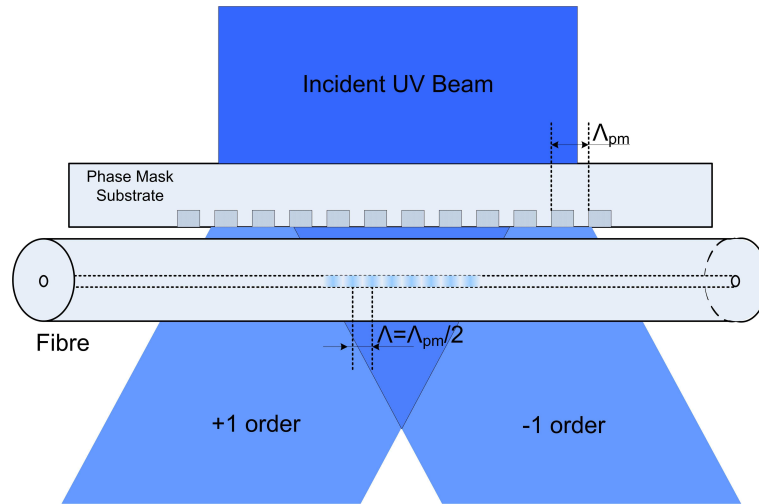
Figure 2.11 Schematic of the phase mask inscription of FBG when the UV beam incident normally to the phase mask.

The phase mask is a UV transparent fused silica plate with one-dimensional surface-relief grating etched in it. Either holography or electron-beam lithography is employed to manufacture the phase mask. It has a period of Λ_{pm} and can diffract the incident UV beam into several orders such as $m = 0, \pm 1, \pm 2...$ With carefully controlled grating depth, aspect ratio i.e. ratio of the linewidth to the depth, the phase of the transmitted UV beam can be modulated thus forming a phase mask rather than an amplitude mask. By minimising the zero order transmitted UV beam, a near field interference fringes could be generated by the ± 1 diffraction orders therefore photoimprinting the Bragg grating into the fibre. To minimise the zero order of the normally incident UV beam on the phase mask, the light pass through the grating ridge (fused silica) and the valley (air) will cancel each other as they are out of phase. The design of phase mask can then follow Equation 2.49 [100]

Equation 2.49 $d \cdot (n_{uv} - 1) = \dfrac{\lambda_{uv}}{2}$

Where d is the grating depth, n_{uv} is the refractive index of the UV beam in fused silica (≈ 1.5108 at 244 nm), λ_{uv} is the wavelength of the UV light. Hence, a grating depth of ~238 nm could be obtained for zero order minimised phase mask for 244 nm

illumination. It is worthy to note that changing the UV wavelength will require a different phase mask unless the zero order transmission is physically blocked. The period of inscribed FBG using a phase mask follows the equation below when considering normally incident situation:

Equation 2.50 $\Lambda = \dfrac{\lambda_{uv}}{2 \cdot \sin\theta} = \dfrac{\Lambda_{pm}}{2}$

Where θ is the diffraction angle of the ± 1 order UV beam.
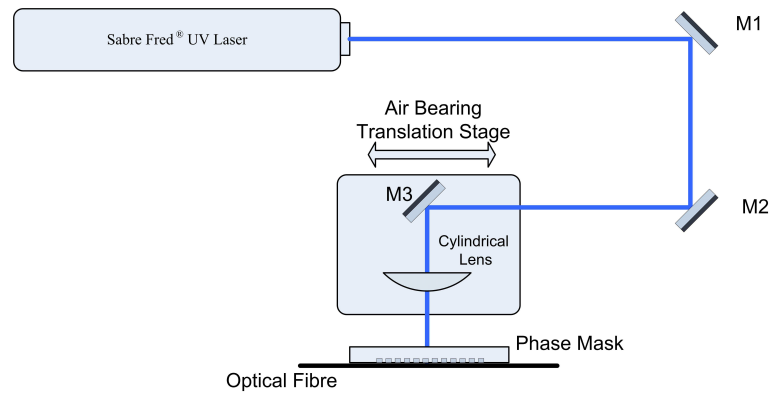
Figure 2.12 Schematic description of typical phase-mask scanning inscription system in our lab.

Figure 2.12 shows a typical experimental arrangement of the phase mask scanning system in our lab. A frequency doubled Ar^+ laser (Sabre Fred®) is used as the UV light source. The UV beam is focused on the fibre core via a cylindrical lens. Then it propagates through the phase mask to incident on the fibre. With the computer controlled movement of high-precision air-bearing stage along the fibre axis, Bragg grating structure can be impinged in the fibre core by scanning the laser beam.

When employing the phase mask, the simplicity of using less components and near-field interference enables stable, repeatable and uniform inscription of Bragg gratings. Low temporal coherence would not induce drawback to the system. Moreover, phase mask scanning technique can offer solutions to high quality and complex grating structures such as chirped gratings [101], apodised gratings [102-103], phase shift

gratings [104-105], Moiré gratings [106] and superstructured grating [107].

Nevertheless, the phase mask scanning method is subject to the condition of spatial coherence. If the separation between the fibre and the mask is too close, damage could be caused to the fine corrugation of the phase mask. On the other hand, if the separation is not close enough, poor quality gratings will be produced when UV source with low spatial coherence is used in the system. Another disadvantage of the phase mask scanning method is its limitation to the alternation of inscribed Bragg wavelength due to the fixed period of the phase mask. Hence, additional phase mask might be required for various Bragg wavelengths. Furthermore, several methods have been proposed to overcome this problem. Prohaska showed that by locating a magnifying or converging lens in front of the phase mask could generate longer or shorter wavelength than the designated wavelength fixed by phase mask period [108], Zhang *et al* [109] demonstrated that Bragg wavelength tuning can be achieved using a pre-strained fibre during UV inscription. The length of the phase mask is another issue using this method as more expensive long mask is required for gratings of long length. The phase mask fabricated using the electron beam lithography, stitching errors on the mask may degrade the quality of the FBG. It is worthy to note that TFGs can be inscribed in an optical fibre by either tilting the phase mask with respect to the fibre axis or using a phase mask with tilted pattern. The 45°-TFGs reported in this thesis are all fabricated using phase masks with tilted pattern and ex 45°-TFGs are by tilting the normal amplitude mask.

Another type of mask is the amplitude mask which can be designed for fabricating LPGs. Such mask normally has a period of hundred microns where no diffraction occurs for the UV incident beam. The ridge and valley design issue does not exist for the amplitude mask. Therefore, the cost of amplitude masks can be much lower. Detailed information regarding such mask can be found in reference [100]. The ex 45°-TFGs studied in this thesis are fabricated by tilting the normal amplitude mask.

2.5 Applications of Fibre Gratings

Fibre gratings are popular components in various lightwave applications. Since the discovery of fibre gratings, they have found wide applications in optical communication, signal processing, microwave generation, optical sensing, fibre

amplifiers and fibre lasers etc. This section will briefly review two of the most important applications of fibre gratings.

2.5.1 Fibre Grating Sensors

Due to its inherent compactness and immune to electromagnetic interference, fibre gratings are ideal candidates in the domain of sensing. Combining with the telecom grade compatible interrogation system, fibre gratings could offer a low cost solution for optical sensing with high precision. The capability of multiplexing is the other advantage of fibre grating based sensor network. Strain, pressure and temperature sensing using both FBG and LPG was reported by Kersey *et al* [110]. With the help of cladding modes coupling, LPGs are able to measure the external refractive index [111]. Normally, a single FBG could only deal with sole parameter sensing and more than one FBG is needed for multiple parameter sensing, but for an LPG, utilising the difference of response of different rejection bands of the LPG, one can implement an multi parameter sensing head [112]. Shu *et al* [113] also demonstrated a method for dual parameter sensing using a single sampled grating. However, in dual parameter sensing, cross sensitivity might be an issue which needs a compensation scheme to eliminate. Recently proposed excessively tilted fibre gratings provide a neat solution for overcoming temperature and refractive index cross-sensitivity [114].

The development of interdisciplinary science offers grating sensors a great platform to play. Various refractive index sensors using grating based technology have been demonstrated for biomedical and life science research purposes. Different configurations of LPG were applied in DNA detection [115-116]. Respiratory sensing using fibre gratings based monitoring devices have also been presented [117-119].

For industry and engineering application, grating based sensors are gradually gaining market in these fields. They give monitoring and detection solutions in oil, gas and mining sectors [120-124]. Another good application of fibre gratings based structural health monitoring sensornets are reported for bridges [125-126], dams [127-128] and underground tunnels [129]. There are also reports that various fibre grating sensor configurations have been developed as inclinometers [130-136].

2.5.2 Fibre Grating Lasers

The emergence of fibre gratings offers laser technology great versatility to the conventional laser research. They appear to be very powerful tool to enhance the laser characteristics. Brinkmeyer *et al* proposed the very first fibre grating stabilised semiconductor laser which gives out narrow linewidth output [137]. All fibre lasers are therefore more attractive for both scientific and practical applications. The ability to inscribe Bragg gratings into the rare earth doped fibres results in a variety of successful demonstrations of fibre lasers. Simple laser configuration was presented for giving out single frequency output [138-139]. By using a phase shifted fibre Bragg grating, distributed feedback Erbium doped fibre laser was presented [140-141]. Single polarisation fibre laser was achieved by inscribing a standard FBG into the polarisation maintaining fibre [142]. In mode locked pulsed fibre lasers, fibre gratings represent a novel method to control the gain bandwidth and cavity dispersion of the laser [143-145].

Inscription of fibre gratings on other active media was also reported including Neodymium [142, 146], Ytterbium [147], Praseodymium [148], Erbium-Ytterbium co-doped [149-151], and Thulium [152], which are all potential gain media for fibre lasers across a broad operation range.

2.6 Chapter Conclusions

In this chapter, the fundamental properties of photosensitivity and methods of enhancement of fibre photosensitivity have been reviewed. Coupled mode theory for explaining different types of gratings were discussed, including FBG, LPG and TFG. Recently developed Green Function method for modelling TFG was also briefly reviewed. Major techniques, including two-beam holographic, point-by-point and phase mask scanning, for UV inscribing fibre gratings were introduced in detail. Finally, a short description of fibre grating applications in optical sensing and laser system was given.

Chapter 3

Fabrication and Characterisation of UV Inscribed 45º- and Ex 45º-Tilted Fibre Gratings

3.1 Introduction

This chapter discusses the UV inscription and characterisation of 45º- and ex 45º - TFGs. For the fabrication of 45º-TFGs, we only focus on the method using phase mask scanning, and a large number of 45º-TFGs have been UV-inscribed not just on standard telecom and photosensitive B/Ge doped fibres but also on two types of polarisation maintaining (PM) fibres with spectral response in both 1.06 μm and 1.55 μm regions. Concatenation method using phase mask with limited size to UV-inscribe 45º-TFGs with high polarisation extinction ratio (PER) has also been investigated. Systematic characterisation has been performed on the 45º-TFGs regarding their spectral and polarisation dependent loss (PDL) properties. Various techniques have been implemented to fully characterise the grating properties. Moreover, thermal and refractive index responses of 45º-TFGs have also been investigated.

In the second part of this chapter, the fabrication and characterisation of ex 45º-TFGs, i.e. the fibre gratings with tilted structure at an angle larger than 45° have been discussed. For fabrication, an amplitude mask with scanning UV beam method was applied for inscribing such ex 45º-TFGs. Only standard telecom fibre has been investigated for this type of TFGs. Similarly, the refractive index and thermal responses have been characterised in terms of coupled cladding modes with two different orders.

3.2 Fabrication and Characterisation of 45º-TFGs

3.2.1 Fabrication methods for 45º-TFGs

As shown in Figure 3.1, a 45º-TFG can be inscribed either by tilting the phase mask with respect to the optical fibre (Figure 3.1(a)), or by using a phase mask with tilted pitches (Figure 3.1(b)). One can also inscribe such gratings by tilting the fibre about its axis orthogonal to the plane defined by the two interfering UV beams in a two-beam holographic fabrication system (Figure 3.1(c)).
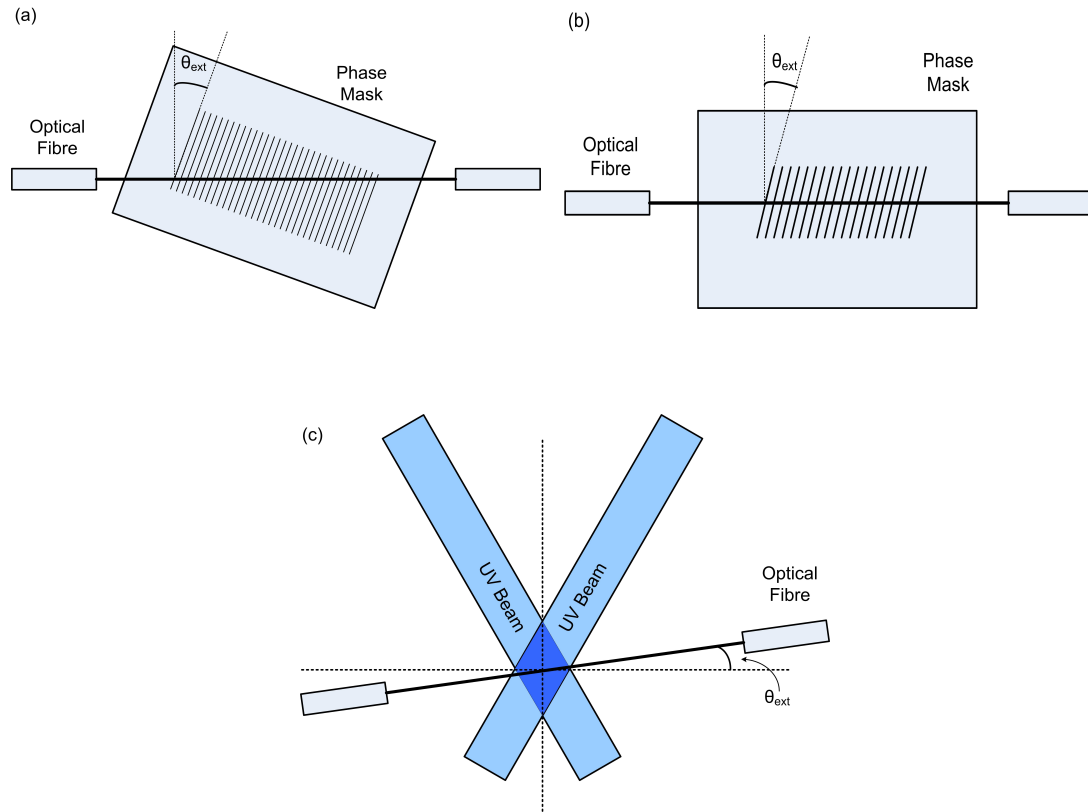
Figure 3.1 (a) and (b) phase mask, (c) two-beam holographic methods for 45°-TFG fabrication.

As discussed in Chapter 2, phase mask scanning technique can inscribe fibre gratings with high quality. All 45°-TFGs reported in this thesis were fabricated with the phase mask method. Detailed information regarding the phase mask parameters and inscription conditions will be described in the following sections.

3.2.2 Relationship between the internal and external tilted angles and period of 45º-TFG

Owing to the geometry of the optical fibre, when a fibre axis is tilted by θ_{ext} with respect to the UV interference fringes, it can generate grating planes with an angle θ_{int} within the fibre core [153].
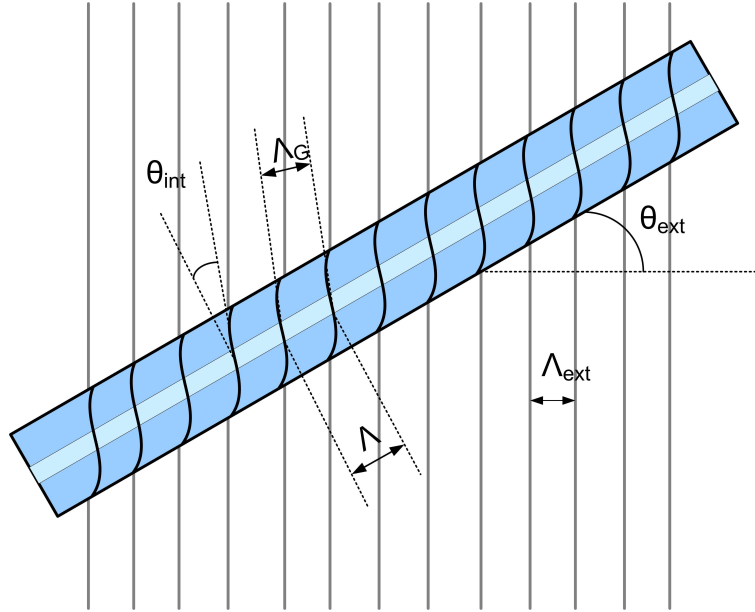
Figure 3.2 Illustration of fringes distortion and a 45°-TFG structure with external θ_{ext}, internal θ_{int} angles and period Λ_G .

Figure 3.2 depicts the effect regarding the fringe difference between external and internal angles when using a phase mask technique. The relationship between θ_{ext} and θ_{int} is given by [11] :

$$\text{Equation 3.1} \quad \theta_{int} = \frac{\pi}{2} - \tan^{-1}\left[\frac{1}{n_{uv} \cdot \tan\theta_{ext}}\right]$$

Where $n_{uv} = 1.51$ is the refractive index of fibre at UV wavelength. The relationship between the internal and external angles is plotted in Figure 3.3.
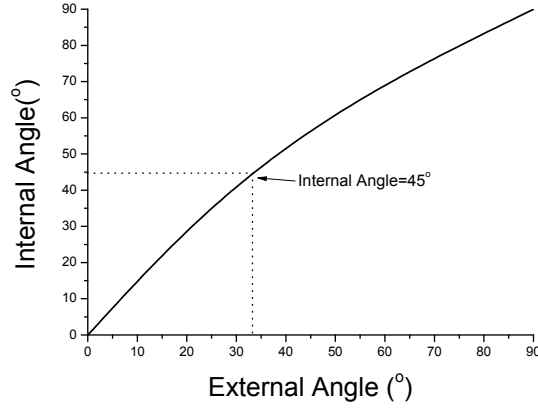
Figure 3.3 Plot of internal angle against external angle for TFG fabrication. Note, the cross point for the two dotted lines indicates the point where the internal angle is 45°.

Figure 3.3 shows that how the internal angle changes when different external angle applies. We can calculate that when the external angle is $\approx 33.7^o$, it can produce grating planes tilted at $\approx 45°$ internally and it is this 45°-TFG structure exhibiting interesting polarisation and spectral properties which will be investigated in the following sections. From Figure 3.2, we can infer that

Equation 3.2 $\Lambda = \dfrac{\Lambda_G}{\cos\theta_{\text{int}}} = \dfrac{\Lambda_{ext}}{\cos\theta_{ext}}$

Hence, the inscribed tilted grating period Λ_G is given by

Equation 3.3 $\Lambda_G = \dfrac{\Lambda_{ext} \cdot \cos\theta_{\text{int}}}{\cos\theta_{ext}}$

Where Λ_{ext} can be found from the well-known relationship $\Lambda_{ext} = \dfrac{\Lambda_{PM}}{2}$, and Λ_{PM} is

the period of the phase mask used in the inscription system. According to the phase matching condition discussed in Chapter 2, we can then deduce that the corresponding periods of phase masks are ~1785 nm and ~1216 nm for 1.55 μm and 1.06 μm regions, respectively, and then the according grating periods along the fibre axis are ~1071 nm and ~731 nm, respectively. During the experiments, the angle alignment is achieved by tuning a commercial grade goniometer where the phase mask is mounted. The angle between the diffraction pattern from the phase mask and a pre-aligned horizontal line has to be around 33.7°. The amount of tuning is normally quite large if a normal mask is going to be tilted for 45°-TFG inscription while small for a tilted mask. The accuracy of the alignment relies on the precision of the goniometer with a nominal accuracy of ±1 °.

3.2.3 Analysis of fundamental limit on fabrication of 45º-TFGs

As discussed in Chapter 2, a fibre grating inscribed in the fibre core relies on the size of the UV interference area after the phase mask. In our experimental system, owing to the usage of a cylindrical lens, the incident beam on the phase mask is a rectangular shape. When the beam diffracts from a non-tilted phase mask, the two diffracted main beams (+1 and -1 orders, assuming zero order transmission is eliminated) will only depart from each other in the x-y plane, as shown in Figure 3.4(a). However, in the case of a tilted phase mask, the diffracted +1 and –1 orders will separate in the y-z plane as well. This separation in y-z plane therefore reduces the effective UV interference area on the fibre. The separation effect is much more severe in the y-z plane than that in the x-y plane. From estimation, we can know d_2 (the maximum effective penetration depth of the UV interference region in the case of a tilted phase mask) in Figure 3.4(b) is much smaller than d_1 (the depth of the effective UV interference region) in Figure 3.4(a) for a normal phase mask. The interference region of the UV beam after the tilted phase mask is drawn in Figure 3.4(c) showing as a trapezium, where φ denotes the phase mask tilt angle, L is proportional to the phase mask period. Therefore, d_2 could be calculated as $d_2 = \dfrac{h}{2 \cdot \tan \varphi}$ with a given beam height h. In Figure 3.4(d), it illustrates the side view of the trapezium interference area covering the optical fibre. In order to achieve efficient grating inscription, d_2 is

defined by the geometry structure of the optical fibre from which the fibre core would be completely covered by the UV interference region. For a single mode fibre with cladding radius (r_{cl}) of ~62.5 µm and core radius (r_{co}) of ~ 4 µm, d_2 has to exceed ~69.7 µm for the complete core coverage by UV interference region. Hence, for efficient 45°-TFG inscription, a minimum beam height of ~93 µm is required.
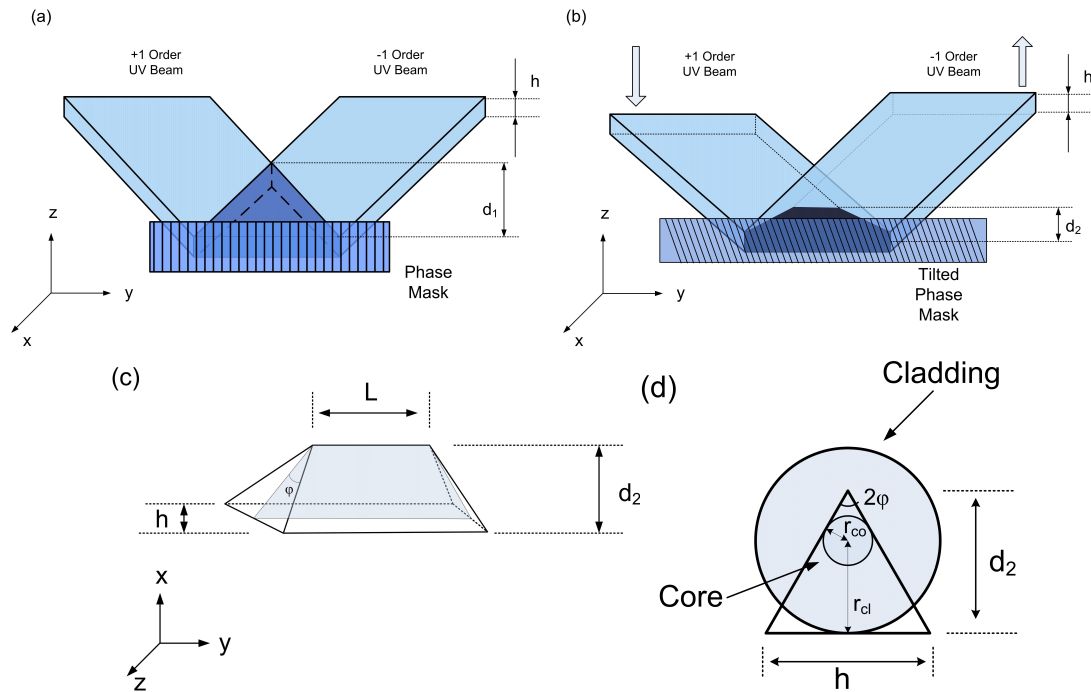
Figure 3.4 Schematic description of UV beam diffraction after the phase mask: (a) from a non-tilted phase mask; (b) from a tilted phase mask; (c) Trapezium of the interference area from a tilted phase mask; (d) side view of the UV interference trapezium showing complete coverage of the fibre core.

In order to achieve effective 45°-TFG inscription, increasing d_2 is necessary. It is therefore natural to defocus the UV beam to obtain the grating inscription optimisation condition. The defocused distance for the 45°-TFG inscription may be derived from the standard Gaussian beam analytical expression [154]:

Equation 3.4 $\Delta f = z_R \cdot \sqrt{\left(\dfrac{h'}{w_0}\right) - 1}$

Where Δf is the defocused distance, h' is half of the beam height, w_0 denotes the Gaussian beam waist, $z_R = \dfrac{\pi \cdot w_0^2}{\lambda_{UV}}$ is the Rayleigh range of the UV beam and λ_{UV} indicates the wavelength of the UV light. Assuming the UV light (wavelength 244 nm) is perfectly focused at the standard single mode fibre core with a core radius of 4 µm, the UV beam waist is thus 4 µm in the case of ideal focusing. The optimised defocus distance can then be calculated to be ~2.27 mm using Equation 3.4. However, it is worthy to notice that defocus of UV beam may result in weakening the power of the interference region as the UV beam intensity will be reduced significantly due to diffraction of a focused Gaussian laser beam. Moreover, for specialty fibres with larger cores, defocus will be a necessity for grating inscription which would ensure the fringes to cover the whole area of the fibre core. Thus, there is a fundamental limit for inscription of 45º-TFGs using the phase mask scanning method. In the work reported in this thesis, I have applied a defocus of ~1.5 mm throughout the fabrication for all 45º-TFGs at 1.55 µm region, so as to balance between the size of the UV interference region and UV power. Figure 3.5 illustrates the schematic diagram of the defocused inscription of the 45º-TFGs.
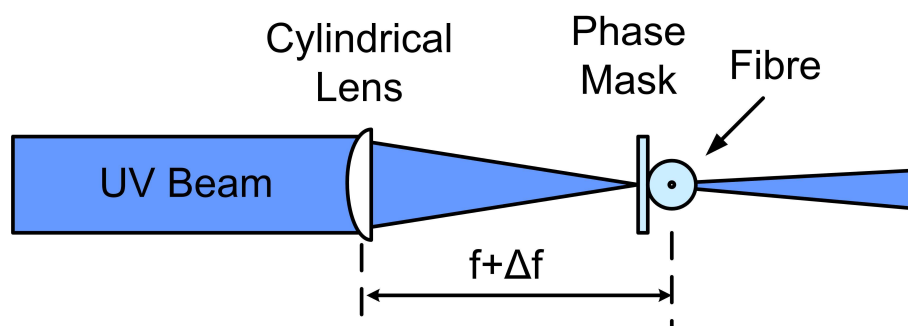
Figure 3.5 Schematic diagram of defocused fabrication of the 45º-TFGs.

3.3 Fabrication and Characterisation of 45º-TFGs at 1.55μm Region

3.3.1 Fabrication of 45º-TFGs by rotating normal phase mask and concatenation

45º-TFGs throughout this thesis were all UV-inscribed in optical fibres using a 244 nm UV light from a frequency doubled Ar^+ laser (Coherent Sabre Fred®) and the scanning phase mask technique. All the optical fibres were H_2-loaded under 150 bar at 80 ºC for 48 hours prior to the UV inscription to enhance fibre photosensitivity. The general fabrication technique is discussed in Chapter 2. Two phase masks were used for 45°-TFG fabrication, one is a normal mask and the other has designed tilted pitches. When the normal phase mask was used, it was tilted at ~33.7º externally to produce 45º tilted fringes within the fibre core. However, this normal phase mask (from QPS Photonics) has only 3.5 mm effective length when rotated at ~33.7º (as shown in Figure 3.1(a)) thus the concatenation method has to be used to achieve long length gratings. The other tilted phase mask (from IBSEN photonics) is designed to have a tilt pattern of ~33.7º with respect to the fibre axis and the total length is ~23.5 mm, which allows strong 45°-TFG fabrication just over one continuous UV-scan.

However, the concatenation technique employed for grating inscription with longer length for strong 45º-TFG function required manual control of the concatenation, which induced various defects, such as stitch errors and bleach effect (i.e. overlapping of the margin areas from the adjacent concatenated grating sections), to the grating structure, resulting in unwanted effects. I have fabricated several 45º-TFGs in H_2-loaded B/Ge co-doped fibre by concatenation technique with different lengths of ~35 mm and ~50 mm. The configuration described in Figure 3.1(a) was applied from which the QPS phase mask was used for inscription. A microscope system (Zeis Axioskop 2 mot plus) was used to inspect the grating structure after the UV inscription. Figure 3.6 shows a typical microscopic image of the UV inscribed 45º-TFG in the fibre core under a 100× oil immersion microscopic lens showing the grating period of ~1081 nm and fringes tilted at 45°.
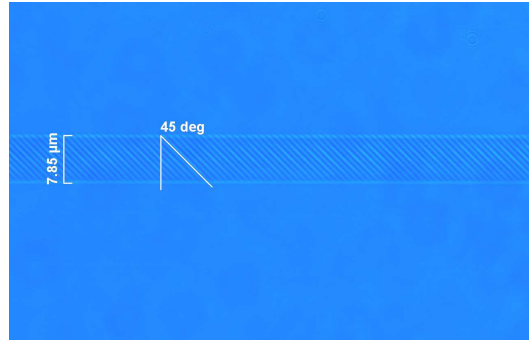
Figure 3.6 Microscope image of a typical 45º-TFG examined by a 100× oil immersion microscopic lens.

In the following sections, detailed information regarding the 45º-TFGs fabricated using concatenation and direct writing will be presented and discussed. Their polarisation dependency and spectral properties will also be described and discussed.

3.3.2 Polarisation dependent loss and spectral measurement of 45º-TFGs

In some passive optical components, the optical loss can be different as the polarisation state of the propagating beam varies. The difference between the maximum and minimum loss with respect to all possible polarisation states is called polarisation dependent loss (PDL). PDL plays important role in the modern optical communication system owing to its effect on system performance [155]. Normally, a few dBs will be the maximum capacity of PDL tolerance. On the other hand, optical devices exhibiting strong PDL may have potential application in polarisation state discrimination. In this section, a systematic evaluation of the 45º-TFGs in terms of their PDL properties will be discussed. In addition, their spectral characteristics have also been investigated.

3.3.2.1 PDL characterisation of 45º-TFGs using BBS and tuneable Laser

The PDLs of the two fabricated 45º-TFGs of lengths of ~35 mm (TFG1) and ~50 mm (TFG2), respectively, have been investigated by using either a broadband source (BBS) or a tuneable laser at single wavelength with an optical spectrum analyser (OSA).

Figure 3.7(a) shows the schematic of the set-up for characterising the PDL using a

BBS source, a commercial fibre polariser, a fibre polarisation controller (PC) and an OSA. Both the polariser and the PC work at 1550 nm region. By changing the PC, we obtain the maximum and minimum transmission spectra of the grating and by subtracting the former to the latter (as they are in dB), we obtain the normalised PDLs for the two 45°-TFGs, as shown in Figure 3.7(b) and Figure 3.7(c), respectively.
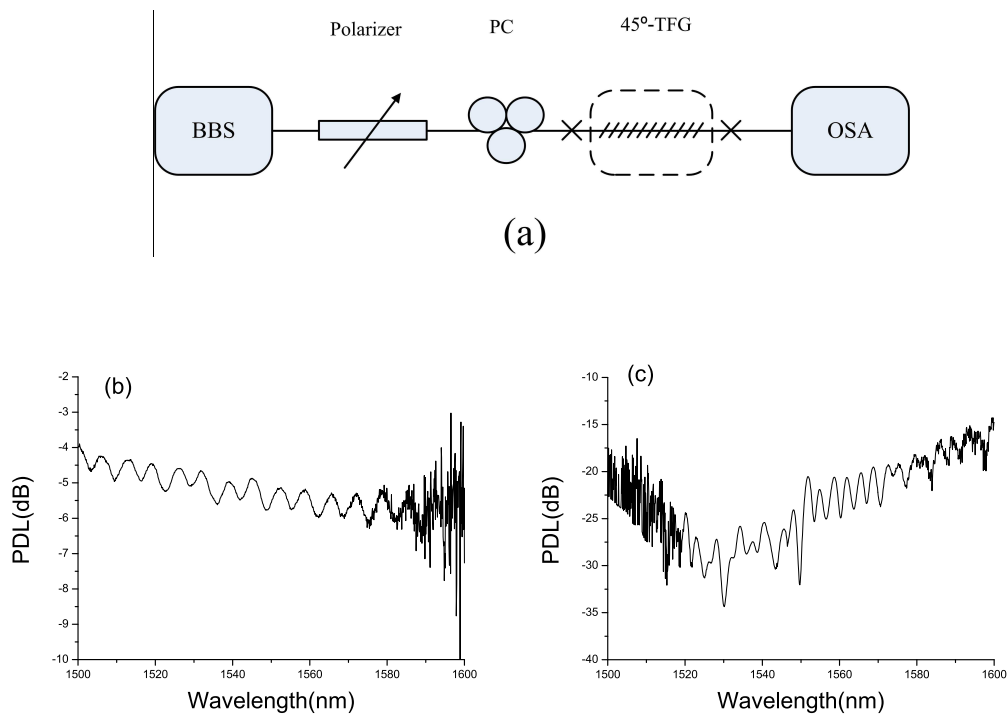
Figure 3.7 (a) Schematic diagram of PDL measurement system employing a BBS. Measured normalised PDLs for (b) TFG1 and (c) TFG2.
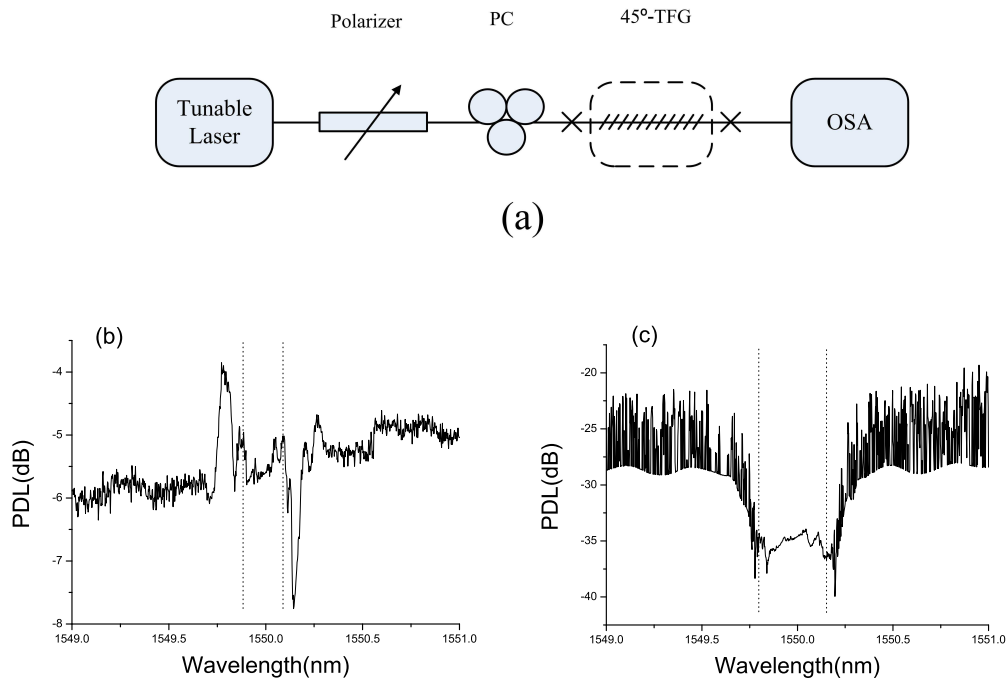
Figure 3.8 (a) Schematic diagram of PDL measurement system using a tunable laser. Measured and normalised PDLs at 1550 nm for (b) TFG1 and (c) TFG2. Note: as the laser was set at 1550 nm, only the section between the two dotted lines in the plot is the correspondent PDL.

Although the PDL of a 45°-TFG has a rather large bandwidth (~100 nm), the PDL value is still wavelength dependent. Using the BBS measurement system, the measured maximum PDLs for TFG1 and TFG2 were ~5.8 dB and ~35 dB, when the polarisation was optimised for 1550 nm. Here it is clearly to see that the PDL is strongly grating length dependent, as the 50 mm TFG2 achieved almost five times higher PDL than that of 35 mm TFG1. It can be also noticed from Figure 3.7 that the oscillation appeared on the PDL spectra when using the BBS as the light source. This could be explained as following. The 45°-TFG will couple out the s-light as radiation from the fibre core, however, a typical optical fibre does not have an infinite cladding, thus the radiated modes could be reflected back via the cladding/air boundary hence forming the cladding modes oscillation.

The PDLs of the two 45°-TFGs were also measured at single wavelength using the tuneable laser as shown in Figure 3.8(a). In this measurement, the tuneable laser was set at 1550 nm and then the PC was changed to get the maximum and minimum PDLs.

Figure 3.8(b) and Figure 3.8(c) show the normalized PDLs for the two gratings at 1550 nm. The PDL values measured from using tuneable laser are 5.5 dB (TFG1), 35 dB (TFG2), which are in a good agreement with the maximum values measured using the system employing BBS.

3.3.2.2 Full PDL response investigated by a linearly polarised light

The full PDL response of the two 45°-TFGs were then further characterised by using linearly polarised light rotating from 0^0~360^0. Figure 3.9(a) shows the schematic of the full PDL response characterisation system using linearly polarised light, which is generated from the tuneable laser through a polarisation beam splitter (PBS). The full PDL characterisation principle is described as following. Because the fibre PBS uses two pieces of polarisation maintaining fibre as the output ports, either port could serve as a linear polarised light source while unpolarised light entered the input port of the PBS. One output port of the PBS is cleaved and then fitted into a high precision fibre rotator as the probe port. This fibre rotator is mounted on a high precision three dimensional translation stage while the 45^0-TFG is fixed on another nearby stage. One end of the 45^0-TFG is also cleaved almost at the start point of the grating which is used for coupling in the linearly polarised light while the other end is monitored through a high speed power meter. The other output port of the PBS is monitored using the same power meter but with a different channel. This functions as a reference signal capable of monitoring power variation of the light source. By adjusting the PC, we could maximise the light coupled into the probe port of the PBS. Then, we can align either translation stage to ensure the maximum coupling from the PBS to the 45^0-TFG. When the coupling optimisation is completed, the fibre is rotated using the fibre rotator in a 10° step for 360° with PDL recorded for each step.
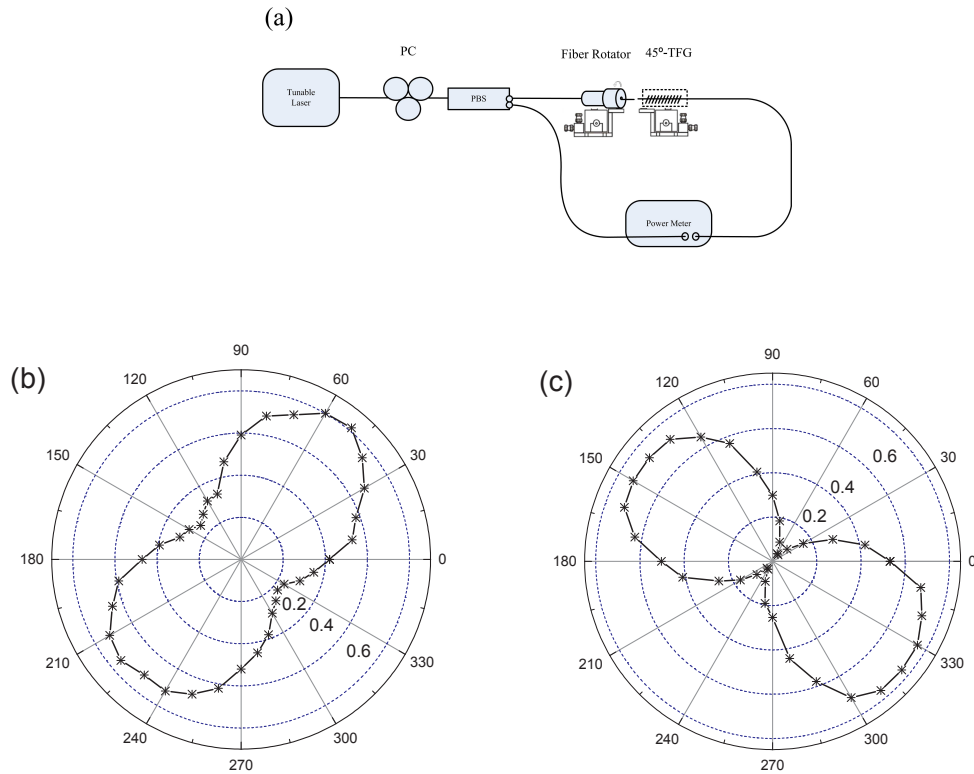
Figure 3.9 (a) Full PDL response characterisation system setup using linearly polarised light. Measured full PDL responses for (b) TFG1 and (c) TFG2.

Figure 3.9(b) and Figure 3.9(c) show that the PDLs go through two cycles as expected due to the existence of two maximum and two minimum PDL positions. From Figure 3.9(b), one can see that the transmission reaches the maximum at the angles near 50^0 and 230^0 while the minimum at the orthogonal positions, i.e. 140^0 and 320^0. This $\pm 90°$ difference from the maximum to the minimum value on figure-8 plot indicates the linear polariser functionality of the 45°-TFG. The two minimum values indicate how much s-light is coupled out by the 45^0-TFG and then the polarisation extinction ratio of TFG1 shown in Figure 3.9 (b) can be calculated as ~ 5 dB, which corresponds well to the measured PDL results by BBS and tuneable laser described in the section above. Figure 3.9(c) shows the full PDL measurement for TFG2 which has a longer grating length (~50 mm), we can see the shape is a closed figure-8 (the shorter grating, TFG1, gives a non-closed figure-8 shape), indicating much higher PDL as the minimum transmission becomes nearly zero at these two positions. The calculated PDL is ~ 12 dB which is smaller then the measured PDL value using other method.

This could attribute to the measurement error induced by the fibre rotator when approaching the minimum value. Later experiment commenced by other colleagues in the group have proved that with very fine tuning of the fibre rotator, this technique could provide similar results of PDLs as the methods described in the above section.

3.3.3 45º-TFG fabrication and characterisation using tilted phase mask

In the later stage of my project, a phase mask with tilted pattern was purchased from IBSEN Photonics which allowed direct 45º-TFG fabrication without multi-section concatenation. In principle, this mask should enable to UV-inscribe 45°-TFGs with high quality and consistent profiles. This phase mask is designed to have a tilt pattern of ~33.7º with respect to the fibre axis and grating period of ~1800 nm, which will generate 45° tilted fringes in the fibre core with resonance wavelength at ~1.55 µm. The mask pattern is 25 mm long; this gives ~23.5 mm effective grating length. We have fabricated four 45º-TFGs under similar inscription conditions (i.e. UV power and exposure time) in commercial B/Ge photosensitive fibre (Fibercore® PS1250/1500). A commercial PDL characterisation system (LUNA system), incorporating a commercial tuneable laser, was employed to examine both the PDL and transmission spectra of the gratings.
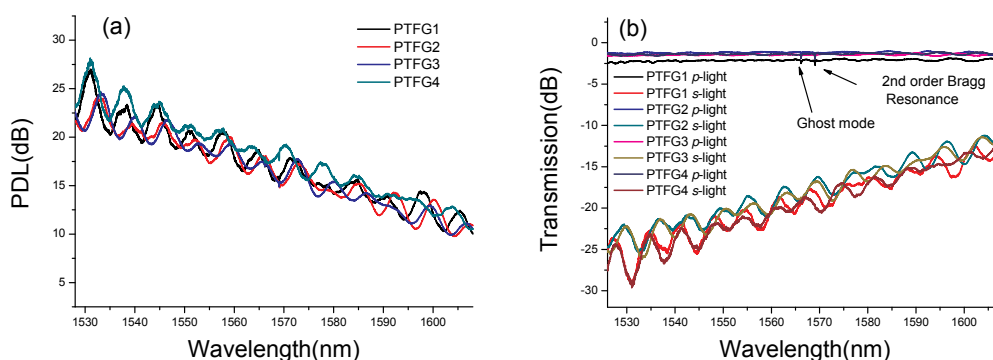
Figure 3.10 (a) PDL and (b) transmission spectra of four 45º-TFGs inscribed under similar condition in PS1250/1500 fibre using the tilted phase mask.

From Figure 3.10 we can infer that, when using a phase mask with longer length, high quality and reproducible 45º-TFGs can be achieved. Referring to section 2.3.2, one

may notice that the measured PDL appears to be linear rather than Gaussian-like shape. The experimental results indicate a blue shift of the central response wavelength of the 45°-TFG. This could mainly attribute to the potential deviation of the effective modal index between theory and the actual fibre at 1.55 µm. It can be seen that all four gratings have ~20 dB PDL at the designated wavelength at 1.55 µm. This corresponds to a UV induced refractive index change of $\delta n \approx 0.001$ when calculating with the volume current method. Furthermore, because the length of phase mask is long enough for strong grating inscription, single scan with a speed faster than that used for concatenation technique was adopted. Therefore, the efficiency of fabricating such gratings could be greatly improved. This further reduces any environmental instability during the inscription. The spectral properties of the 45°-TFGs were examined using the same (LUNA System) commercial characterisation system which also gives the insertion loss of the devices. It can be seen from Figure 3.10(b) that for all four 45°-TFGs, there exist maximum loss and minimum loss (the loss here is given in terms of transmission). The difference between the maximum loss and minimum loss is actually the PDL of the device. These measured results show very good agreement with our theory prediction stating that when light propagates through the 45°-TFG, *s*-light is radiated out while *p*-light confined in the fibre core with a minimum transmission loss. For PTFG2, PTFG3 and PTFG4, the insertion losses for *p*-light have a similar value of ~1.3 dB. It should be noticed that PTFG1 shows slightly higher insertion loss (i.e ~2.5 dB), this may be due to bad splicing induced extra loss to the measurement system. This can be proved by the data in the annealing experiment (Figure 3.11(b)) showing that *p*-light of all TFGs has similar insertion loss. With the resolution set at 1 pm from the tuneable laser, more fine spectra were obtained showing the existence of ghost mode and the 2nd order Bragg resonance (see arrows in Figure 3.10(b)) which will be discussed in detail in next section.
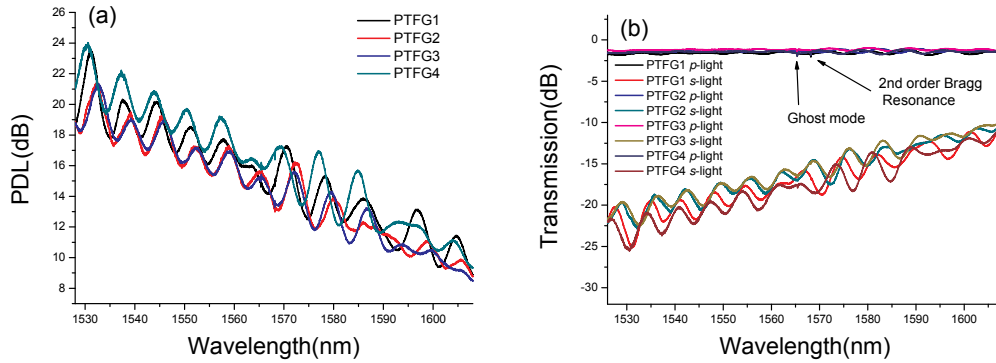
Figure 3.11 (a) PDL and (b) transmission spectra indicating insertion loss of the 45º-TFGs in Figure 3.10 after 24 hours thermal annealing at 80 °C.

Thermal annealing is a standard treatment for fibre gratings to stabilise their properties as grating thermal decay may occur if annealing has not been conducted. In order to evaluate the annealing effect on 45º-TFGs, all four gratings have been put in a thermally stable oven at 80 ℃ for 24 hours. The measured results after annealing are shown in Figure 3.11. Compared to Figure 3.10, it can be seen that all four gratings have a small decrease in PDL which is ~4 dB (only a few percents in linear scale). A more clear view is illustrated in Figure 3.11(b) manifesting that *p*-light (minimum loss) is nearly not affected by the thermal annealing process (i.e. still ~ 1.3 dB insertion loss) while the insertion loss of *s*-light (maximum loss) alleviated by ~4 dB.

3.3.4 2nd order Bragg resonance of 45º-TFGs

It has been noticed from Figure 3.10(b) and Figure 3.11(b) that there are two small narrow dips in the transmission spectra. One of the two dips locating at ~1568 nm is the 2nd order Bragg resonance (SBR) and the other is the ghost mode. It is well known that due to the saturation effect of the UV inscription, high order Bragg resonance can be observed in a non-tilted uniform FBG [156]. Some early work showed that 1st- and 2nd-order Bragg resonances can be used together in sensing application to distinguish the effects induced by temperature and strain simultaneously [157]. UV written 2nd order FBG via a double period phase mask for telecom application has also been reported [158].

A standard mathematical description of Bragg diffraction in a uniform FBG is defined

as

Equation 3.5 $\lambda_i = n_{eff} \cdot \dfrac{\Lambda_{eff}}{i}$

where λ_i is the resonance wavelength of FBG, $i = 1,2,3...$ is the diffraction order, n_{eff} is the effective index of the mode, and $\Lambda_{eff} = \dfrac{\Lambda}{\cos\theta}$ is the effective grating period. Λ is the phase mask pitch and θ is the angle between the phase mask pitch wave-vector and the fibre axis. Thus, theoretically a series of high order solution do exist for a given phase mask period without any tilt. Normally, the grating fringes induced by scanning the phase mask are regarded as a quasi-perfect sinusoidal refractive index change along the fibre axis. According to the Fourier series analysis, the sinusoidal function does not give out any high order periodic component. When the index change gets saturated, the refractive index tends to get a square-like shape, hence, producing high order periodic frequencies. For TFGs, it is actually much easier to get the higher order Bragg resonance. Physically because when the fringes tilted, they break the sinusoidal index profile along the fibre axis, therefore inducing higher order Fourier components. According to Equation 3.5, using effective index 1.45 and phase mask period 1800 nm, a theoretical SBR appears at 1568.59 nm which shows good agreement to our experimental observation. As for the ghost mode, it is a well known effect in weakly tilted uniform FBGs [159-160]. The ghost mode is explained as the mode coupling between the fundamental propagating mode and the low order cladding mode. Recently, the ghost mode has been applied as various sensors [161-162]. Yet, as the first observation of the ghost mode adjacent to the SBR, the origin of this ghost mode is still not clear. Since both the SBR and ghost mode have only been observed for p-light, the ghost mode may due to the coupling between the SBR and low order cladding mode which is facilitated by the tilted grating structure.

3.3.5 Refractive index and thermal response of 45º-TFGs

3.3.5.1 Refractive index response of the 45º-TFGs

As 45º-TFGs have a strong polarisation dependency which may be developed into in-fibre polarisation device, I further examined the refractive index (RI) and thermal response of the 45º-TFGs. It is found that when a 45º-TFG is immersed in the RI matching gel, the oscillation on PDL spectrum can be eliminated. As clearly seen in Figure 3.12(a), when the grating was surrounded by the RI matching gel (RI=1.456), the original oscillation feature on PDL disappeared and the PDL response became smooth across whole wavelength range, as shown by the red straight lines. The measured transmission spectra are shown in Figure 3.12(b) stating that the index matching eliminate the oscillation feature only for *s*-light while the *p*-light is not affected
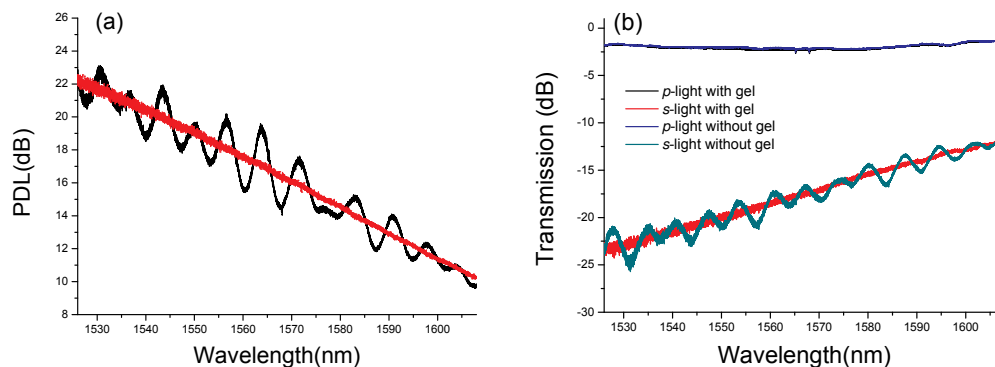
Figure 3.12 (a) PDL spectra of a 45º-TFG when exposed to air (black curve) and immersed in RI matching gel (red curve); (b) transmission spectra of the *p*-light and *s*-light when the same 45°-TFG exposed to air and immersed in RI matching gel. Note: transmission spectra of *p*-light are overlapped by each other when the grating exposed to air and immersed in RI matching gel.

The transmission spectral evolution of the 45º-TFG was further evaluated by immersing the grating into a set of certified RI gel (from Carillgon Lab) with RI value varies from 1.3 to 1.408 with an increment of 0.01 and from 1.428 to 1.64 with an increment of 0.08. Figure 3.13 illustrates the RI response of a 45°-TFG from air to

1.64, showing PDL and transmission spectra evolution. From Figure 3.13(a), we can see that the PDL turns to be smooth when the RI increases from air to 1.45 which is close to the index of fibre cladding. When the RI further increases to 1.64, although not significantly obvious, the oscillation appears again. Similar behaviour has been observed for the grating transmission spectra, as shown in Figure 3.13(b). This corresponds well to the explanation which has been made above, when RI difference between the cladding and outer medium is very small, the oscillation can be eliminated due to the equivalent effect of infinite fibre cladding. If this RI difference is large, radiated modes can oscillate between the cladding/outer medium boundary and the core. This principle applies to both PDL and transmission spectra of the 45°-TFG. Therefore, it can be predicted that for RI value above 1.64, strong spectral oscillation may occur due to the strong refractive index mismatch between the cladding and RI gel.

Although the 45°-TFGs may not be suitable for RI sensing, using coating with a similar RI to the fibre cladding can eliminate the oscillation and get a smooth PDL (or PER) response, which is desirable for polarisation devices and applications.
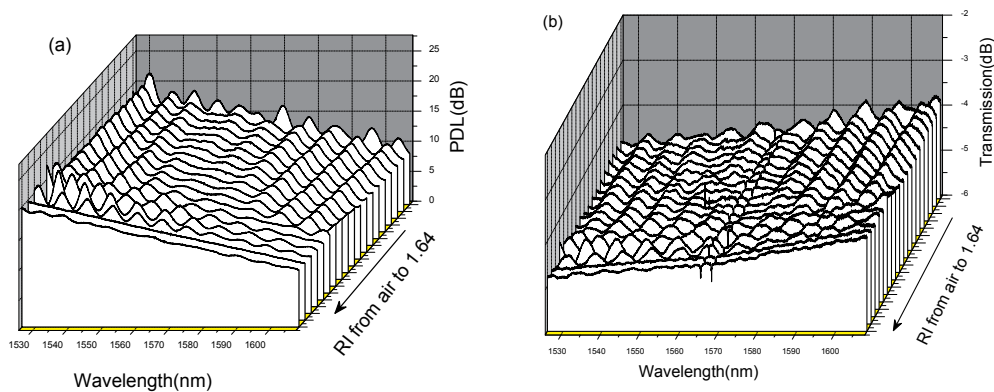
Figure 3.13 (a) PDL and (b) transmission spectra of the 45°-TFG when immersed in various RI gels at 1(air), from 1.3 to 1.408 with an increment of 0.01 and from 1.428 to 1.64 with an increment of 0.08

3.3.5.2 Thermal responses of the 45º-TFGs

A 45º-TFG was firstly examined without the RI matching gel under elevated temperatures from 10°C to 60°C with a 5°C increment, and the device was further examined when immersed in the RI gel. The measured PDL and transmission spectra are shown in Figure 3.14.
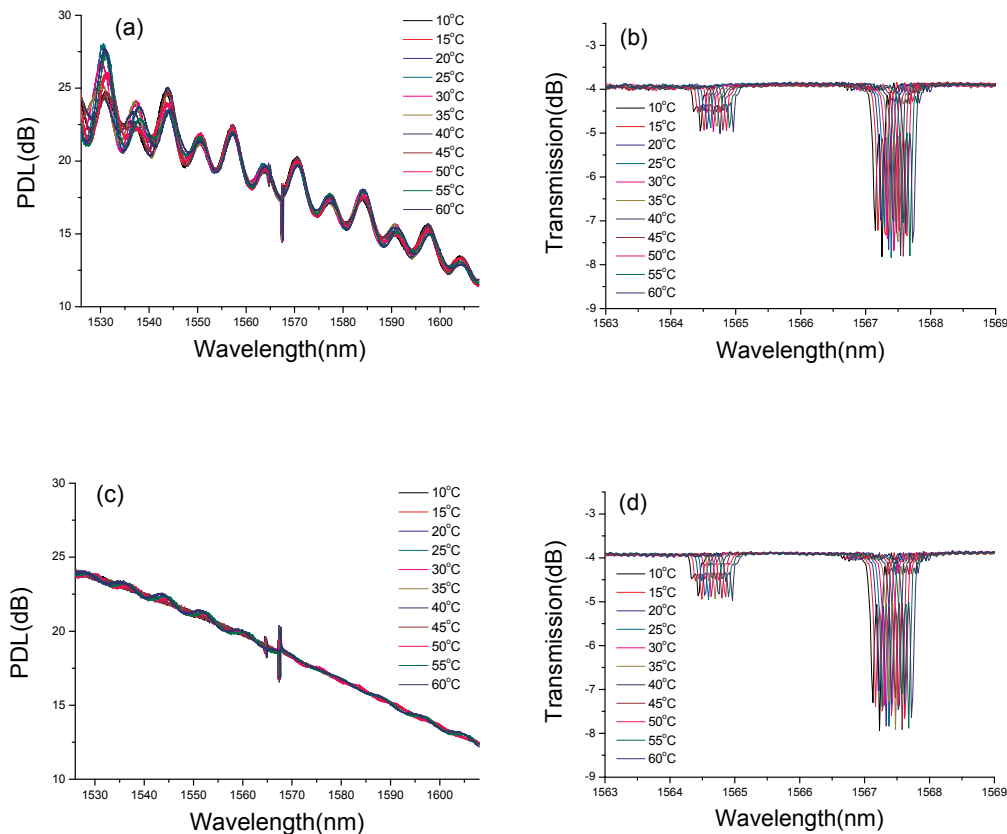
Figure 3.14 Thermal responses of the 45º-TFG for PDL and transmission when the grating is exposed to air (a) and (b) and immerged in RI gel (c) and (d).

Figure 3.14(a) and (c) indicate that when a 45º-TFG is heated up, its PDL does not have noticeable change. There is also no obvious amplitude fluctuation regarding the transmission spectra which can be seen from Figure 3.14(b) and (d). Due to the thermal condition change applied to the grating, from Figure 3.14(d), noticable shifts of the SBR and the ghost mode, similar to normal fibre Bragg gratings, can be observed. The thermal responses of the ghost peak and SBR have been evaluated

accordingly and are shown in Figure 3.15. From the figure, it can be seen that when the 45 º-TFG is exposed to air, the thermal sensitivities of the ghost mode and SBR are ~9.95 and ~9.47 pm/ºC respectively. When the grating is immersed in the RI matching gel, the corresponding thermal sensitivities are measured to be ~10.5 and ~10.02 pm/ºC, increased by a small fraction. But in general, the temperature sensitivity of the ghost and SBR are in the same order (i.e. < ~10.6 pm/°C) to the first order Bragg resonance [163]. The ghost mode is slightly more sensitive to temperature than the SBR. This may be due to the different thermal optic coefficient between the fibre core and cladding, thereby changing the cladding mode phase matching condition for the ghost mode.
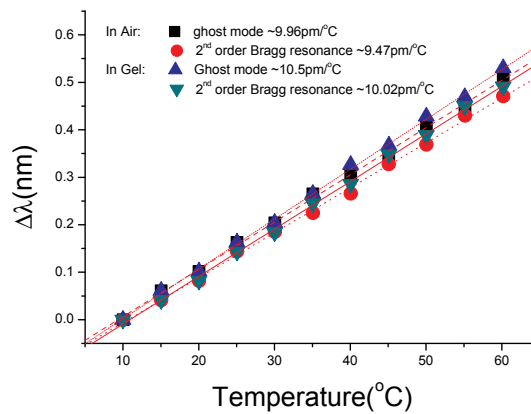
Figure 3.15 Thermal responses of the ghost mode and SBR of the 45º-TFG.

3.4 Fabrication and Characterisation of 45º-TFG at 1.06 μm Region

Recent development on Ytterbium doped fibre lasers working around 1.06μm region has attracted a lot of interests due to their inherent high gain compared to the Erbium doped fibre laser systems. Particularly in high energy pulsed lasers, polarisation can play important role [164]. The very recent activity in fibre laser and amplifier based on coherent beam combing requires polarisation control [165]. Therefore, exploration of polarisation effects and function of 45°-TFGs may offer alternative insights to the relative topics.

In this section, it is mainly focused on the fabrication of 45º-TFGs at 1.06 μm region, because there was no broadband source available for this wavelength range, PDL characteristics have only been examined using single wavelength source. Various fibres including standard and B/Ge co-doped photosensitive single mode fibres and conventional PM fibres have been investigated. The phase mask used for 45°-TFG at 1.06 μm inscription was purchased from IBSEN, having a period of ~1220 nm and a tilted pattern at ~33.7º. The effective mask length along the fibre axis is ~49 mm corresponding to the inscribed grating length. Because the phase mask for 1.06 μm region has smaller pitch than the one used for 1.55 μm region, the size of the UV interference area is further reduced according to the description in Figure 3.4. In other words, the interference trapezium will have a smaller value of L. It should be noticed that even in the case of uniform FBG inscription (Figure 3.4(a)), the portion of the UV beam next to the interference region may "bleach" the fibre core so as to reduce the effective photosensitivity of the optical fibre for grating inscription. In the case of tilted mask scanning inscription (Figure 3.4(b)), this "bleach region" is inversely proportional to the mask period. For 1.06 µm 45°-TFG inscription, the phase mask has a smaller period than that of 1.55 µm, it is therefore expected the "bleach" region becomes larger. Thus, defocused the UV beam to ~2 mm was adopted in order to make sure the UV beam fringes can cover most area of the fibre core. As discussed in section 3.2.3, defocus the laser beam on the fibre will reduce UV inscription intensity, hence, high UV laser power was increased for 45°-TFG inscription at 1.06 µm region. For characterisation, owing to the availability of equipment, we only performed the PDL measurement at single wavelength using a home-made Ytterbium doped fibre laser (YDFL) lasing at ~1055.8 nm. The schematic of the PDL measurement system is shown in Figure 3.16.
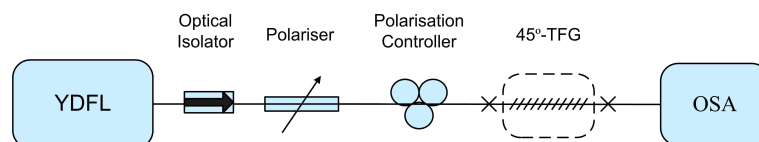
Figure 3.16 Schematic of PDL measurement system with a home-made YDFL.

In this system, an optical isolator which can provide >26 dB signal isolation at 1060

nm±30 nm is placed after the YDFL to prevent any unwanted reflection back to the laser cavity in order to maintain stable laser output. Similar to Figure 3.8(a), a commercial polariser and a set of PC were used to enable the manipulation of polarisation of the probe light for 45°-TFG evaluation. An OSA was used to record the PDL spectra.

3.4.1 45°-TFG at 1.06μm region in conventional single mode fibres

Two types of conventional fibre have been investigated including telecom fibre (Corning ®SMF-28) and commercial photosensitive fibre (Fibercore® PS1250/1500). Figure 3.17 shows typically measured spectra of the 45°-TFGs inscribed in these two fibres. It can be seen that the 45°-TFG inscribed in photosensitive fibre achieved a higher PDL (~20 dB) than in SMF-28 fibre (~12 dB).
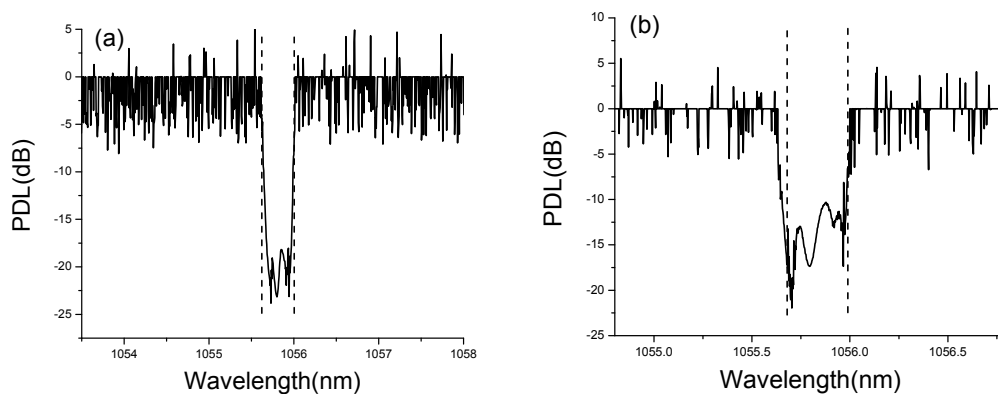
Figure 3.17 Measured typical PDL spectra of 45°-TFG at 1.06 μm region in (a) commercial photosensitive fibre and (b) SMF-28 fibre. Note: as the laser was set at 1.055 μm, only the section between the two dotted lines in the plot is the correspondent PDL.

In order to identify the fabrication condition to achieve high PDL, we have then fabricated a number of 45°-TFGs in these two types of fibre. Three 45°-TFGs were inscribed using SMF-28 fibre with ~ 150 mW UV illumination power. With a minimum laser beam scan speed of 0.04 mm/s, a maximum PDL of ~ 5 dB was obtained. Another five 45°-TFGs were inscribed using SMF-28 fibres with ~ 240 mW UV illumination power. Under the same scan speed of 0.04 mm/s, a maximum PDL of ~ 17 dB was achieved for all five gratings. As 0.04 mm/s is the minimum scan speed we can drive the stage, this suggests that stronger 45°-TFGs may be possible

obtained by using photosensitive fibres.

Four 45º-TFGs were therefore UV-inscribed on photosensitive fibre (PS1250/1500) to explore the condition for obtaining strong PDL. Compared to 45º-TFGs inscribed in SMF-28 fibre, it can be seen that in photosensitive fibre, >20 dB PDL can be easily achieved with much less UV illumination power, i.e. ~ 80 mW. Using the minimum scan speed of 0.04 mm/s, the grating inscribed in photosensitive fibre exhibited ~ 27 dB of PDL. Increasing the scan speed to 0.06 mm/s and 0.08 mm/s, the obtained PDL was ~ 22 dB and ~ 19 dB, respectively. This result indicates that strong 45°-TFGs at 1.06 μm region can be achieved. A double exposure has also been tried to achieve high PDL, however significant degradation in PDL has been observed. Again, this could be attributed to the environmental variation induced unstable grating inscription. Therefore, it has been concluded that to fabricate strong 45º-TFGs at 1.06 μm should be either employing photosensitive fibres or using high UV power. With more fine adjustment of inscription parameters, high quality and reproducible 45º-TFGs can be obtained with PDL as high as ~35 dB are possible, as this has been demonstrated by other colleague recently.

3.4.2 45º-TFGs at 1.06 μm region in polarisation maintaining fibres

Polarisation maintaining (PM) fibres are designed to transmit light with maintained linear polarisation. They have wide applications in telecom, sensors and lasers because of their polarisation state preservation property. For the first time, investigation on the 45°-TFG inscription in PM fibres are presented in this thesis. These unique devices may lead to potential application as the integrated fibre polariser for fibre laser and sensor systems.

As described earlier, strong 45º-TFG structures giving PDLs close to 30 dB may be achievable in the fibres with sufficient photosensitivity. Although the standard telecom fibre has less photosensitivity, the 45°-TFGs have been inscribed in it achieving PDL close to ~20 dB, when the fibre being H_2-loaded and using much higher UV power. This has encouraged the attempt to UV-inscribe 45°-TFGs in standard (non photosensitive) PM fibres.

3.4.2.1 Specification of the polarisation maintaining fibres

Two types of PM fibre have been investigated for 45º-TFGs inscription. These types of PM fibre are commercially available PANDA type fibre (from OFS). The geometry properties of the investigated PM fibres were examined and measured using a commercial microscope system (Carl Zeiss Axio). The cross-section images of these two PM fibres are shown in Figure 3.18.
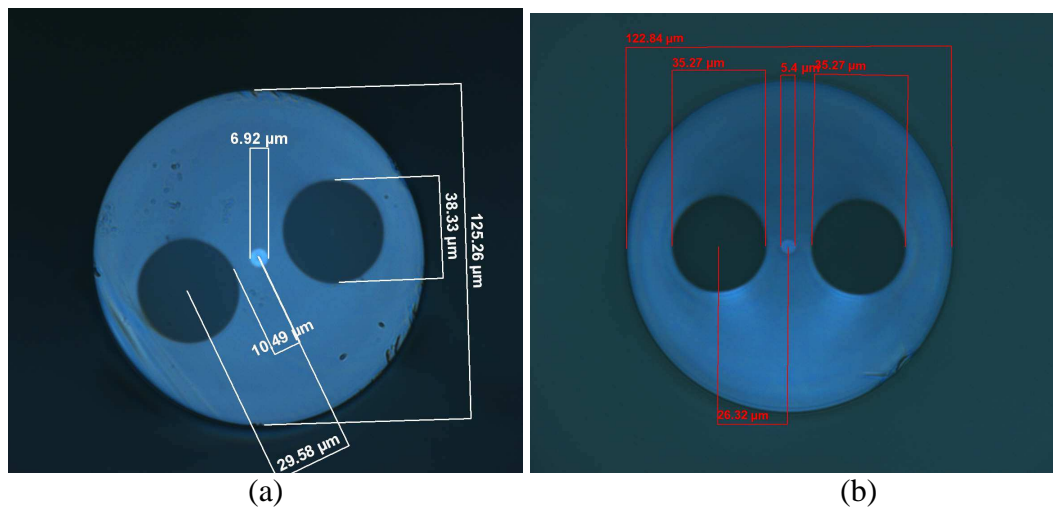
Figure 3.18 Cross-section images of the two investigated PM fibres (a) OFS PM_125L type fibre; (b) OFS TruePhase® 980 fibre.

The measured parameters of the two fibres are listed in Table 3-1. Through this section of the thesis, for simplicity, the OFS PM-125L type fibre will be referred as PM125L and the OFS TruePhase® 980 type as TP980.

Table 3-1 Geometry Parameters of the two PM Fibres.

Fibre Code	Core Diameter	Cladding Diameter	Rod Diameter	Rod Offset to Core
PM125L	6.92µm	125.26µm	38.33µm	10.49µm
TP 980	5.4µm	122.84µm	35.27µm	26.32µm

For PM125L and TP980 fibres, they are standard PANDA structure single mode PM fibres with a fibre core sandwiched between two large size stress rods (namely stress applying parts). The stress rods are normally made by Boron doped low refractive

index glass which exhibits different thermal expansion coefficient from the cladding of the optical fibre.

3.4.2.2 Fibre Bragg grating fabrication on PM125L and TP980 fibres

In order to assess the photosensitivity of PM125L and TP980 PM fibres, normal FBGs were first inscribed onto these two fibres and compared with the FBG written in a standard telecom fibre. The two PM and SMF-28 fibre samples were H_2-loaded under 180 bar at 80 ºC for 72 hours prior to the UV-inscription to enhance the photosensitivity. The standard phase mask scanning technique was employed to fabricate the FBGs. Because the PM fibres have two principal axes namely fast- and slow-axis, we have inscribed FBG structures along the two axes and also along the direction 45° to the two axes to see if there is fibre inscription direction dependency in the PM fibres. The schematic diagram of the inscription arrangements along the three different directions is shown in Figure 3.19.
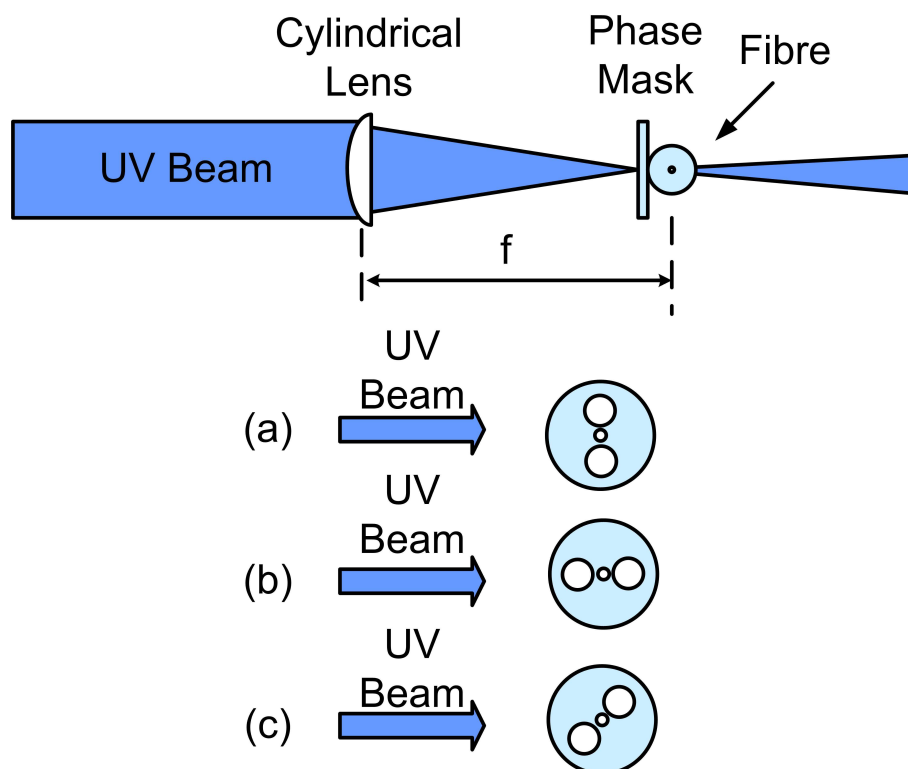
Figure 3.19 Schematic diagram of an FBG inscription with respect to PM fibre orientations, along: (a) fast-axis; (b) slow-axis; (c) 45º direction.

In order to evaluate the photosensitivity of PM125L and TP980, five FBGs were UV-inscribed in the two PM fibres and one FBG in SMF28 fibre were fabricated under the same inscription condition for comparison. Before the UV-inscription, all PM fibre samples had been properly marked with the axis directions under a microscope, which were used as the fibre orientation reference for the inscription. After the inscription, all FBG fibres were annealed under 80 ℃ for 24 hours for stabilisation. The FBGs on PM125L, TP980 and SMF-28 fibres were characterised with a commercial measurement system with a resolution of 20 pm (LUNA Technologies) before and after the annealing. Figure 3.20(a) and (b) plot the Bragg reflections (PDLs) for the two FBGs made in PM125L and TP980 Pm fibres and (c) depicts the typical spectra of FBG made in SMF-28 fibre.
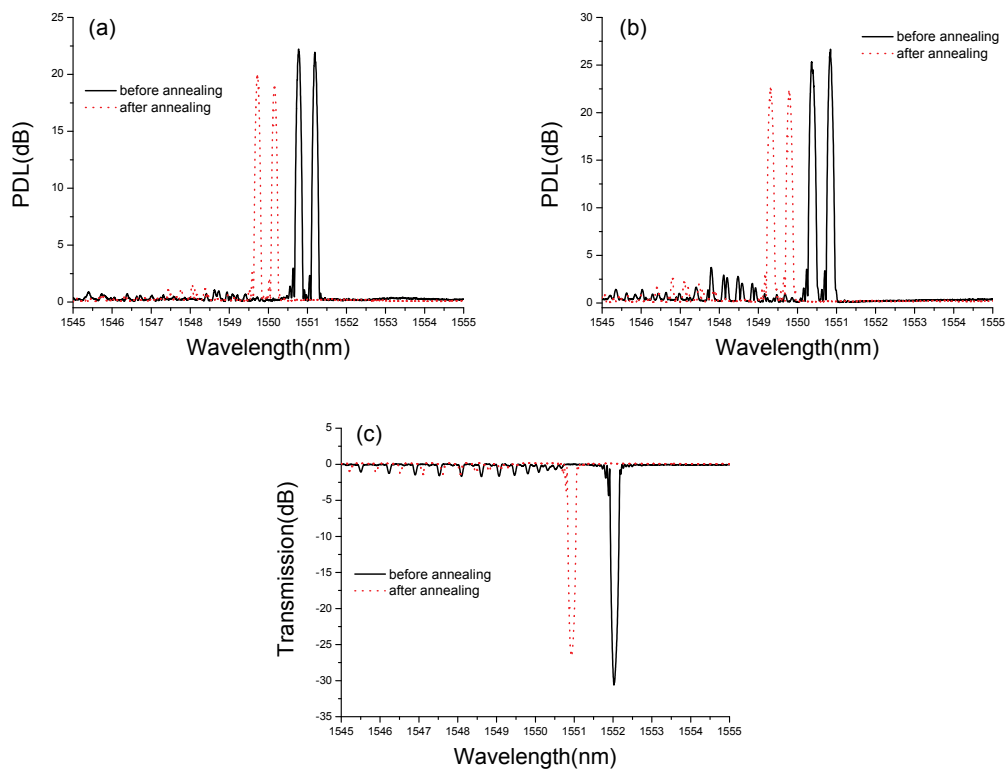
Figure 3.20 Typical transmission spectra of FBGs before and after annealing inscribed in (a) PM 125L; (b) TP980; (c) SMF-28 fibres. Note: there are dual peaks in the PM fibre, corresponding to the two orthogonal polarisation modes.

From Figure 3.20(a) and (b), we can clearly see that there are two Bragg reflection peaks in the PM fibres corresponding to the two orthogonal polarisation states. These

dual peaks can only be fully excited when the launched light is fully polarised in the individual orthogonal directions, whereas there is only one Bragg peak for the SMF-28 fibre due to its relatively low birefringence, as shown in Figure 3.20(c). Hence, the real strength of UV inscribed FBGs in PM fibres can only be resolved when they are probed by linearly polarised light. Generally speaking, all FBGs became slightly weaker after the annealing treatment and the annealing treatment also led to a blue-shift of the Bragg peak. This blue-shift is mainly caused by the out-gas H_2, resulting in a lower average refractive index change. Detailed information about the reflectivity and inscription direction for 5 FBGs are listed in Table 3-2. From the Figure 3.20 and Table 3-2, it can be seen that the FBG strengths in the PM fibres are as high as that (~30 dB) in SMF-28 fibre if the UV-inscription is along the fast-axis and a bit lower if along the slow-axis of the PM fibre. However, if the UV-inscription is along 45° direction of the PM fibre, the grating strength becomes even lower (only ~15 dB). These results indicate that the PM fibres may have sufficient photosensitivity after the H_2-loading treatment while using high UV power, 45°-TFGs of high PDL may be produced in the two PM fibres.

Table 3-2 Reflectivity of FBGs inscribed in two PM and SMF-28 fibres

Grating Code	Fibre Type	Reflectivity (dB)	Inscription Orientation
FBG1	PM125L	20	Slow-axis
FBG2	PM125L	14	45°
FBG3	TP980	22	Slow-axis
FBG4	TP980	30	Fast-axis
FBG5	TP980	15	45°
FBG0	SMF28	27	N/A

3.4.2.3 Fabrication and PDL measurement of 45º-TFGs in PM fibres

According to the description in the beginning of section 3.4, the UV beam should be at slightly de-focus position. As shown in Figure 3.19 , in the UV-inscription system, we have moved out the cylindrical lens by Δf ~2mm from the focus position in order to expand the beam slightly. As indicated in the fabrication of FBGs, the fibre orientation should be also critical to the UV-inscription for 45°-TFGs in PM fibres. All PM fibre samples were marked with reference axis using a microscope system in order to set the fibre orientation correctly for oriented inscription.

In order to achieve high PDL, the UV inscription power has been increased to ~240 mW. The scan speed has been kept the same as 0.04mm/s while single scan was employed to maintain the reproducibility of the gratings. For both types of PM fibre, 45°-TFGs have been inscribed at the three designated axis (i.e. slow-axis, fast-axis and 45°-oriented). It can be seen from Table 3-3 and Table 3-4 that with the high UV power, high PDL values can be obtained (i.e. ~ 16 dB). Therefore, for 45°-TFGs inscribed in PM fibres, two major conclusions could be drawn indicating that: fast- and slow-axis inscription tend to give high PDL (~ 16 dB for slow-axis, ~8 dB for fast axis), while 45° is the most difficult orientation for strong grating inscription (~ 2 dB); second, with single scan, the grating inscription is also reproducible. However, this observation contradicts to our results from FBG inscription in PM fibres (section 3.4.2.2) from which strong FBG is shown in fast-axis inscription.

Table 3-3 45°-TFGs fabrication condition and PDL on PM125L fibres.

Grating Code	Fibre Type	PDL	Inscription Orientation
P1	PM125L	16dB	slow-axis
P2	PM125L	15dB	slow-axis
P3	PM125L	8dB	fast-axis
P4	PM125L	6dB	fast-axis
P5	PM125L	2dB	45°-Oriented
P6	PM125L	2dB	45°-Oriented

Table 3-4 45°-TFGs fabrication condition and PDL on TP980 fibres.

Grating Code	Fibre Type	PDL	Inscription Orientation
P7	TP980	16dB	slow-axis
P8	TP980	14.8dB	slow-axis
P9	TP980	8dB	fast-axis
P10	TP980	8dB	fast-axis
P11	TP980	2.5dB	45°-Oriented
P12	TP980	2.9dB	45°-Oriented

This could attribute to the geometrical structure of the PM fibre. As the stress rods applying parts (SAP) of the PM fibres are cylindrical, hence for slow-axis inscription, they may behave like a lens which could distort the fringe image in the fibre core. The fringe distortion would alternate the tilted angle in the fibre core from which central resonance wavelength of the 45°-TFG would vary. Paraxial analysis similar to that in

reference [11] for 45°-TFG inscription in PM fibre has been carried out to estimate the fringe distortion. As it is interested to determine the alternated tilted fringe angle through the SAP in the fibre core, the image fringe generated in the fibre core is considered to be produced at the flat surface of a half cylindrical lens through a build-in full cylindrical lens. Figure 3.21(a) depicts schematic of the paraxial ray tracing for calculating the fringe distortion. In Figure 3.21(a), n_1, n_2 are the refractive indices of the cladding and SAP respectively, where generally the relationship $n_2 < n_1$ applies. This is because the SAP is normally made by Boron doped silica which has higher thermal expansion coefficient and lower refractive index than those of the cladding. R_1 is the radius of the fibre cladding which is positive. R_2 and R_3 are the radius for the left and right hand side of the SAP part, where R_2 is positive and $R_3 = -R_2$. MN denotes the object size, it is the fringe height pass the phase mask in this case. In the following calculation, the sign convention is indicated by superscripts + or − where ± means unknown.
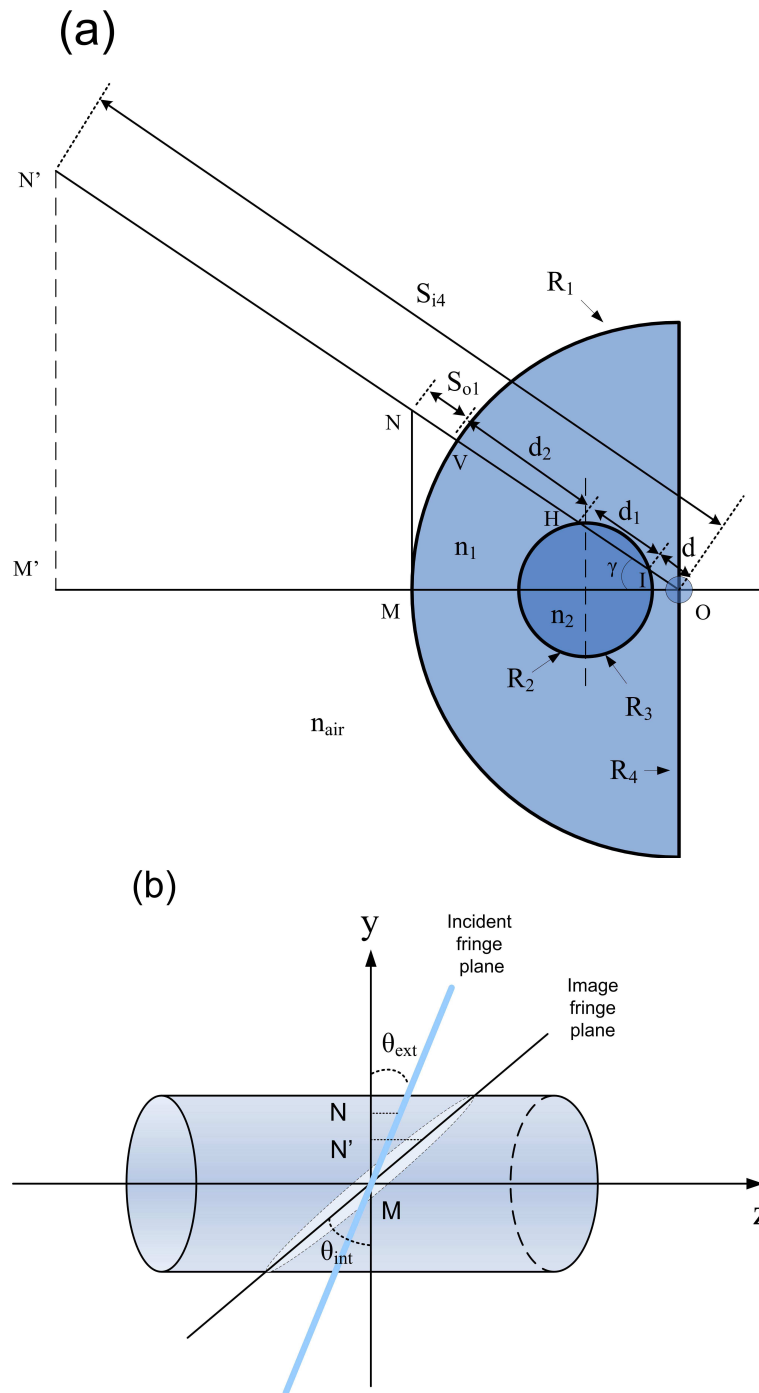
Figure 3.21 (a) Paraxial ray tracing through a half cylindrical lens with build-in full
cylindrical lens; (b) schematic description of fringe distortion in the fibre core.

First, let us consider the image by the fibre cladding with a radius R_1. Using the thin-
lens equations, then have:

Equation 3.6 $\dfrac{n_{air}}{S^+_{o1}} + \dfrac{n_1}{S^{\pm}_{i1}} = \dfrac{n_1 - n_{air}}{R^+_1}$

With $n_{air}=1$, S_{o1} (NV) is the object distance, it can be deduced that

$S^-_{i1} = \dfrac{n_1 \cdot R_1 \cdot S^+_{o1}}{(n_1 - 1)\cdot S^+_{o1} - R_1}$. Because of using the paraxial approximation, the

relationship $S^+_{o1} \ll R^+_1$ is true, it is therefore to have a virtual image with negative S_{i1} value. The next step is to examine the image formed by the left surface of the SAP, the object distance with respect to point H is given by:

Equation 3.7 $S^+_{o2} = \left| S^-_{i1} \right| + d^+_2 = \dfrac{d_2 \cdot \left(R_1 + S^+_{o1} \right)}{d_2 - (n_1 - 1)\cdot S^+_{o1}}$

When $S^+_{o1} \to 0$, we will have $S^+_{o2} \cong d^+_2$. At the left surface of SAP, apply the thin-lens equation again:

Equation 3.8 $\dfrac{n_1}{S^+_{o2}} + \dfrac{n_2}{S^{\pm}_{i2}} = \dfrac{n_2 - n_1}{R^+_2}$

we can then derive:

Equation 3.9 $S^-_{i2} = \dfrac{n_2 \cdot R^+_2 \cdot S^+_{o2}}{S^+_{o2} \cdot (n_2 - n_1) - n_1 \cdot R^+_2}$

Equation 3.9 then can be used to calculate the object distance through the right surface of the SAP giving that $S^+_{o3} = \left| S^-_{i2} \right| + d^+_1$. In the paraxial approximation, when

$S^+_{o1} \to 0$, we will have $d^+_1 \cong 2 \cdot R^+_2$ therefore :

Equation 3.10 $S^+_{o3} = \dfrac{2 \cdot R^+_2 \cdot d^+_2 \cdot \Delta - 2 \cdot R^{+^2}_2 - (1+\Delta) \cdot R^+_2 \cdot d^+_2}{d^+_2 \cdot \Delta - R^+_2}$

Where $\Delta = (n_2 - n_1)/n_1$ is the refractive index difference between the cladding and the SAP part in percentage. When applying the thin-lens equation at the right surface of the SAP:

Equation 3.11 $\dfrac{n_2}{S^+_{o3}} + \dfrac{n_1}{S^{\pm}_{i3}} = \dfrac{n_1 - n_2}{R^-_3}$

From Equation 3.11, recall $R^+_2 = -R^-_3$ it can be derived that:

Equation 3.12

$$S^-_{i3} = \dfrac{-R^+_2 \cdot [2 \cdot R^+_2 \cdot d^+_2 \cdot \Delta - 2 \cdot R^{+^2}_2 - (1+\Delta) \cdot R^+_2 \cdot d^+_2]}{-\Delta \cdot [2 \cdot R^+_2 \cdot d^+_2 \cdot \Delta - 2 \cdot R^{+^2}_2 - (1+\Delta) \cdot R^+_2 \cdot d^+_2] + (1+\Delta) \cdot R^+_2 \cdot (d^+_2 \cdot \Delta - R^+_2)}$$

Hence, the object distance through the flat surface is given by:

Equation 3.13 $S^+_{o4} = \left| S^-_{i3} \right| + d^+$

Now using the Gauss formula with $R_4^+ = \infty$ for the flat surface,

$$\text{Equation 3.14 } \frac{n_1}{S_{o4}^+} + \frac{n_{air}}{S_{i4}^{\pm}} = \frac{n_{air} - n_1}{R_4^+}$$

Therefore, we have $S_{i4}^- = -\dfrac{S_{o4}^+}{n_1}$

Now, if we consider the front view of the incident fringe and its image in the core as shown in Figure 3.21(b), we will have:

$$\text{Equation 3.15 } \tan\theta_{ext} = \frac{h}{(R_1^+ + S_{o1}^+) \cdot \sin\gamma}$$

$$\text{Equation 3.16 } \tan\theta_{int} = \frac{h}{\left|S_{i4}^-\right| \cdot \sin\gamma}$$

Where h is the displacement of the incident fringe plane from the normal of the z-axis. From Equation 3.15 and Equation 3.16, the distorted fringe image angle can be calculated as :

$$\text{Equation 3.17 } \theta_{int} = \tan^{-1}\left(\frac{R_1^+}{\left|S_{i4}^-\right|} \cdot \tan\theta_{ext}\right)$$

Refer to PM125L fibre (Figure 3.18(a)), the measured fibre parameters are $R_1^+ = 62.5\mu m$, $R_2^+ = 19.1\mu m$, $d^+ = 10.49\mu m$, $d_2^+ = 13.82\mu m$, $\Delta = -0.005$, take $n_1 = 1.51$, the resulted internal grating fringe angle is ~ 45.65°. For TP980 fibre (refer to Figure 3.18(b)), the measured fibre parameters are

$R_1^+ = 61.4 \mu m$, $R_2^+ = 17.64 \mu m$, $d^+ = 8.68 \mu m$, $d_2^+ = 17.44 \mu m$, the calculated resulted internal grating tilt angle is ~ 45.38°. Remember that according to the VCM simulation, the change in grating tilted angle could lead to variation of central resonance wavelength i.e Figure 2.4(d). Figure 3.22 demonstrates the VCM simulated results of spectral response against PDL for gratings tilted at 45° and 45.6°. The simulation has been optimised to fit for the spectral response of the 45°-TFG at 1.06 µm which may have a red shift in resonance central wavelength due to the potential different effective modal index from theory calculation. It can be clearly seen that the grating tilted at 45° has a PDL of ~8 dB with ~12 dB PDL at 45.6° when the probe wavelength is set at 1.055 µm, which is the central wavelength of the home made YDFL. This simulation shows good agreement with the experimental observation of 45°-TFG inscribed in PM fibres from which slow-axis inscription lead to stronger 45°-TFG than fast-axis inscription. However, due to the lack of BBS at 1.06 µm region at the current stage, further confirmation and support of the theory will be left for future work.
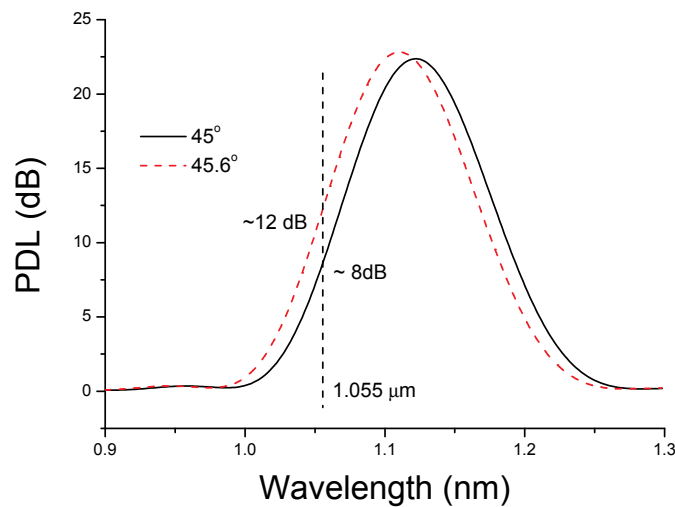
Figure 3.22 Spectral response against PDL for grating tilted at 45° (black solid line) and 44.2° (red dashed line) showing change of PDL at designed resonance wavelength. The black dashed line crosses the two PDL spectra depict the difference in PDL at the probe wavelength of 1.055 µm when using the YDFL.

3.5 Fabrication and Characterisation of Ex 45º-TFGs

3.5.1 Introduction

Tilted gratings with tilted angle >45° (ex 45º-TFG) have been reported very recently [114]. They behave like LPGs which couple the light from core modes to forward propagating cladding modes, but only to the high order ones, then resulting in a series of more densely distributed loss bands in transmission. These newly designed fibre gratings have index fringes excessively tilted with respect to the fibre axis which induce strong birefringence. Therefore, we may identify the equivalent fast- and slow-axis relative to the fringe plane for ex 45°-TFGs, as shown in Figure 3.23.
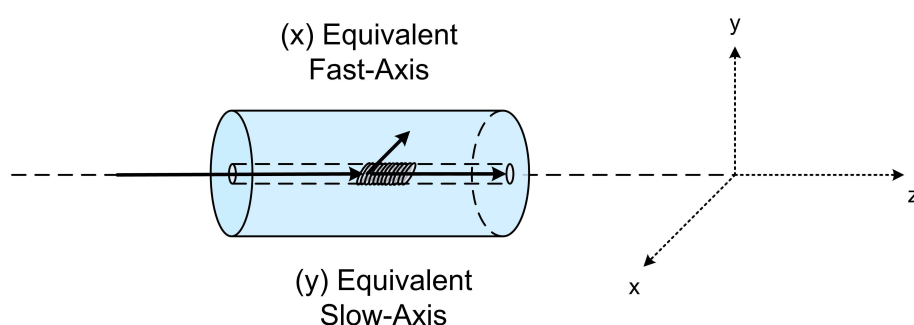
Figure 3.23 Schematic diagram of an excessively tilted grating structure with two assigned orthogonal polarisation axes.

Due to the strong birefringence effect induced by the ex 45°-TFG, polarisation mode splitting effect is anticipated to occur. In research work presented here, this type of TFGs was fabricated with excessively tilted structure at around 78° in the fibre core. These gratings were then used as sensors and polarisation loss filters in later work.

3.5.2 Fabrication of ex 45º-TFGs

Ex 45°-TFGs with strong spectral profile can be UV inscribed in H_2-loaded SMF-28 fibre. Different from 45º-TFGs fabrication, for ex 45º-TFGs inscription, an amplitude mask was employed. We adopted the same fabrication configuration as described in

Figure 3.1(a). A commercial amplitude mask (from Edmund Optics Ltd) with a period of 6.6 μm was purchased for ex 45º-TFG inscription. Owing to the limited size of the amplitude mask, the effective exposure length of the fibre is only ~12 mm. In the experiment, the amplitude mask was tilted at ~73˚ to induce in-fibre fringes blazed at ~78˚. A typical microscopic image of the 78º-TFG under 100× oil immersion objective lens is shown in Figure 3.24. The spectra of the fabricated 78°-TFGs were examined by the use of a similar setup depicted in Figure 3.7(a).
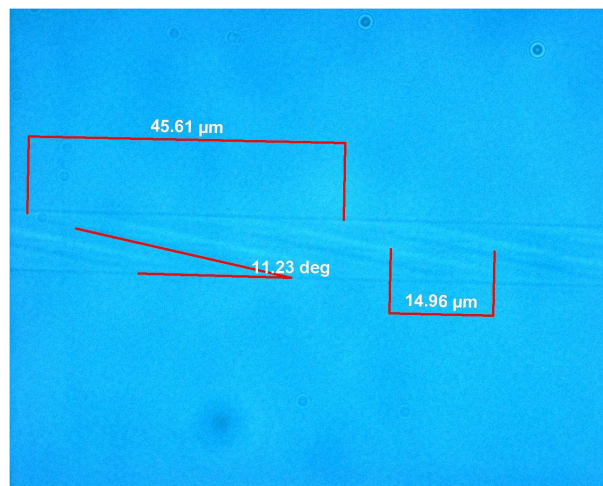
Figure 3.24 Microscope image of a 78º-TFG examined by a 100× oil immersion microscopic lens.

3.5.3 Spectral characterisation and PDL measurement of ex 45º-TFGs

The measured transmission spectra of 78º-TFGs show a series of paired loss bands in the wavelength range from 1200 nm to 1700 nm, as shown in Figure 3.25(a). The pair feature is a clearly evidence of polarisation mode splitting. Initially, because the probe light was un-polarised, two sets of mode with orthogonal polarisation states were more or less equally excited, as all paired peaks are about 3 dB in strength (Figure 3.26 (a)). We then used the combination of a polariser and a polarisation controller between the broadband source and the 78º-TFG to excite the modes with selective polarisation. As zoomed one paired peaks shown in Figure 3.25(b), when the probe light is polarised, either the equivalent fast- or the slow-axis mode can be fully excited or eliminated. For a fabricated 78°-TFG, the full strength of the loss peak reached ~10 dB when it was fully excited. In Figure 3.25(b), the blue dash-dotted line indicates the fast-axis mode, while the dashed red line shows the slow-axis mode and the black

solid curve illustrates excitation of the two modes with un-polarised light.
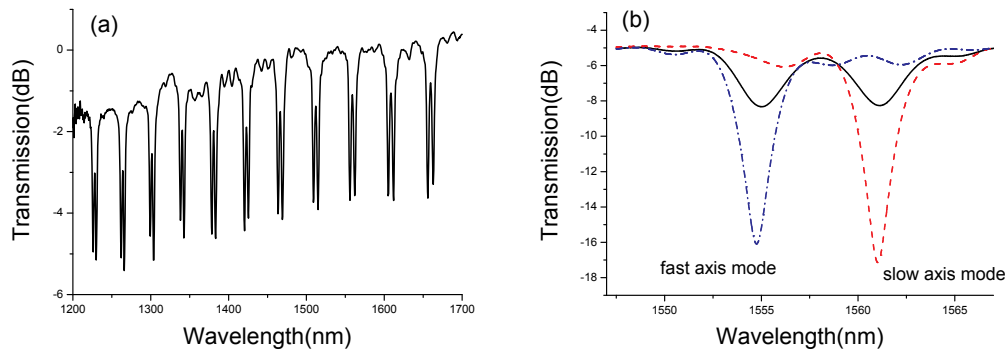
Figure 3.25 (a) A series of paired loss bands of a 78°-TFG in the range from 1200 nm to 1700nm measured using un-polarised light; (b) a paired loss peaks measured using polarised light showing full excitation and elimination of fast- and slow-axis modes.

3.5.4 Thermal and refractive index response of the ex 45º-TFG

3.5.4.1 Thermal response

The thermal response of the 78º-TFG has been evaluated by mounting the grating on a heat exchange plate while monitoring the transmission spectrum with temperature elevation. We examined two pairs of modes of the 78°-TFG around 1560 nm and 1610 nm. Figure 3.26 plots the wavelength shift of the two paired loss peaks when the grating was heated from 20 ℃ to 80 °C. Due to the involvement of an extra polariser and polarisation controller for characterisation with the low power response of the light source at the interested wavelength region, the measured loss peaks almost reach the sensitivity limit of the OSA. Considering the resolution of OSA as 0.02 nm, these produce an experimental error of wavelength reading 0.04 nm as stated in the error bars. As clearly shown in the figure, the temperature responsivities of the two paired loss peaks are quasi linear. The temperature responsivities of the fast- and slow-axis modes around 1560 nm are 4.5 pm/°C and 5.5 pm/°C (Figure 3.26(a)) while are 4.5 pm/°C and 7.5 pm/°C (Figure 3.26(b)) in the region around 1610 nm. Here we see that the temperature responsivity of the 78°-TFG shows dependency on mode orders, similar to the thermal behaviour of LPGs. We found in general the slow-axis mode has a higher temperature responsivity than fast-axis mode. The reason of this is still

unknown which will be left for future investigation.
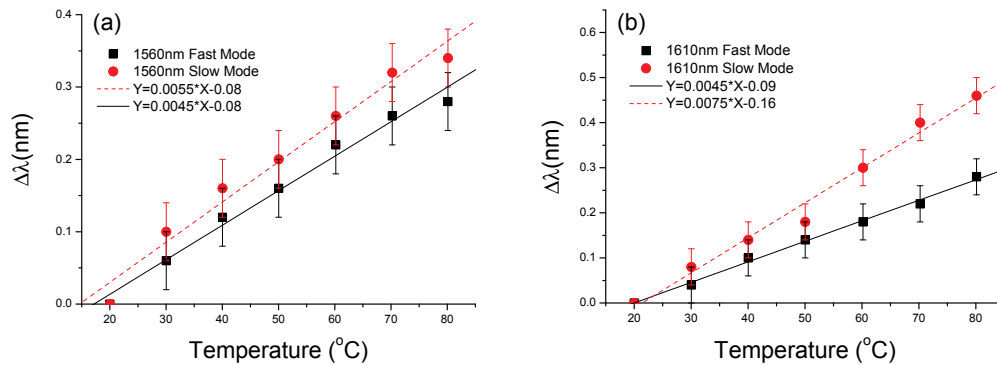
Figure 3.26 Wavelength shifts of two paired loss peaks of the 78°-TFG against the temperature change in the regions around (a) 1560 nm and (b) 1610 nm.

3.5.4.2 Refractive index response

Because the ex 45º-TFGs are able to couple the light from forward propagating core to cladding modes, they are intrinsically sensitive to RI of the external medium. The 78º-TFG was evaluated for RI sensing. The grating was fixed in a V-grooved aluminium plate to perform the RI evaluation experiment, which ensured the measurement free from other effects such as strain and bend. A series of certified commercial refractive index gel (from Carillgon Lab) were used to characterise the grating RI response. A BBS and an OSA were used to record the optical spectra for each RI. Figure 3.27 depicts the RI response of the two paired modes around 1560 nm and 1610 nm when the 78º-TFG was immersed in RI gels with RI change from 1.32 to 1.38 with an increment of 0.01. It can be seen that when the RI value increases, the dual loss peaks begin to degenerate. This is mainly due to the reduction of the cladding and outer medium RI difference. The decrease in RI difference reduces the polarisation mode dispersion (PMD) of the cladding modes. The RI response of the fast- and slow-axis mode employing polarised light for 1560 nm and 1610 nm band is shown in Figure 3.28. In general, for both bands, the total wavelength shift is ~ +20 nm from RI = 1.32 to 1.38, although the wavelength shift for 1610 nm band is slightly larger than that for 1560 nm band.
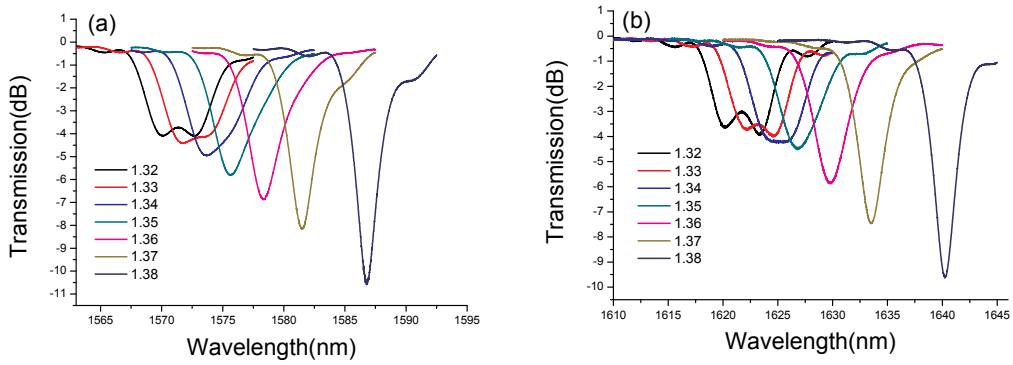
Figure 3.27 RI response of mode pair when subject into index gel from RI=1.32 to 1.38 with an increment of 0.01 for (a) 1560 nm band and (b)1610 nm band.

It is worthy to notice that the ex 45°-TFGs has strong RI response for the RI value around 1.3 which is different to that of the conventional LPGs [166]. This implies ex 45°-TFGs may be more suitable for bio/chemical sensing for water based solutions.
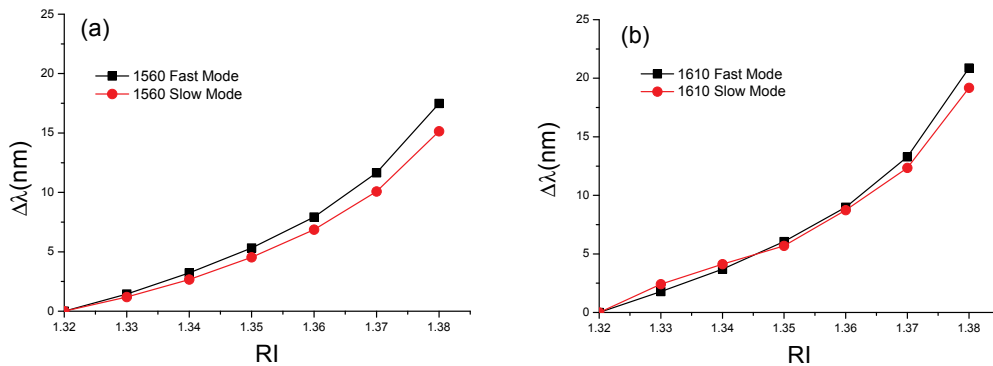
Figure 3.28 RI response of fast- and slow- modes around (a) 1560 nm and (b) 1610 nm when the 78°-TFG was subjected to index gels with RI change from 1.32 to 1.38 with an increment of 0.01.

Furthermore, it is noticed that for RI over 1.38, there is no more cladding modes coupling, only radiation mode coupling can be observed.

3.6 Chapter Conclusions

In this chapter, we have studied the structures, inscription technique, PDL, spectral, thermal and RI response characteristics of the 45º-TFGs and ex 45º-TFGs.

For 45º-TFGs, we have systematically studied the fabrication using the concatenation and single scan techniques at 1.5 μm region. The polarisation characteristics have been investigated thoroughly using various methods. The 45º-TFGs achieved high PDLs have shown function as in-fibre linear polarisers. I also explored the coupling between the 45º-TFG and PM fibres for which potential applications may emerge. 45º-TFGs exhibit thermal independency although annealing would decrease the PDL by a small amount. The observation the SBR from a 45º-TFG has been reported in this thesis. Characterisation of SBR has also been performed. Thermally induced SBR peak shifts and large PDL have been identified and a 45°-TFG with an SBR may be used to realise single-wavelength and single-polarisation operation of a fibre laser. I have found that the thermal sensitivity of SBR is smaller than that of a conventional FBG. It is also discovered that when a 45°-TFG is surrounded by medium with RI close to the fibre cladding, the oscillations on its PDL and spectral profiles can be eliminated. The RI response of the 45°-TFG has been explored and discussed.

For 45º-TFGs designed and fabricated for 1.06 μm region, although the initial trial was conducted on conventional photosensitive and SMF-28 fibres, we mainly focused on the investigation in PM fibres. It is found that slow-axis inscription produce higher performance than fast-axis inscription in the case of two types of conventional type PM fibres. Reproducible 45º-TFGs with ~16 dB PDL have been obtained with slow-axis inscription while only ~8 dB for fast-axis inscription. The reason for this has been explained by paraxial ray tracing analysis and VCM theory. 45°-oriented UV inscription proved to be less efficient for 45°-TFGs production. In general, it is has been proved that 45°-TFGs can be inscribed in conventional PM fibres successfully.

Finally, the fabrication and characterisation were performed on ex 45º-TFGs and several 78º-TFGs were UV-inscribed in low cost SMF-28 fibre, showing unique PM-like LPG property. The 78°-TFGs exhibited polarisation mode splitting effect, indicating significant birefringence induced by the excessively tilted grating structure in the fibre. It is noted that such ex 45°-TFGs show less thermal sensitivities than the

conventional FBGs. In terms of RI response, we found that the coupled relative high order cladding modes at the longer wavelength side have a slightly higher RI sensitivity. However, the RI response range of ex 45°-TFGs is around 1.32 to 1.38 which is quite different from that of LPGs, usually from 1.4 to 1.44. The down shift of the RI response range is mainly caused by the light coupling to the high order cladding modes in ex 45°-TFGs rather than to the low order ones in LPGs. Together with LPGs, this may be an advantage to broaden the entire liquid sensing range for bio/chemical sensing applications.

Chapter 4

45° and Ex-45° Tilted Fibre Gratings – On the Application of Erbium Doped Fibre Lasers

4.1 Introduction

Fibre lasers are very useful light sources in optical communication, optical sensing, and diagnostics etc. Due to the rapid development of optical communication, Erbium doped fibres (EDFs) showing strong emission at 1.5 μm region have attracted a lot of interest and been explored and utilised for a range of fibre lasers and amplifiers. Their advantages include the high compatibility, low cost, ease of fabrication etc, they also exhibit quite good mechanical and thermal stability. EDF based fibre lasers (EDFLs) have started to show their advantages over their conventional solid state counterparts.

Polarisation is an important property of the laser beam. Nevertheless, in fibre lasers, this topic hasn't led to extensive research yet. Therefore, generating polarised light within a fibre laser cavity is of great interest. From continuous oscillation to pulse formation, polarisation could play a significant role in light oscillation. Including a large birefringence element or an in-fibre polariser in the cavity is the most popular approach to drive a fibre laser to oscillate in single polarisation state. Tilted fibre grating (TFG) based asymmetric structure inherently increases the birefringence of the fibre laser system without breaking the format of optical fibre. Additionally, the tilted structures induced PDL makes them ideal in-line polarisation discriminators. This could further facilitate the polarised light formation in a standard laser cavity consisting of low-birefringence fibres.

In this chapter, the functionality of both the 45°- and ex 45°-TFGs in generating polarised light from fibre laser cavities has been investigated. With the polarisation effects induced through tilted gratings, both single- and multi-wavelength laser cavities have been exploited. In addition, a mode-locked fibre laser giving out femtosecond output pulse will be demonstrated which presents the polarisation application of 45°-TFG in nonlinear photonics.

4.2 Continuous Wave Fibre Lasers

4.2.1 Single polarisation single wavelength fibre laser

Polarisation, which is one of the fundamental properties of laser light, plays an

important role in some laser systems. A well-known effect that could affect the polarisation properties of the EDFL system is the polarisation dependent gain (PDG). This physical phenomenon origins from the anisotropic absorption of the Erbium ion in the optical fibres. Optical fibres made from glass are amorphous from which the ions are generally randomly oriented. The fact is, if the EDFL is pumped with linearly polarised light, the ions oriented parallel to the pump polarisation state absorb much more than those of the orthogonal orientation. Consequently, the gain could distinguish from different polarisation state which significantly depends on the anisotropy of the Erbium ions [167]. Experimentally, this effect had been examined by using a high birefringence EDF while in the meantime, a Muller matrix method had been developed to explain it theoretically [168].

Due to the intrinsic low-birefringence of the standard passive and active fibres, most of the fibre laser systems degenerate the two eigen-polarisation-states of the laser output. Using such fibres generally gives un-polarised output or, in other words, a very low degree of polarisation (DOP). This is undesirable in some applications for which single wavelength and single polarisation oscillation are required. To achieve single polarisation oscillation for fibre lasers, several methods have been proposed. One scheme involves the use of an integrated fibre polariser which adds complicity and loss to the structure [169]. Other approaches incorporate FBGs [142] or LPGs [170] written in high-birefringence (Hi-Bi) fibres. Recently, photonic crystal fibre (PCF) based devices have also been proposed to facilitate single polarisation fibre laser operation. McNeillie *et al*. have demonstrated a Hi-Bi PCF based single polarisation fibre laser [171] and a type of specially designed polarising PCF has also been used for implementing single polarisation fibre laser [172]. However, all these methods adopting specialty fibres impose high insertion loss to the cavity and, in addition, some devices such as PCFs are at high cost.

Recently, tilted fibre gratings inscribed in standard and photosensitive single mode fibres have been demonstrated as broadband in-fibre polarisers [13]. Based on the UV patterning of the fibre core through a phase mask, tilted fibre gratings may exhibit advantages over other types of polariser. In the work demonstrated here, we have proposed and demonstrated a single polarisation fibre ring laser utilising such an intra-cavity 45°-TFG made in conventional photosensitive fibre. The proposed laser

shows a very high DOP of >99.8%. The laser also showed a good stability as the variation of DOP was only about ~0.2% when the laser output was monitored continuously for 5 hours in laboratory conditions. The slope efficiency of the laser has been evaluated and we also demonstrated the tuneability of the output up to ~1 nm while keeping the highly polarised status.

4.2.1.1 Polarisation extinction ratio improvement

In order to evaluate the polarising function of the 45°-TFGs in fibre laser system, two 45º-TFGs which were discussed in Chapter 3 were adopted in the experiment. Both were fabricated via concatenation technique. TFG1 has a PDL of ~6 dB while TFG2 is ~30 dB. We constructed a standard fibre ring laser (as shown in Figure 4.1(a)) consisting of ~6 m EDF (from Lucent Technologies). Two polarisation independent optical isolators (OIS) are used to ensure single direction oscillation. The fibre laser is pumped through a 980/1550 wavelength division multiplexing (WDM) from a grating stabilised 975 nm laser diode (from SDL), which can provide up to 300 mW pump power. A 10:90 coupler is employed to couple 10 % of laser power out of the cavity. A uniform FBG which has a Bragg resonance at 1550 nm, a reflectivity of ~97 % and ~ 0.1 nm bandwidth is incorporated in the cavity through an optical circulator, providing a seed for single wavelength operation. The DOP of the laser output was measured with and without 45°-TFG. Figure 4.1(b) gives a typical output of the ring laser on the OSA.

(a)

(b)
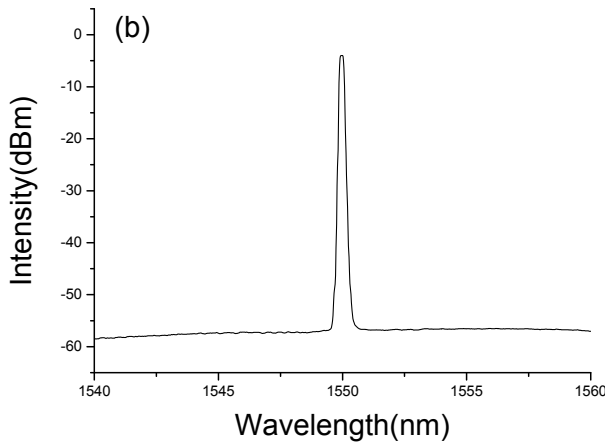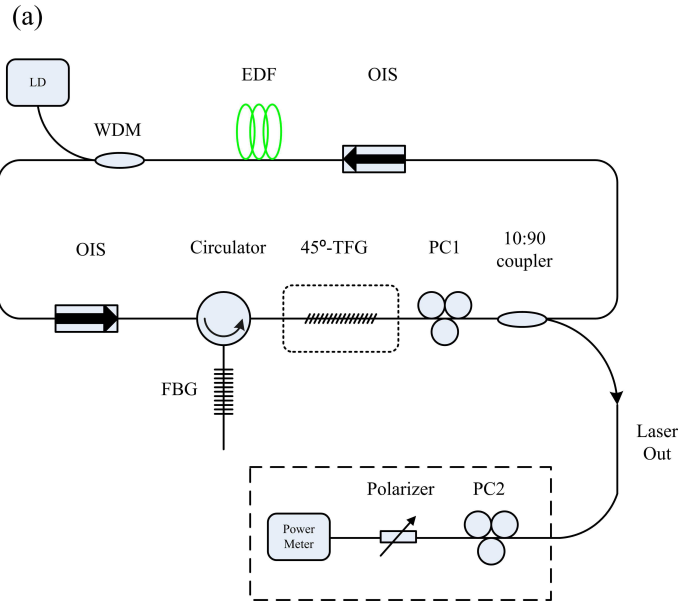
Figure 4.1 (a) Schematic diagram of the fibre ring laser structure. The polarisation extinction ratio of the laser output is measured using the setup shown in dashed line box. (b) Typical output spectrum of the fibre laser.

The DOP measurement of the output of the fibre laser is conducted by the setup shown in the dashed line box in Figure 4.1(a) and the DOP calculation is simply based on the following expression:

Equation 4.1 Degree of Polarisation (DOP)$= \dfrac{P_{polarised}}{P_{polarised} + P_{unpolarised}} \times 100\%$

Where $P_{polarised}$ is the polarised part of the laser power, $P_{unpolarised}$ is the unpolarised part of the laser power. Similar to the PDL measurement described in Chapter 3, adjusting polarisation controller (PC2) in Figure 4.1(a) can give the maximum power $P_{max} = P_{polarised} + \dfrac{1}{2} \cdot P_{unpolarised}$ and minimum $P_{min} = \dfrac{1}{2} \cdot P_{unpolarised}$ of the fibre ring laser. The DOP can therefore be calculated by applying Equation 4.1. Without 45°-TFG in the laser cavity, the fibre ring laser produced the output with DOP only about ~ 22.6 %. This indicates that the laser output is almost un-polarised. When incorporating the 45°-TFG into the cavity, the laser output shows DOP of ~99.6% for TFG1 and ~99.9 % for TFG2, which clearly manifests that the output of the laser is highly polarised and almost single polarisation. In comparison with ~22.6% without intra-cavity 45°-TFG, this is a remarkable improvement and it is more interesting to note that by introducing a relatively weak 45°-TFG (like TFG1) into the cavity, a high PER state can also be achieved.

4.2.1.2 Slope efficiency and stability performance

The slope efficiency of the fibre laser has also been examined before and after inserting the stronger 45°-TFG (TFG2). The power meter employed to perform the measurement has a quoted resolution of 0.2 μW with a 5% measurement uncertainty which is regarded as the main error factor for the output power measurement. It can be seen clearly from Figure 4.2 that the threshold pumping power for the laser with and without TFG2 is similar which is ~8 mW. However, the slope efficiency decreased from 13.2 % to 7.9 % after the 45º-TFG had been incorporated. We believe this could be due to the 45º-TFG induced PDL related total loss in the laser cavity, mainly from the two splices.
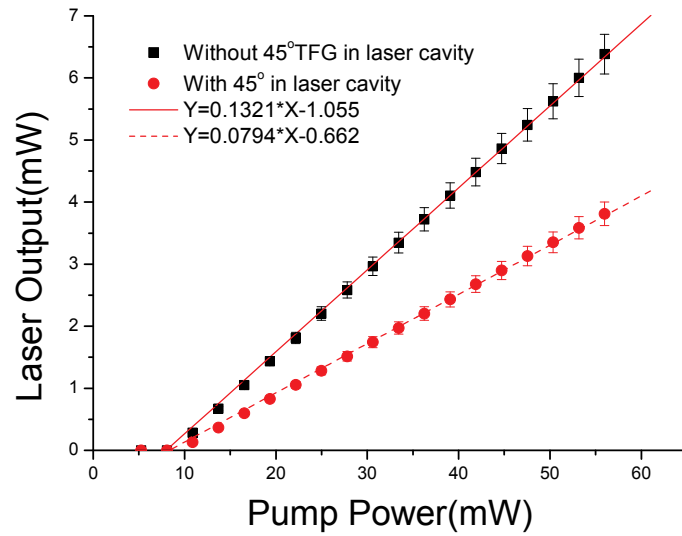
Figure 4.2 Slope efficiency of the fibre ring laser before (■) and after (●) inserting the intra-cavity 45º-TFG.

The polarisation stability of the fibre ring laser with the 45°-TFG in the cavity has also been investigated. The DOP were measured over 5 hours at the laboratory condition and the results are plotted in Figure 4.3. Apart from the systematic error from the power meter, the environmental effect may also play important role in the polarisation stability of the laser. Here, we indicate DOP errors by standard deviation of the measurement. The uncertainty in timing is estimated to be ±1 min. It can be seen that over 5 hours the DOP variation is within ~0.2 %, which is insignificant for most systems. We should stress that this stability could be improved if the ambient environmental variation could be properly controlled.
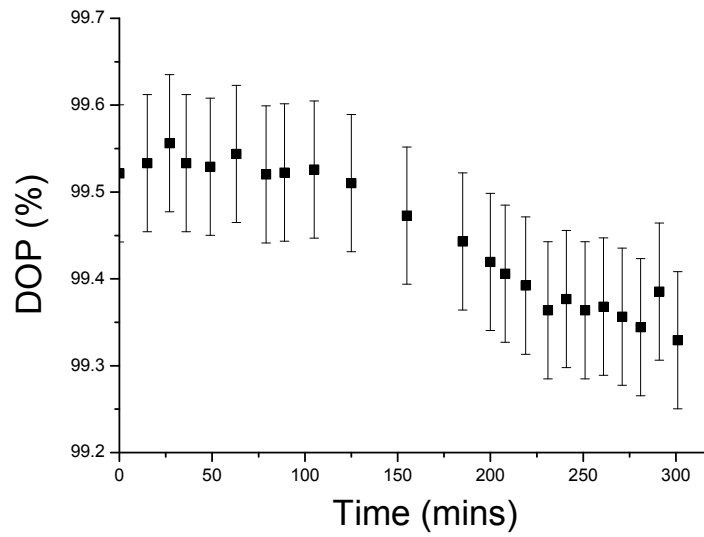
Figure 4.3 DOP stability measurement over 5 hours at the laboratory condition.

4.2.1.3 Tuning ability

As an FBG was used as a wavelength seeding element, this laser has a capability of continuous wavelength tuning. We have inspected the tunability by applying mechanical strain to the seeding FBG. Figure 4.4 shows the outputs when the FBG is under strains. From Figure 4.4 we can see the laser output has been tuned over ~1 nm range by applying strain up to ~1000 $\mu\varepsilon$, and even larger range up to 40 nm may be achieved if the FBG has a preserved mechanical strain [173].
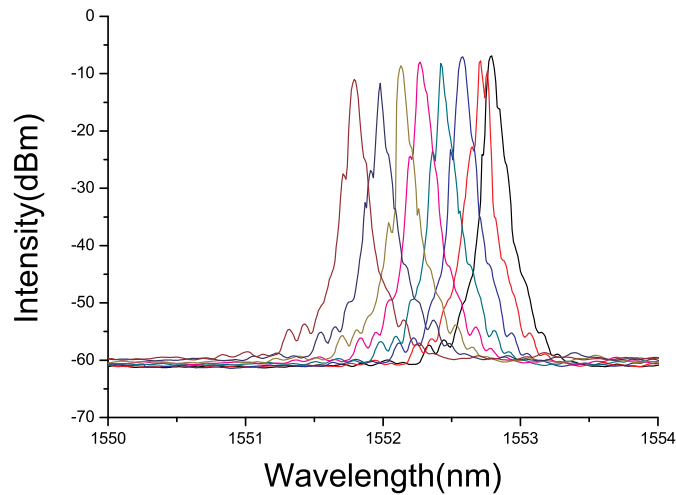
Figure 4.4 Output wavelength tuning through stretching the seeding FBG.

4.2.1.4 Single polarisation, single wavelength fibre ring laser using 2nd-order Bragg resonance of 45º-TFG

In Chapter 3, it is mentioned that the 2nd-order Bragg resonance (SBR) generated by the 45º-TFG exists. This SBR has shown both large PDL and narrowband reflection. Consequently, it can serve as a polarising grating which may produce polarised output in laser cavity. More importantly, this polarising grating is based on standard low-birefringence fibres.
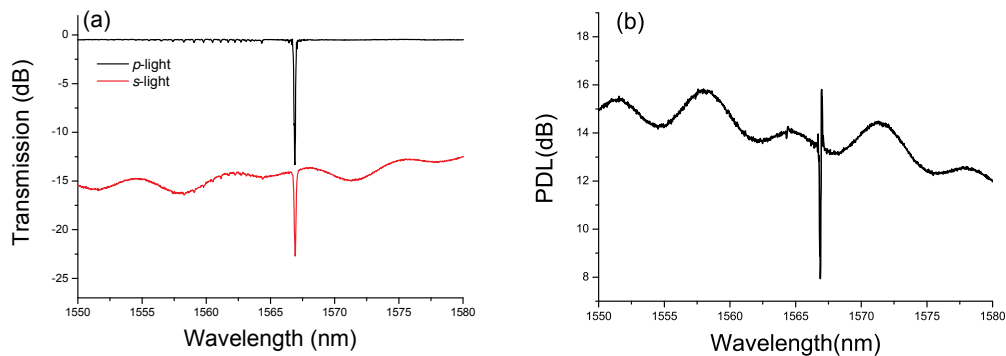
Figure 4.5 (a) Measured transmission spectrum of the 45°-TFG for both *p*-light and *s*-light showing SBR at 1566.9 nm ;(b) measured PDL spectrum of the 45°-TFG

A typical optical spectrum of the 45°-TFG with SBR is shown in Figure 4.5(a). It shows a general insertion loss of ~ 0.4 dB for *p*-light while ~ 15 dB for *s*-light. Both *p*-light and *s*-light have a SBR reflection band centred at ~1566.90 nm and ~ 1566.92 nm respectively with a similar 3 dB bandwidth of ~ 0.1 nm. The difference in SBR central wavelength is mainly due to the polarisation mode dispersion of the SBR. The strength of SBR for *p*-light is ~ 12 dB. Therefore a narrow bandwidth *p*-light polarising grating has been demonstrated. Figure 4.5(b) illustrates the measured PDL spectrum of the 45°-TFG, the large spike in the middle of the figure indicates the existence of SBR. The large spike comes from the polarisation mode dispersion of the SBR. In order to evaluate the polarising function of the 45°-TFG induced SBR, a standard fibre ring laser was constructed as shown in Figure 4.6(a) which is similar to Figure 4.1(a). Compare to Figure 4.1(a), both the FBG and 45°-TFG have been replaced by a single 45°-TFG with SBR response which can provide polarisation feedback to the laser cavity through an optical circulator. In order to evaluate the DOP of the laser, the output was measured through an OSA with a polariser and a polarisation controller, as shown in dotted box in Figure 4.6(a).
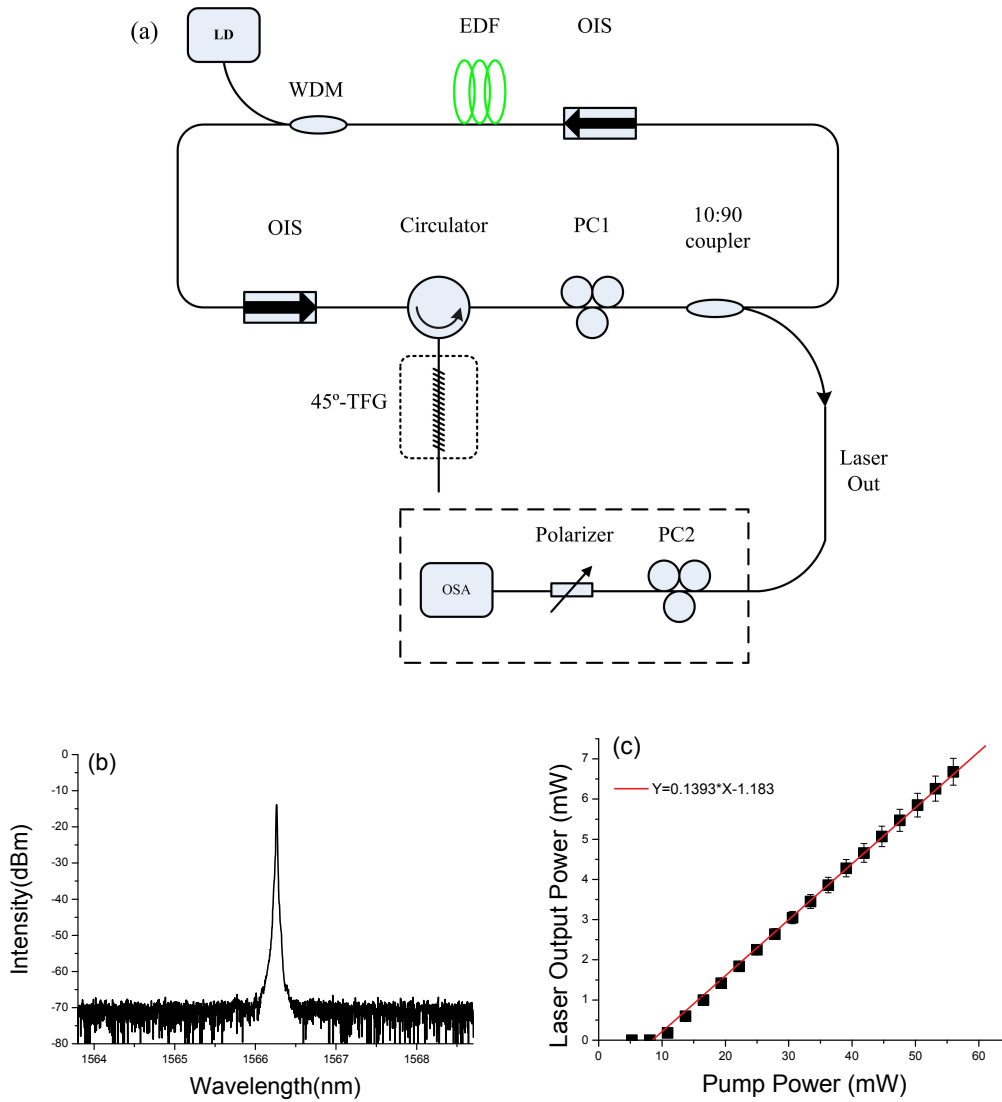
Figure 4.6 (a) Schematic of the proposed fibre laser configuration; (b) typical emission spectrum of the fibre laser; (c) slope efficiency of the fibre laser.

Figure 4.6(b) gives a typical laser output optical spectrum displayed on the OSA showing lasing wavelength at 1566.9 nm which is defined by the central wavelength of the SBR. The DOP of the fibre laser was measured as high as ~99.8%, clearly indicating single polarisation oscillation of the fibre laser. Furthermore, as indicated in Figure 4.6(c), the laser exhibited a comparable slope efficiency of ~13.9 % to the system where a standard FBG was used for seeding (refer to section 4.2.1.2). Figure 4.7(a) demonstrates the laser output amplitude variation monitored over 60 mins. The amplitude variation is measured to be only ~0.2 dB at the laboratory conditions, while Figure 4.7(b) depicts the laser tuning ability by applying mechanical strain on the 45°-TFG. Here, ~1 nm tuning range has been demonstrated successfully.
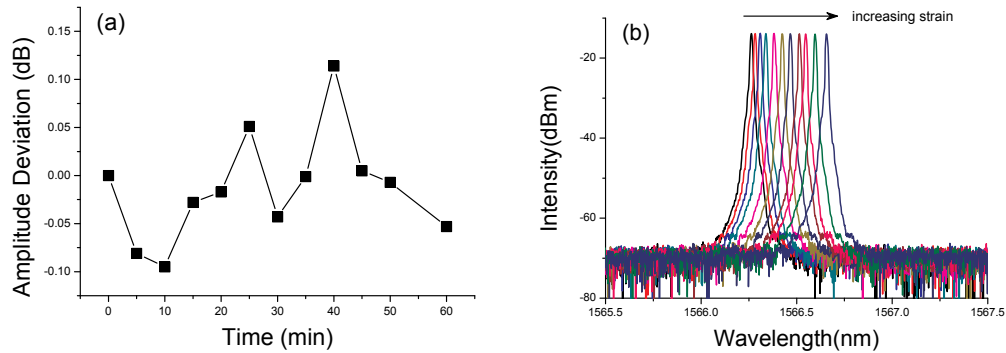
Figure 4.7 (a) laser output amplitude variation monitored over 60 mins; (b) laser wavelength tuning by applying strain to the SBR.

4.2.2 TFG based multi-wavelength switchable fibre lasers

Optical fibre lasers with switchable multi-wavelength output are useful in many applications, such as WDM optical fibre communication systems, fibre sensors, optical instrument and system diagnostics and so on. FBGs are ideal wavelength selective components for fibre lasers due to their advantages of intrinsic fibre compatibility, ease of use, and low cost etc. EDF has been developed and widely used for commercial fibre lasers and amplifiers owing to its high optical gain and low noise figure in 1550 nm region. Because of its relatively broad homogeneous excitation, it is normally difficult to obtain stable oscillations with relatively close wavelength spacing in EDFLs at room temperature. Various techniques have been developed to suppress the mode competition induced by the homogeneous broadening of EDF, such as cooling down EDF in liquid nitrogen [174], incorporating a frequency shifter in the cavity [175], employing a hybrid gain medium [176] and utilizing spatial hole burning by inserting a multi-phase shift FBG in a linear cavity fibre laser [177]. Special laser cavity configurations for multi-wavelength operation by incorporating a segment of highly nonlinear photonic crystal fibre or dispersion-shifted fibre have also been reported [178-180]. In recent years, multi-wavelength fibre lasers operating at room temperature by utilising polarisation hole burning (PHB) effect from FBGs made in PM fibres have been studied extensively and various setups have been demonstrated [181-183]. Nevertheless, in all these setups, the PHB effect has only been studied with PM fibre based devices. In this section, single- and multi-wavelength switchable fibre lasers implemented fabricated utilising both 45°- and ex 45°-TFG in an EDF ring laser

cavity without any PM fibre based device have been investigated. In this combination, the 45°-TFG is used as an in-fibre polariser [13] and the ex-45º structure as a polarisation dependent loss filter. Firstly, a single polarisation, switchable, dual-wavelength EDFL has been exploited. In this configuration, the separation between the switchable wavelengths can be more flexibly designed with potential tuning capability. Then, the extended version, a single polarisation, wavelength switchable, quadruple wavelength EDFL has been demonstrated.

4.2.2.1 TFG based dual wavelength switchable, single polarisation EDFL

UV-inscribed 45°-TFG and 77°-TFG were chosen to be incorporated into the ring EDFL to achieve dual wavelength switchable and single polarisation output. According to our study, TFGs with ex 45º tilted structures exhibit PDL properties, as they show paired polarisation loss peaks in the 1550 nm region [15]. In order to locate the paired polarisation loss peaks in the EDF gain spectrum, we choose a 77°-TFG, which was fabricated by rotating the amplitude mask by 73° in the UV-inscription system. The transmission spectrum of this 77°-TFG was first examined using a broadband source (Agilent 83437A) and an OSA, which is shown in Figure 4.8(a). From the figure we can see that all paired loss peaks exhibit near 3 dB strength, indicating the light is coupled almost equally to the two sets of cladding modes with orthogonal polarisation states. We also measured the 77°-TFG using polarised light from a broadband light source (AFC BBS 1550A-TS) with a low degree of polarisation while inserting a commercial in-fibre polariser and a polarisation controller between the light source and the 77°-TFG. As the zoomed spectra of one pair of peaks in Figure 4.8(b) shows, when the fast-axis mode is fully excited by the polarised light to ~12 dB, the slow-axis mode almost disappeared, and when the slow-axis mode is fully excited to ~10 dB, the fast-axis mode almost disappeared. Equal power distribution occurs between the fast- and slow-axis modes when the probe light is un-polarised. This proves that although the 77°-TFG was made in standard telecom fibre, the excessively tilted structure makes it behaving as a PM-like device, i.e. a PDL filter.
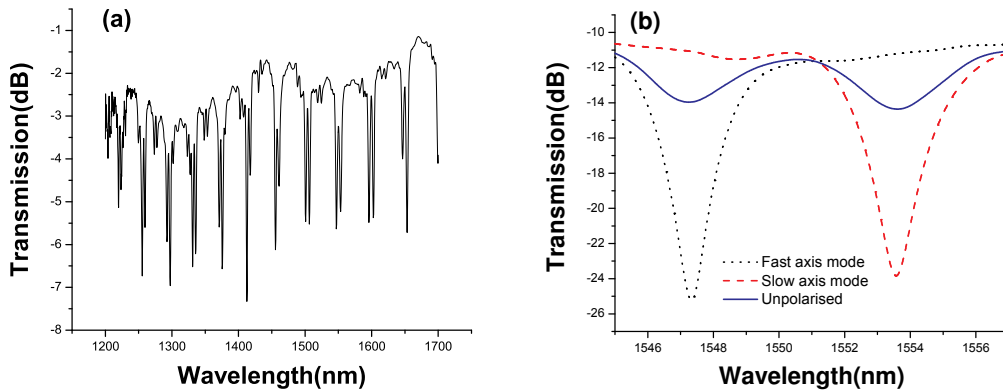
Figure 4.8 (a) Transmission spectrum of the 77°-TFG over wavelength range 1200 nm –
1700 nm; (b) Zoomed spectra of one pair of polarisation loss peaks of the 77°-TFG
around 1550 nm measured with un-polarised (blue solid line) and fully polarised light
(black dotted line for fast-axis mode, red dashed line for slow-axis mode).

The 45°-TFG used as an in-fibre polariser in the EDFL system was fabricated
previously using the concatenation method, employing a normal phase mask with 1.8
µm period (from QPS), which was detailed described in Chapter 3. In addition to the
two TFGs, two standard FBGs (G1 and G2) were used as seeding wavelength
selectors, which were UV-inscribed in H_2-loaded SMF-28 fibre with their Bragg
wavelengths matching the two loss peaks of the 77°-TFG. Their spectra are shown in
Figure 4.9.
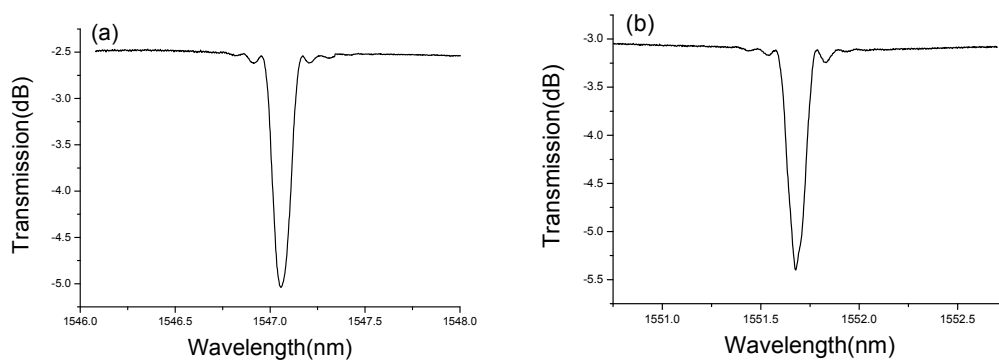
Figure 4.9 Measured transmission spectra of the seeding FBGs: (a) G1 at 1547.07 nm; (b)
G2 at 1551.65 nm.

It is shown in Figure 4.9 that the reflectivities of the two FBGs are ~2.51 dB and ~2.28 dB at 1547.07 nm and 1551.65 nm, respectively, and the bandwidths are ~0.1 nm for both G1 and G2. G2 was not quite matching with the slow-axis loss peak of the 77°-TFG, so was mechanically stretched to 1553.24 nm in the experiment.

4.2.2.2 Principles of the EDFL system and experimental results

The set-up for the proposed dual-wavelength switchable EDFL is shown in Figure 4.10. In this configuration, the gain medium is a ~6 m of highly Erbium doped fibre (from Lucent Technology), which has an absorption coefficient of 12 dB/m. A 976 nm laser diode (from SDL) controlled by a commercial laser diode driver (Newport 505B) and temperature controller (Newport 300 Series) is used to pump the EDFL through a 980/1550 WDM coupler. An OIS ensures an anticlockwise ring cavity. The 30 % arm of the coupler is used as the output port of the laser. A fibre PC is placed between the 77°-TFG and the 45°-TFG. Two standard FBGs (G1 and G2) functioning as seeding wavelength selectors are coupled into the laser cavity via a circulator. The end of the FBG array is terminated by index matching gel in order to eliminate any unwanted background amplified spontaneous emission (ASE) noise.

The operation principle of this dual-wavelength switchable EDFL is described as follows. The intra-cavity 45°-TFG has a very high PER, which can guarantee that the fibre ring laser will oscillate in single polarisation regime. The 77°-TFG will induce PDL to the ring cavity around its paired loss peaks' region, thus imposing PHB effect to the gain medium in this region. The amplitude of the loss depends on the polarisation state of the light travelling in the 77°-TFG.
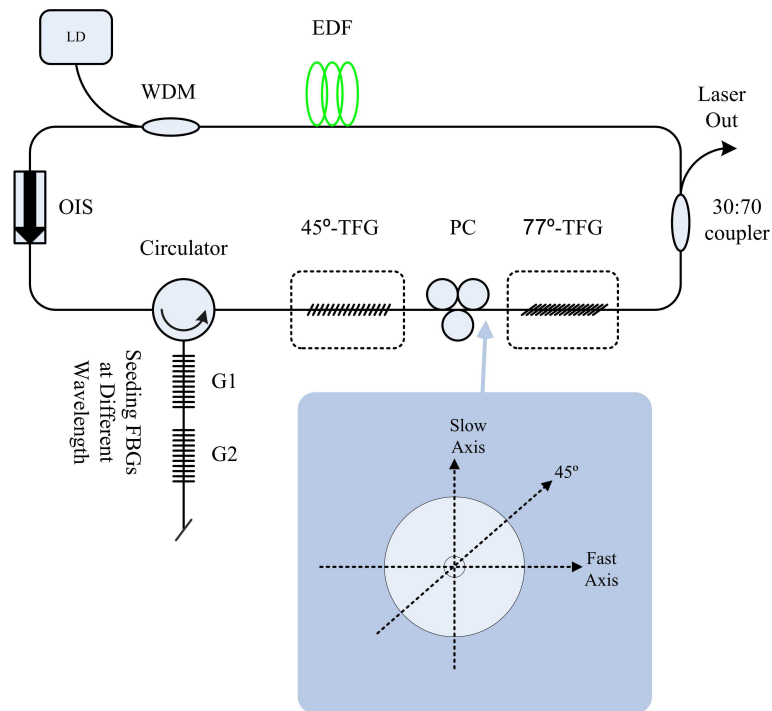
Figure 4.10 Schematic diagram of TFG based single- and dual-wavelength switchable EDFL. The inset describes the polarisation directions of the light launching to the 77°-TFG

By adjusting the PC to control the polarisation state of the light entering the 77°-TFG, i.e. polarised in the equivalent fast- or slow-axis of the 77°-TFG, single-polarisation and single-wavelength lasing at either 1547 nm or 1553 nm can be realised. Figure 4.11(a) and Figure 4.11(b) show the single wavelength oscillation of the fibre ring laser at the two seeding wavelengths, respectively.
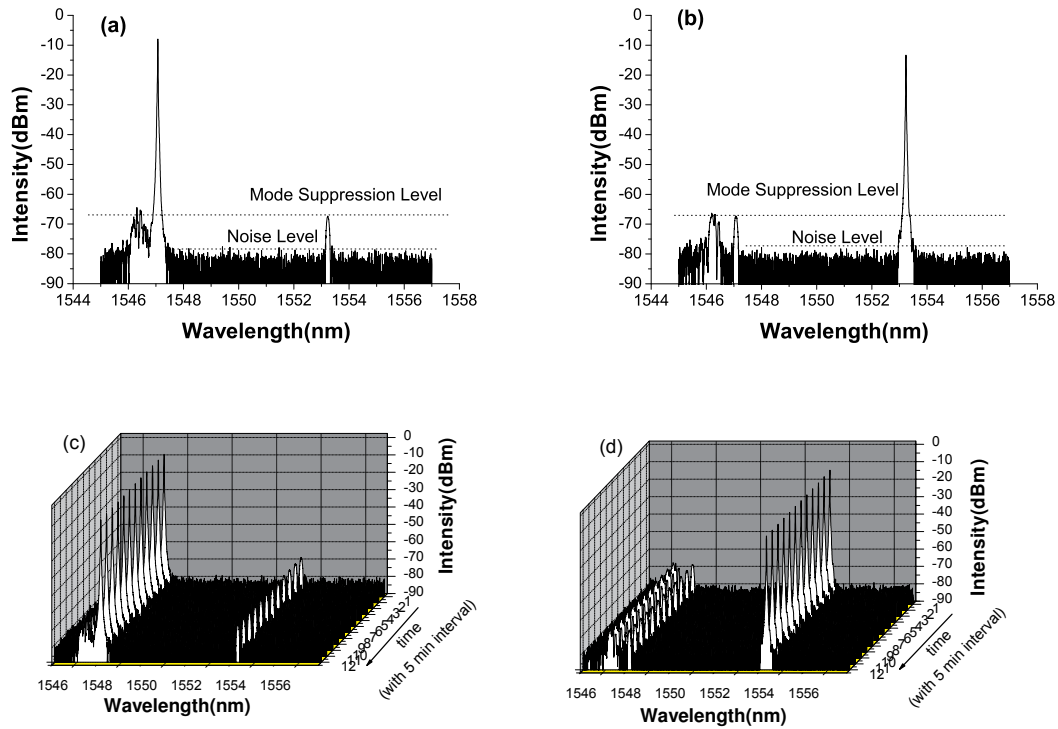
Figure 4.11 Single wavelength lasing oscillation of the propose fibre ring laser at two seeding wavelengths at (a) 1547.07 nm and (b) 1553.24 nm; (c) and (d) stability measurement of the two laser lines.

The spectra were recorded every 5 min to examine the stability of the laser. The recorded spectra are plotted in Figure 4.11(c) and Figure 4.11(d) and show the laser output amplitude variation is less than 0.5 dB within 1 hour at the laboratory condition. From Figure 4.11 we can see that the side mode suppression ratio (SMSR) is larger than 50 dB for both laser lines. This value is higher than that of the EDFLs reported in references [181-183]. The higher SMSR of the TFG based system may be attributed to the ASE suppression function of the 45°-TFG and the low reflectivities of the two seeding FBGs.

The measured DOP of the laser output was ~99.9 % for 1547.07 nm and ~99.8 % for 1553.24 nm laser lines, indicating a high degree of single polarisation operation. If we change the polarisation direction of the launching light to 45° between the fast- and slow-axis of the 77°-TFG, as shown in inset in Figure 4.10, dual-wavelength laser output with two orthogonal polarisation states can be achieved. Figure 4.12 shows the dual-wavelength output at ~1547.07 nm and ~1553.24 nm of the fibre ring laser. The

dual wavelength operation has been continuously monitored for 20 mins and no noticeable amplitude variation was observed for a fixed PC position at room temperature (shown in Figure 4.12(b)).
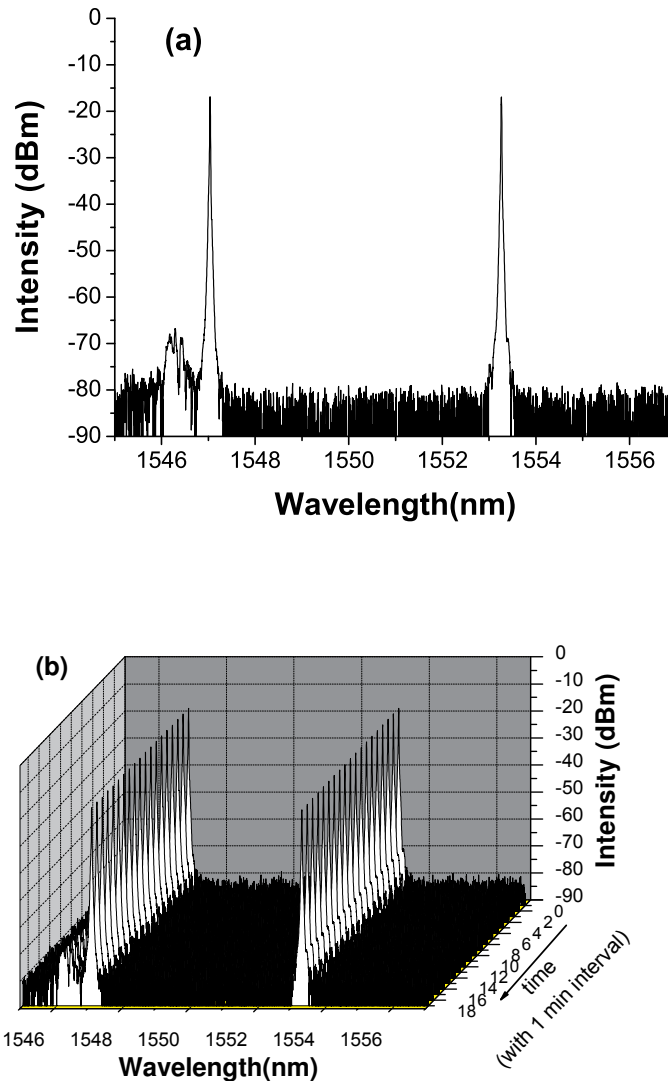
Figure 4.12 (a) Dual wavelength lasing oscillation of the proposed fibre ring laser; (b) Stability of dual wavelength oscillation (20 times repeated scan).

The slope efficiencies of the proposed fibre laser have also been characterised for both single- and dual-wavelength operation. Figure 4.13(a) shows that for single wavelength operation, the threshold pump power is just slightly lower than ~15 mW and the slope efficiencies are 0.22% and 0.12% for 1547.07 nm and 1553.24 nm lasing lines, respectively. The difference in slope efficiency could be due to the variation of the polarisation dependent gain of the EDF. While the laser working in

dual-wavelength operation, equal power distribution at ~1547 nm and ~1553 nm regions can be obtained by carefully tuning the PC. As shown in Figure 4.13(b), for dual-wavelength operation, the threshold pump power is just slightly higher than 15 mW and the slope efficiency is ~0.06% which is much lower than that in the single wavelength operation. This is because in dual-wavelength operation, 77°-TFG induces some losses at the two lasing wavelengths, inevitably resulting in lower output for each wavelength. Since there were three extra fibre splices in the cavity and the TFGs may have some small intrinsic loss, it is expected that the slope efficiencies of the proposed EDFL system are to be low. Also, in general, for dual-wavelength operation, the laser stability reduces. The difference from the reflectivity's of the two FBGs which match the loss peaks of the 77°-TFG may also contribute to unstable laser performance. These could lead to larger errors (~ 10 %) compared to single wavelength operation regime. By reducing the loss and employing FBGs with higher reflectivity, the slope efficiency can be improved. However, the trade-off is the SMSR may reduce if the reflectivity of the seeding FBG is too high.
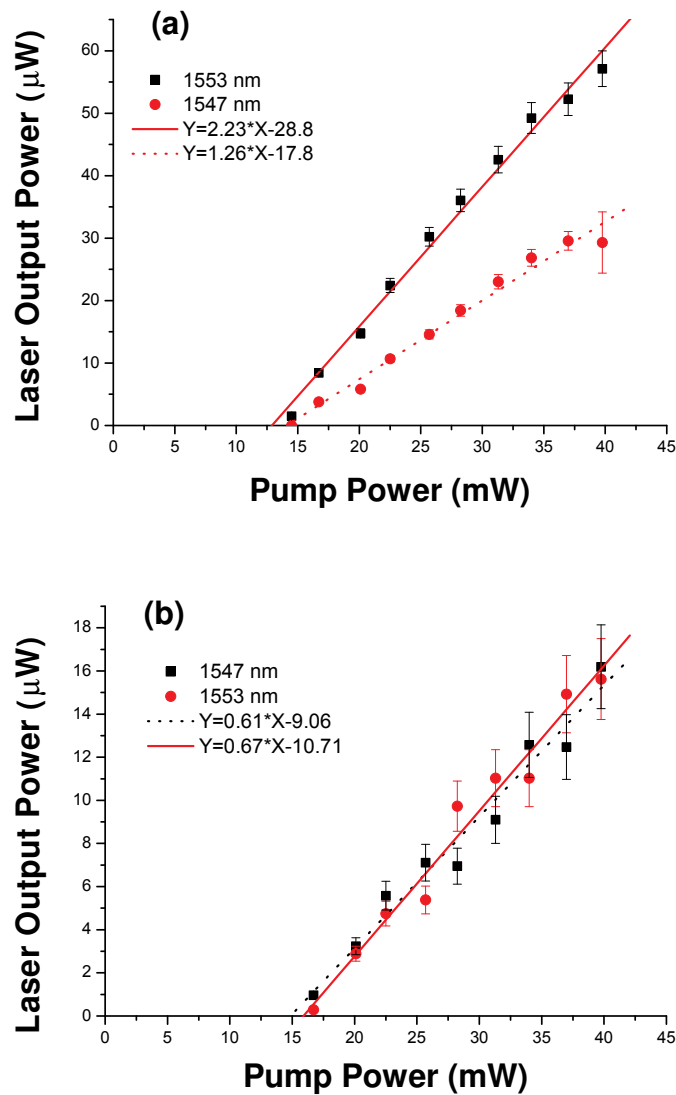
Figure 4.13 Slope efficiencies of the fibre laser at (a) single and (b) dual wavelength output.

One may notice from Figure 4.11 and Figure 4.12, there is a small reflection peak at 1546.5 nm adjacent to the lasing line at 1547.07 nm. This reflection was proved to be induced by the 45°-TFG. We experimentally verified this by monitoring the laser output port when the 77°-TFG and the two seeding FBGs were removed from the cavity. As shown in Figure 4.14, we see a strong reflection around 1546.5 nm when the cavity contained only the 45°-TFG. If the 45°-TFG is a perfect in-fibre polariser no feedback will be provided into the laser cavity, thus only strong ASE should be seen from the laser output port. This proved to be the 2nd-order Bragg reflection of the 45°-TFG as discussed in Chapter 3.
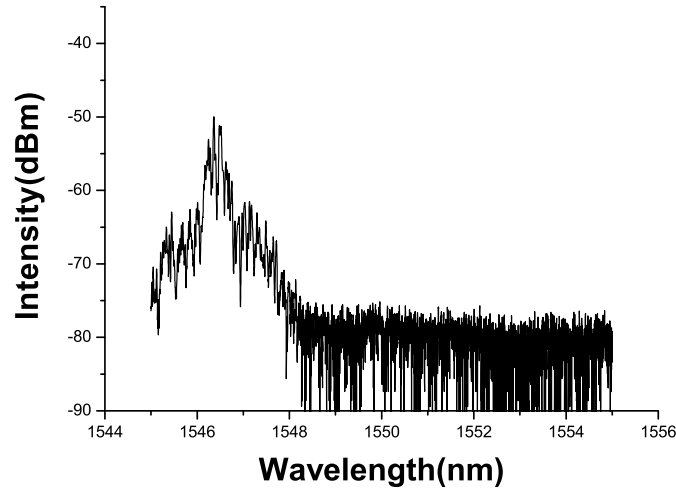
Figure 4.14 45°-TFG induced second order Bragg reflection at 1546.5 nm in the fibre ring

laser.

4.2.2.3 TFG based multi-wavelength switchable, single polarisation EDFL

Following the demonstration of single- and dual-wavelength operation by employing TFGs as intra-cavity polariser and PDL filter, we further investigated switchable multi-wavelength (more than two) output by using two ex-45° TFGs with un-overlapped spectra. Figure 4.15 depicts the expanded version of the fibre laser providing the possibility of quadruple wavelength lasing operation. In order to support quadruple wavelength lasing, we inserted an 81°-TFG into the cavity as the second PDL filter, and also fabricated another two seeding FBGs with wavelengths at 1563 nm and 1569 nm to match the PDL loss peaks of the 81°-TFG. In order to match the loss peaks of the 81°-TFG, the FBGs were designed with low reflectivities around 2.1 dB and 5.6 dB respectively. A second PC was placed before the 81°-TFG for polarisation alteration purpose. The optical spectrum and polarisation properties of the 81°-TFG are shown in Figure 4.16(a) showing the whole spectrum from 1200 nm to 1700 nm with un-polarised probing light and Figure 4.16 (b) showing zoomed one paired peaks probed under polarised light.
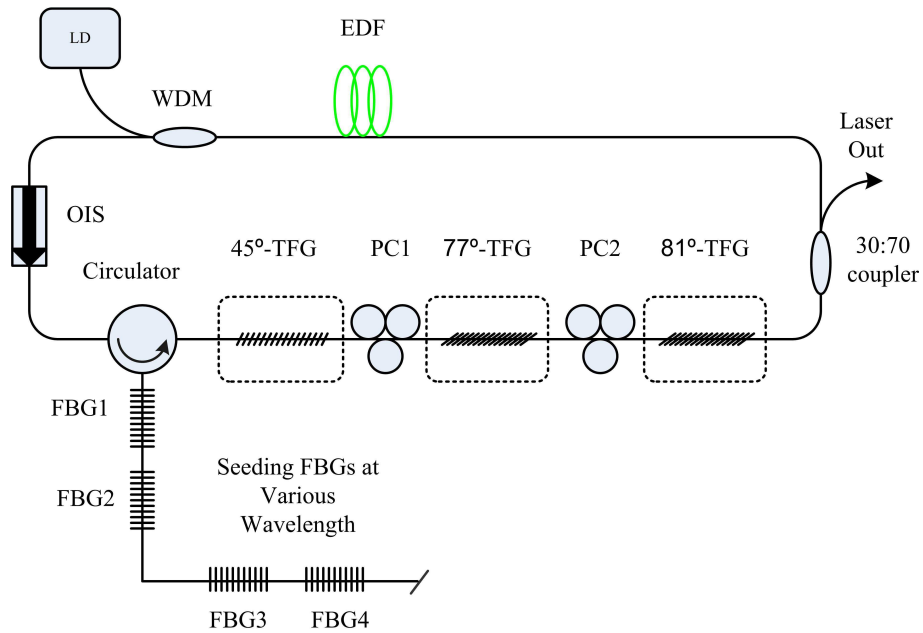
Figure 4.15 Schematic diagram of the proposed EDFL using two ex 45°- and one 45°-TFG which can support switchable quadruple wavelength oscillation.
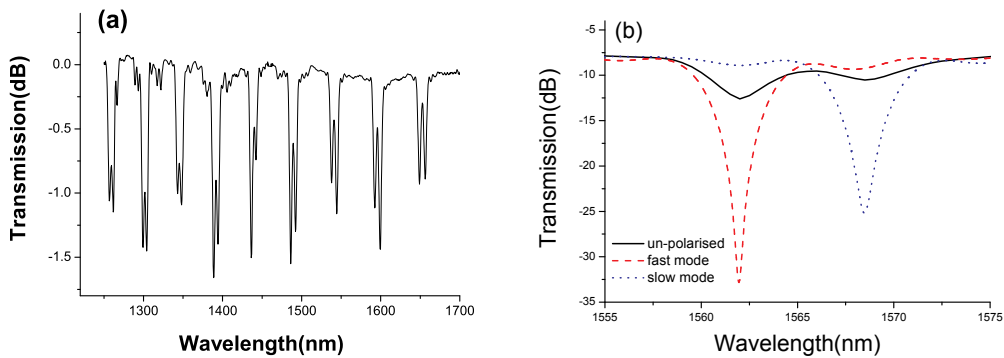
Figure 4.16 (a) Transmission spectrum of the 81° -TFG over wavelength range 1200 nm – 1700 nm; (b) Zoomed spectra of one paired polarisation loss peaks measured with randomly (black solid line) and fully polarised input lights (red dashed lines for fast mode, blue dotted line for slow mode).

By adjusting the two PCs to control the polarisation state of the light entering the 77°-TFG and 81°-TFG (polarised in the equivalent fast- or slow-axis of the ex 45°-TFGs), single-wavelength lasing at any of the four seeding wavelengths has been demonstrated. Figure 4.17 (a)-(d) clearly show the lasing at the four different seeding

wavelengths at 1547.05 nm, 1553.27 nm, 1563.05 nm and 1568.97 nm, respectively. We measured the DOP of the outputs from this fibre laser system by connecting the laser output to a polarisation controller with a commercial polariser and a power-meter. The measured DOP was in the range of ~99.8% to ~99.9% for the lasing oscillation at four different wavelengths, presenting a very high degree of single polarisation operation of the laser system.
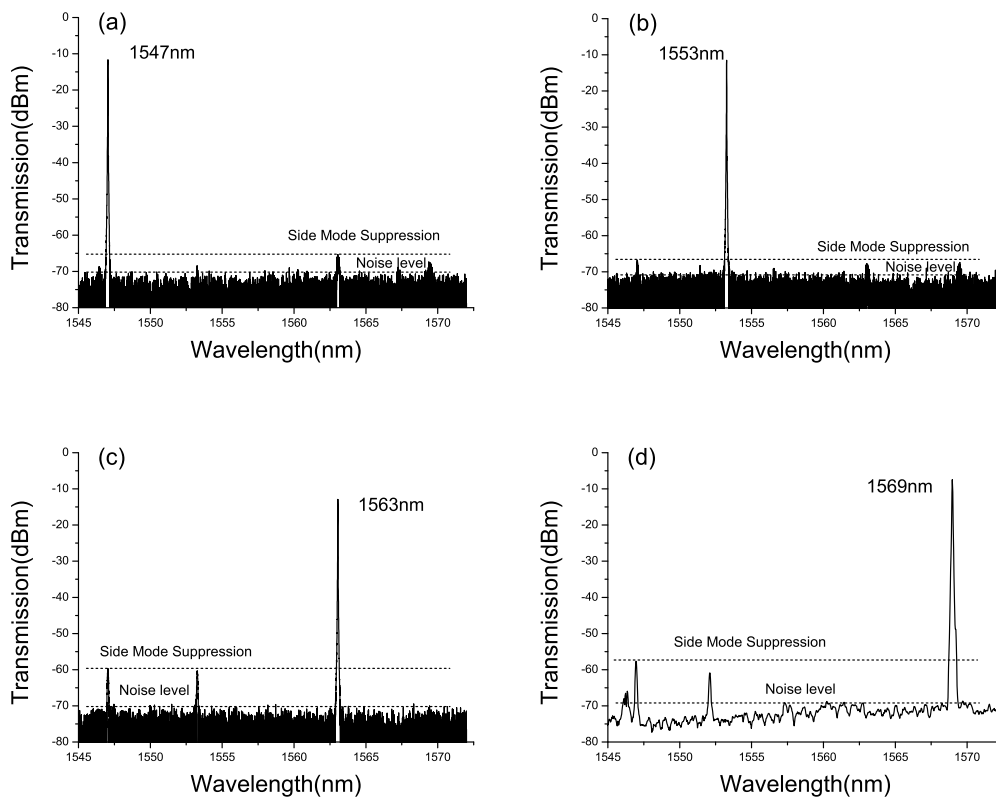
Figure 4.17 Single wavelength lasing at (a) 1547.05 nm, (b) 1553.27 nm, (c) 1563.05 nm and (d) 1568.97 nm.

Again, by adjusting the two PCs to change the polarisation state of the light entering the 77°-TFG and 81°-TFG as this will change the PHB profile, the laser oscillation at double, triple and quadruple wavelengths can be obtained in this system. Figure 4.18(a)-(c) show three sets of dual-wavelength oscillation at 1547.06 nm/1553.27 nm, 1547.06 nm/1563.07 nm and 1553.27 nm/1563.07 nm, respectively. Figure 4.19(a)-(c)

show the three sets of spectra for triple-wavelength oscillation at 1546.94 nm/1551.99 nm/1562.63 nm, 1551.99 nm/1562.63 nm/1568.89 nm, and 1546.94 nm/1551.99 nm/1568.97 nm and Figure 4.19(d) shows the spectrum of quadruple lasing oscillation.
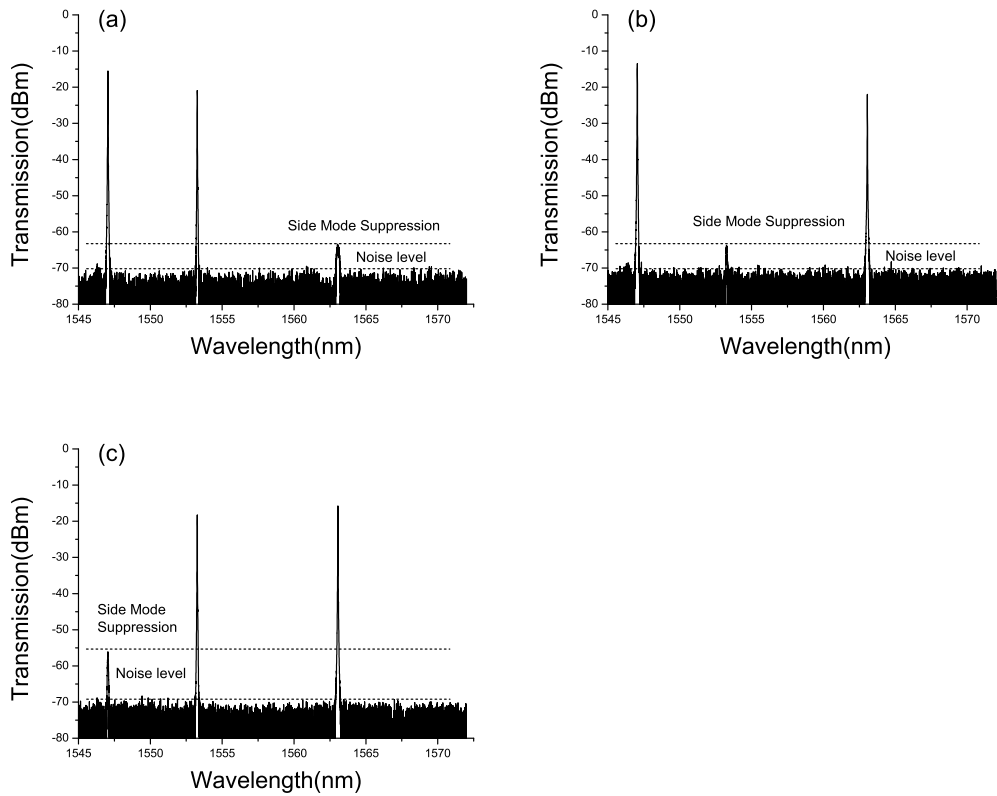
Figure 4.18 Illustration of dual-wavelength lasing at (a) 1547.06 nm/1553.27 nm (b) 1547.06 nm/1563.07 nm and (c) 1553.27 nm/1563.05 nm.
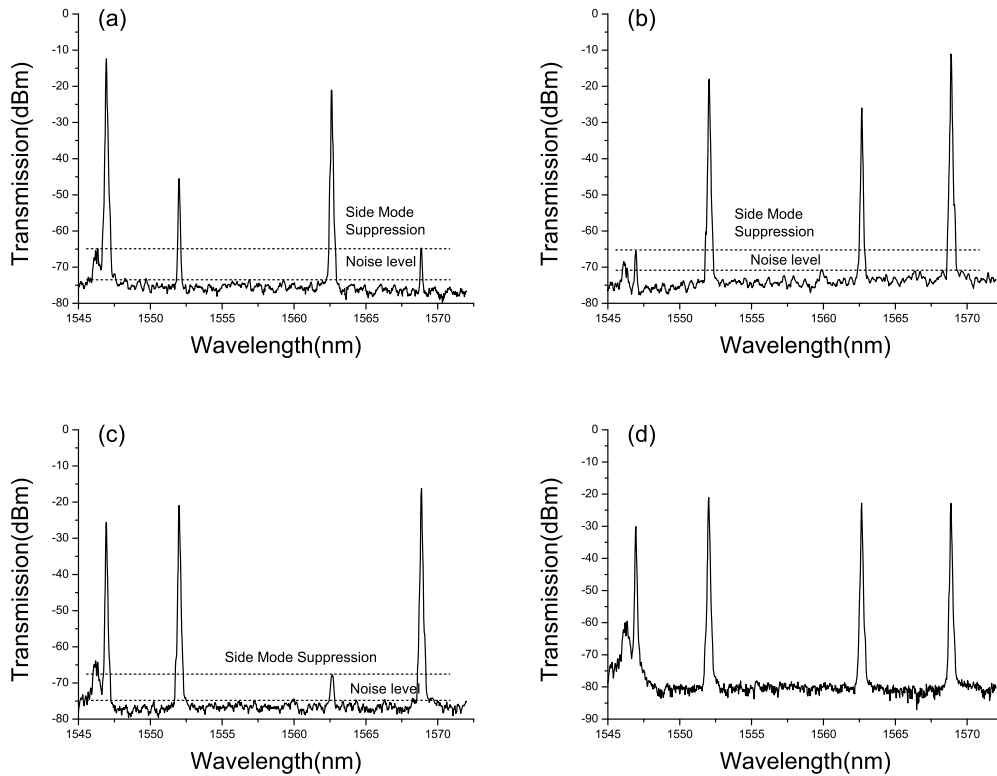
Figure 4.19 Triple wavelength oscillations at (a) 1546.94 nm/1551.99 nm/1562.63 nm
and (b) 1551.99 nm/1562.63 nm/1568.89 nm; (c) 1546.94 nm/1551.99 nm/1568.97 nm;
(d) Quadruple wavelength oscillation for all four wavelengths.

All sets of single- and multi-wavelength lasing oscillation have been continuously monitored for 30 minutes in the laboratory at room temperature for stability assessment. No noticeable amplitude fluctuation was observed for the laser operating at single- and multi-wavelengths when the PCs were fixed at the certain positions during the experiment. Figure 4.20 is an example of the long term monitored lasing profiles on the OSA for 20 mins for (a) single and (b) dual-wavelength lasing situation, showing no obvious change of output amplitude. Similarly, as shown in Figure 4.21(a)-(d), no noticeable change is observed for triple and quadruple wavelength operation.
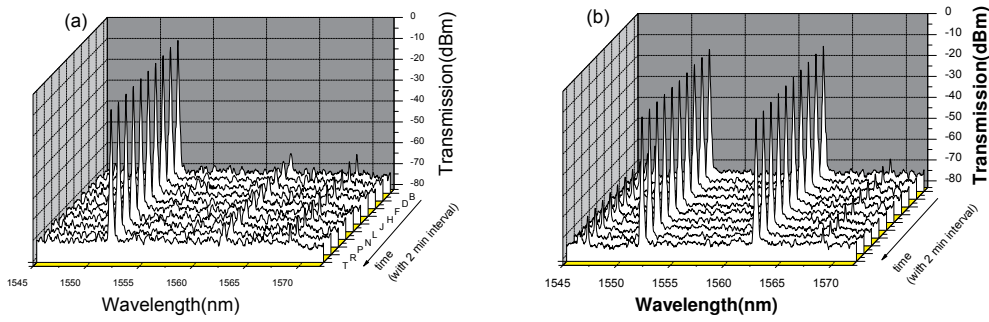
Figure 4.20 Stability measurements for one of the (a) single wavelength, (b) double-wavelength operations, showing no noticeable variation for the output profile.
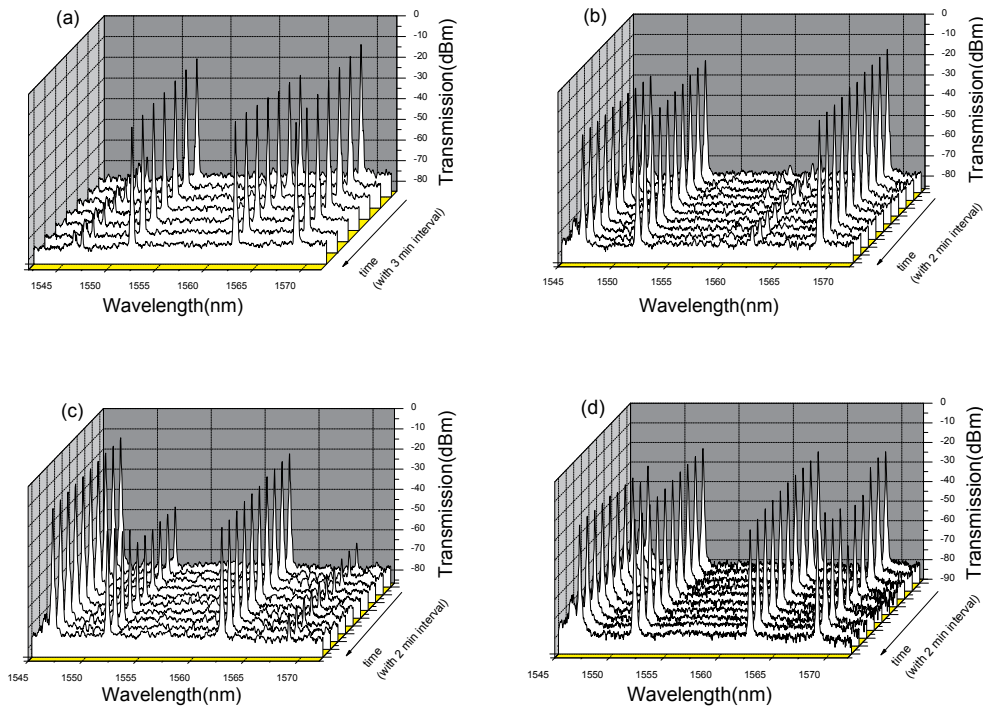
Figure 4.21 Stability description for triple-wavelength (a-c) and quadruple-wavelength (d) oscillation, showing no noticeable variation for the output profiles.

The measure SMSRs for single, dual, triple and quadruple wavelength lasing is 55 dB, 50 dB, 48dB and 40 dB, respectively. The difference in SMSR may result from the variety in strength of the ex 45°-TFGs and the seeding FBGs.

4.3 Pulsed Fibre Laser

4.3.1 Principles of laser mode-locking

A laser can oscillate in a large number of longitudinal modes. In normal operation, the phase relationship among all the modes is random. Especially in the continuous wave resonator case, the beam intensity exhibits random time behaviour. If all the oscillating laser modes are somehow kept with a fixed relation between their phases while having comparable electric field amplitudes, the laser is called mode locked. This is one of the effective ways to get a strong laser pulse output. Any methods that can establish this phase relation is regarded as mode locking. Generally, mode locking can be explained in either frequency- or time-domain [154, 184].

In the frequency domain, consider, for example, there are $2n+1$ longitudinal modes oscillate with identical amplitude E_0. Suppose the phase ϕ_l of the modes is locked following the relation $\phi_l - \phi_{l-1} = \phi$ where ϕ is a constant. Then the electric filed of the output beam can be written as :

Equation 4.2 $E(t) = \sum_{-n}^{+n} {}_l E_0 \cdot \exp\{i \cdot [(\omega_0 + l \cdot \Delta\omega) \cdot t + l\phi]\}$

Where ω_0 is the central mode frequency, $\Delta\omega$ is the modal spacing between two adjacent modes, and the phase for central mode has been set as zero for simplicity. The total electric field of the beam can then be given as:

Equation 4.3 $E(t) = D(t) \cdot \exp(i \cdot \omega_0 \cdot t)$

Where

Equation 4.4 $D(t) = \sum\limits_{-n}^{+n} {}_l E_0 \cdot \exp\{i \cdot l \cdot (\Delta\omega \cdot t + \phi)\}$

The equation above indicates that the total electric field can be described in terms of a carrier wave centred at ω_0, and a time-dependent amplitude $D(t)$. By taking $\Delta\omega \cdot t' = \Delta\omega \cdot t + \phi$, we can rewrite the amplitude such as:

Equation 4.5 $D(t') = \sum\limits_{-n}^{+n} {}_l E_0 \cdot \exp i \cdot l \cdot (\Delta\omega \cdot t') = E_0 \cdot \dfrac{\sin[(2n+1) \cdot \Delta\omega \cdot t'/2]}{\sin(\Delta\omega \cdot t'/2)}$

The equation above shows that $D^2(t')$ is proportional to the beam intensity $E_0{}^2$, thus physically, producing a set of evenly spaced pulse train. This has been clearly depicted in the following picture.
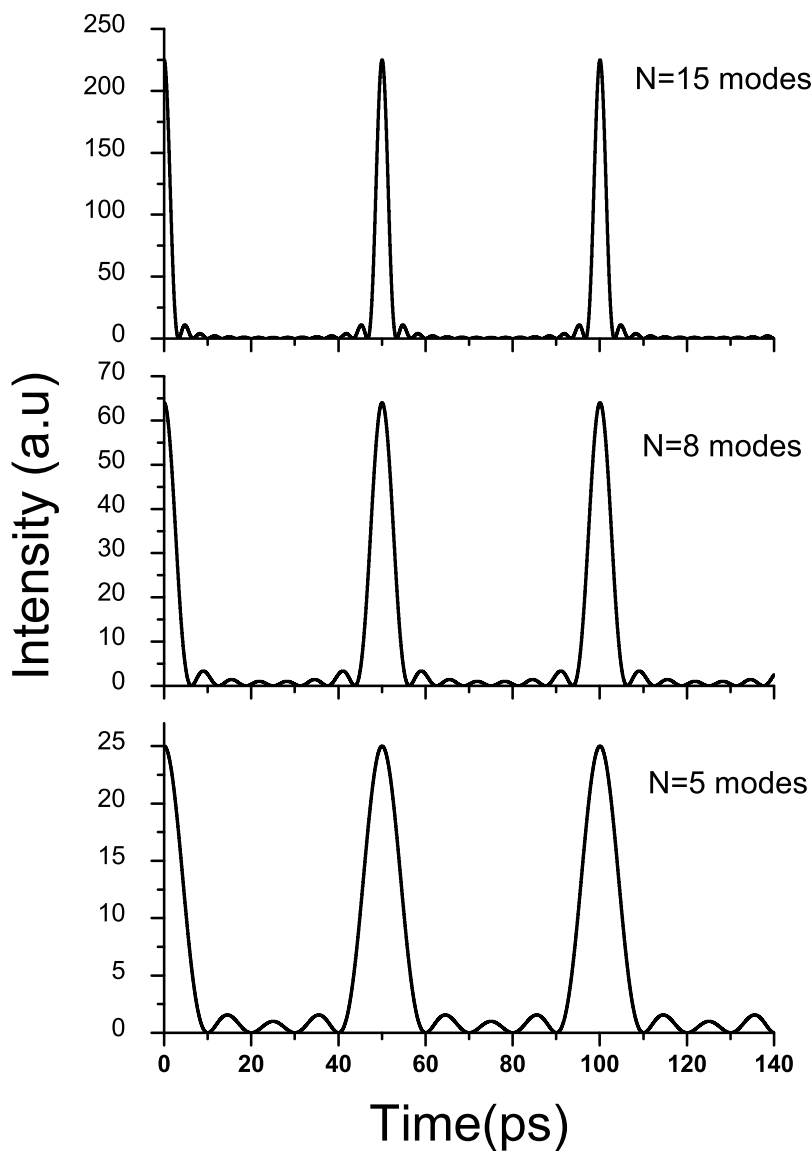
Figure 4.22 simulation of pulse intensities mode locked by N evenly spaced modes for which N=5, 8, and 15.

It can be seen clearly from Figure 4.22 that with a fixed cavity length and gain bandwidth, the pulse duration and pulse intensity can be significantly affected by the number of phase locked modes. The more modes are involved in the locking operation, the shorter pulse can be obtained. In this simulation, for simplicity, only equal amplitude electric fields have been taken into consideration. Consequently, for more modes, the output amplitude is much higher. In real lasers, most of gain medium will have a certain bandwidth profile rather than a flat one, i.e. Gaussian profile,

which could induce amplitude distinction. Nevertheless, as long as the phase is locked, pulse behaviour of laser oscillation can be achieved. To understand mode locking behaviour in time domain, we consider a typical mode locked pulse train shown in Figure 4.23.
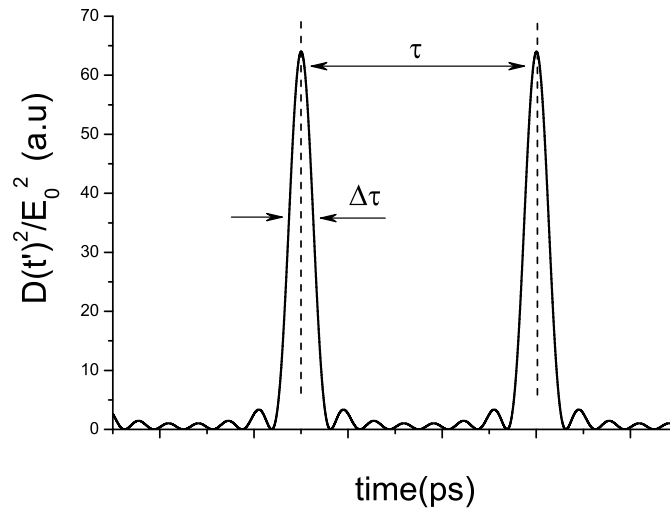
Figure 4.23 A typical output pulse time behaviour description of eight oscillating laser modes with phase locking and equal amplitudes.

In Figure 4.23, τ indicates the pulse separation time representing the cavity round-trip U

Equation 4.6 $\tau = \dfrac{2 \cdot n \cdot L}{c}$

where c is the speed of light in vacuum, n is the effective refractive index of laser cavity, L is the laser cavity length. $\Delta\tau$ is the pulse duration. The mode locking operation can then be visualized as propagating a single pulse with a duration of $\Delta\tau$ which travels around the laser resonator cavity. Due to this description, mode locking could be obtained by integrating a high speed shutter in the laser cavity. Assuming the

shutter operated with a period of τ with an open time of $\Delta\tau$, the shutter could possibly let only the giant pulse pass through. Thus, only this pulse could survive, therefore generating mode-locked pulses.

Basically, any method can behave as a proper shutter would be possible to generate mode locking. Hence, it can have two types of laser mode locking, which are active and passive mode locking. For the former, normally, a phase modulator or an amplitude modulator is involved in mode locking operation. However, extra active components or high frequency electronic devices are always required for this type of mode locking. This further increases the complexity of the laser system. More importantly, the laser in this case is not self-starting.

Passively mode-locked lasers employing an intra-cavity saturable absorber have evolved from fundamental science to commercial instruments, with a wide variety of applications in telecom, optical frequency comb generation, metrology, microscopy and nonlinear science. Femtosecond pulse generation in mode-locked lasers relies on a variety of physical effects including group-velocity dispersion (GVD), self-phase modulation (SPM) and amplification. Further, it is necessary to have some form of intensity discrimination to promote pulse formation from initial white noise. Over the past two decades, a number of different methods have been used including, among others, nonlinear polarisation rotation (NPR) [185-187], nonlinear interferometry [188-189], semi-conductor saturable absorber (SESAM) [190-192] and more recently single-walled carbon nanotubes (CNTs) [193-195].

4.3.2 Mode-locked fibre laser using 45º-TFG

Although solid-state mode-locked lasers remain the current workhorse for high-power, ultra-short pulse generation applications, there has been great interest in mode-locked fibre lasers due to the practical advantages they offer, such as superior wave-guide properties, reduced thermal effects, power scalability, and integrability with other telecom components. In general, a mode-locked fibre laser that is made from all-fibre components would be desirable. However, current fibre lasers rely on bulk optics in the laser cavity thus reducing the benefits of an all-fibre format. For instance, a common method to experimentally achieve intensity discrimination in a mode-locked fibre laser is through NPR. The basic principle of NPR is described below in Figure

4.24 [187, 196]. The light passing through a linear polariser can be transformed to elliptical polarisation by means of a set of wave plates or a polarisation controller. This polarisation ellipse can rotate from angle α to an angle β with respect to the fibre axis as shown in the diagram due to the Kerr effect induced by the fibre from which the polarisation ellipse will only rotate an angle while maintaining the ellipicity. If the second set of wave plates was at some position that can recover the elliptical polarisation state into linear which can match the analyser axis, then there is no loss for the transmission light. Because the optical Kerr effect induced change in polarisation ellipse is dependent on the intensity of the pulse, the light transmission through the analyser is intensity dependent. By appropriately selecting the polarisation ellipse through polarisation controllers, one can discriminate the pulse energy by maximizing the transmission for the highest pulse intensity and blocking propagation of lower energy pulses, thus creating an intensity discriminator i.e. a saturable absorber. Therefore, a self-started mode locked fibre laser could be obtained.
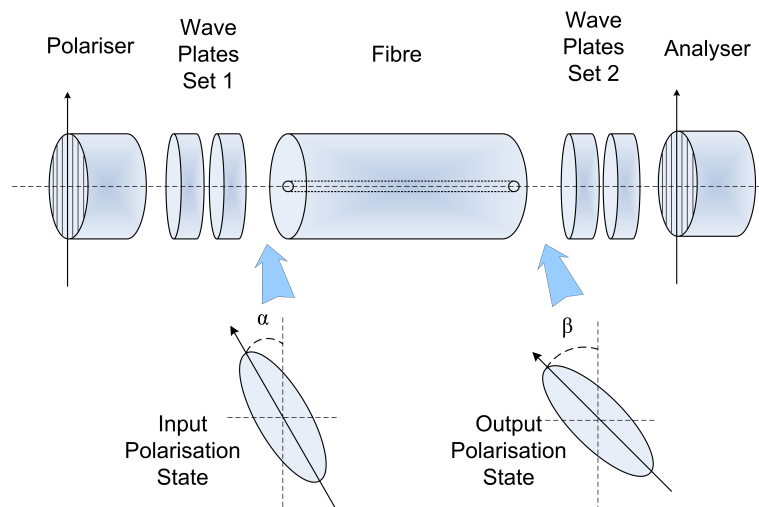
Figure 4.24 Schematic diagram of NPR effect in an optical fibre based system.

Usually, a bulk optic polariser is used in this configuration, resulting in high cavity loss due to the coupling between fibre and bulk segments. Compared with bulk optic polarisers, in-fibre polarisers are more desirable in fibre systems due to their light weight, low insertion loss, and high coupling efficiency. Several types of in-fibre polariser have been demonstrated [169, 172], however they lack the robustness and integrity necessary to take full advantage of an all-fibre device. Recently 45º-TFGs

have been shown to exhibit strong PDL property, as the light through the grating shows small transmission loss for the *p*-light whereas the *s*-light loss remains significant. This polarisation discrimination mechanism enabled the 45°-TFGs being used as a PDL equaliser [11] and a broadband polariser [13] in optical communication systems. Furthermore, these polarising gratings have been successfully used to generate single polarisation continuous output in an all-fibre laser structure [197].

In this section, we focus on pulsed light generation and present a novel all-fibre mode-locked laser that is passively mode-locked using NPR and a 45º-TFG polarisation element.

4.3.3 Mode-locked fibre laser configuration and experimental results

The 45º-TFG used in the experiment was fabricated as described in Chapter 3.
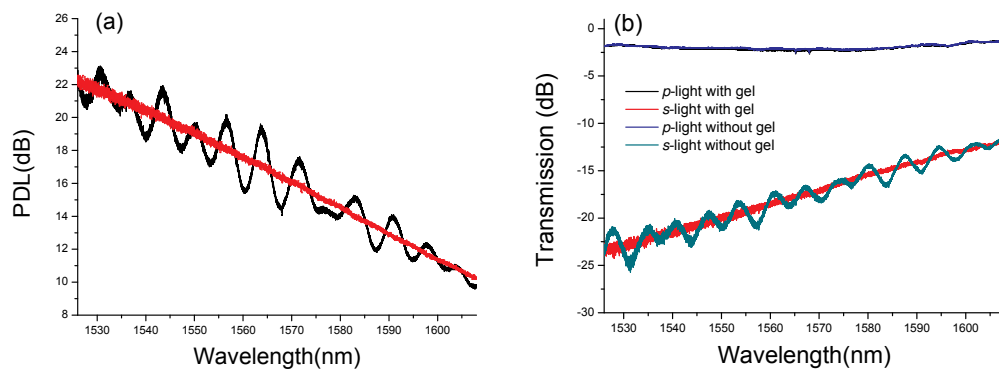
Figure 4.25 Measured (a) PDL response (b) transmission of the 45º-TFG used for mode locking from 1525 nm to 1608 nm. Note, the oscillating and smooth curves were obtained when the 45°-TFG were surrounded by air and index gel (RI=1.456).

Figure 4.25 shows the characteristic PDL and transmission profile of the 45°-TFG used for the mode locking experiment over a large wavelength range (~80 nm) that almost covers a typical gain bandwidth of EDF. As shown in figure (a), the PDL is ~ 22 dB at 1550 nm and drops to ~10 dB at 1600nm. Figure 4.25(b) indicates there is an average ~1.5 dB insertion loss across the entire spectrum for *p*-light while transmission loss is much higher for *s*-light, which mainly from PDL effect.

The mode locking laser experimental set-up is shown in Figure 4.26. The laser consists of ~6 m conventional EDF (from Lucent Technologies) with nominal absorption coefficient of 12 dB/m at 1530 nm and normal dispersion -8.6 ps/nm/km. The length of the passive fibre segment is ~12 m and the length of the fibre incorporating the 45°-TFG is ~50 cm. The 45°-TFG was made in B/Ge co-doped photosensitive fibre, which has anomalous dispersion of ~10 ps/nm/km, thus giving a net-anomalous dispersion of the laser cavity ~8.7 ps/nm/km. We expect soliton-like pulse formation where the GVD and SPM counter-balance. Two polarisation independent optical isolators are used to ensure single direction oscillation. The fibre laser is pumped through a 980/1550 WDM from a grating stabilised 975 nm laser diode (from SDL), which can provide up to 300 mW pump power. A set of commercial laser diode driver and temperature controller (Newport 505B & 300) is used for stabilising the pump laser. Two fibre polarisation controllers are located before and after the 45°-TFG. A 10:90 fibre coupler is employed for which the 10% port is used to couple out the laser light. The laser output is connected to another isolator to ensure that unwanted reflection does not couple back into the laser cavity.
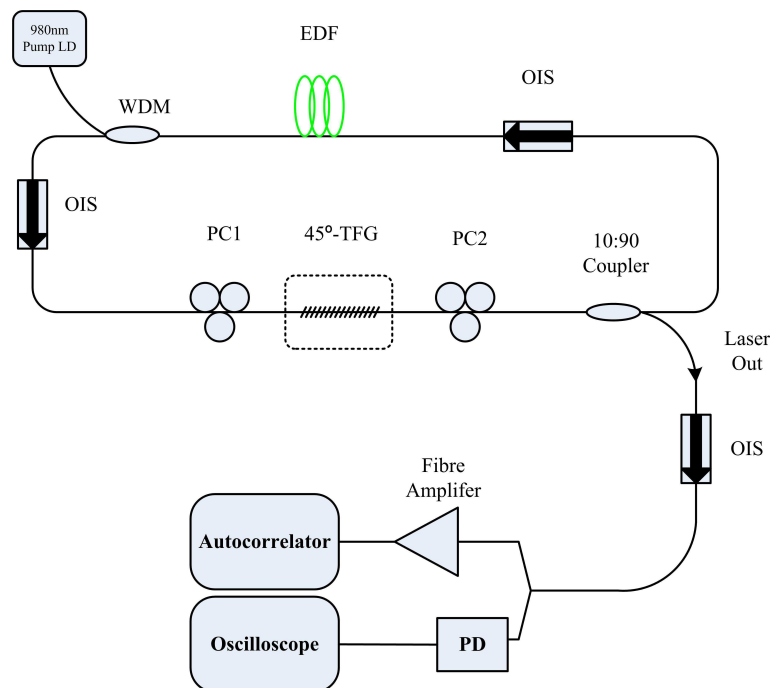
Figure 4.26 Schematic configuration of the 45°-TFG based mode locked femtosecond fibre laser. The output is split into two parts so that the autocorrelation trace and oscillogram can be viewed in the same time.

The effect of NPR with the 45°-TFG based in-line polariser provides the necessary intensity discrimination for mode locking. Since the net GVD is anomalous, GVD and SPM counter-balance to give soliton-like pulses. By properly adjusting the two PCs in the system, stable mode-locked pulses can be obtained. The optical pulses have been amplified and then fed through to an autocorrelator whose resolution is 44 fs (from INRAD Inc. MODEL 5-14B). Figure 4.27(a) shows the auto-correlation trace of the pulse corresponding to a pulse duration of ~600 fs. Figure 4.27(b) shows the optical spectrum of the fibre laser centred at 1553 nm with a spectral bandwidth at full-width half-maximum (FWHM) of ~9 nm, thus giving a time-bandwidth product of ~0.6, indicating the pulse is slightly chirped. A typical pulse train is shown in Figure 4.27(h) with a 90 ns interval between two adjacent pulses, giving a repetition rate of 10.34 MHz. The output pulse power is 12 mW which corresponds to the output energy of ~1 nJ. By adjusting the two sets of polarisation controllers, the mode locked wavelength exhibits a certain degree of tunability from 1548 nm to 1562 nm with pulse durations from ~600 fs to ~1 ps. This is shown in Figure 4.27(c)-(g)
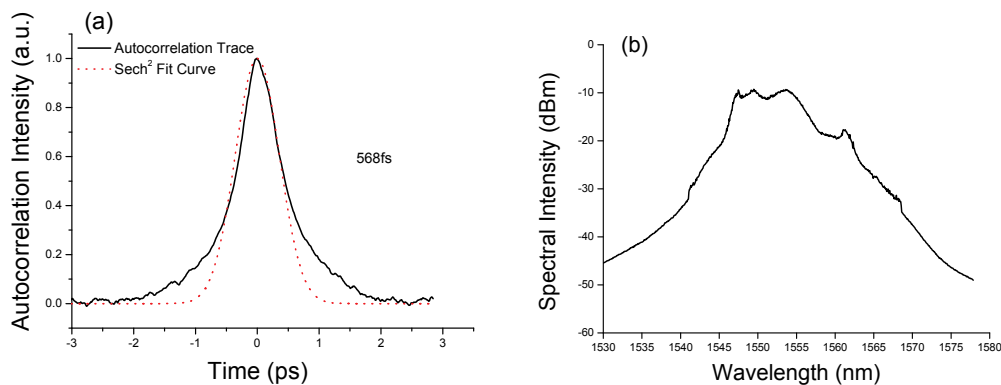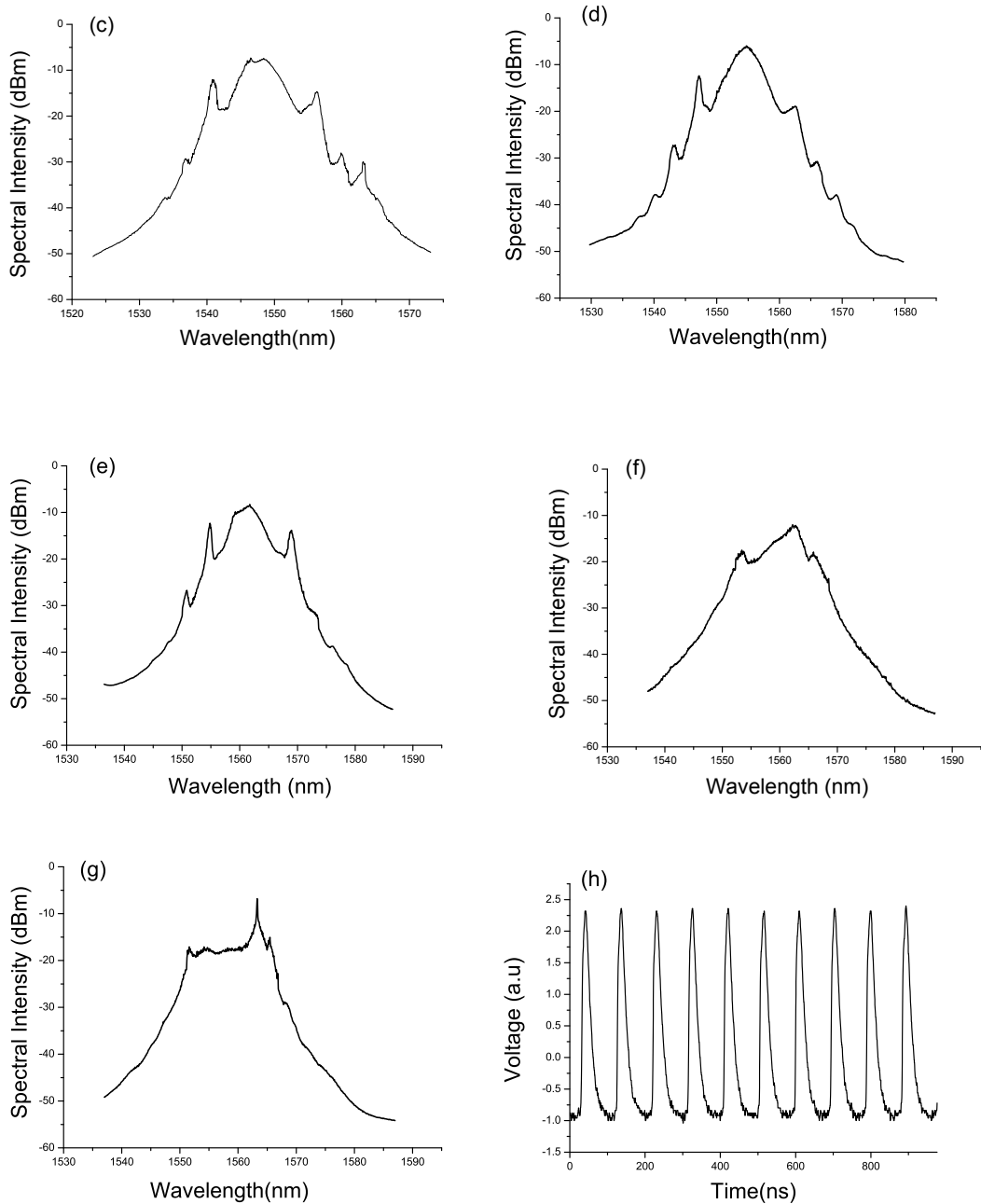
Figure 4.27 Measured typical auto-correlation trace and the corresponding sech2 fit of (a) laser mode locked at 1553 nm; optical spectrum of laser mode locked at (b)1553 nm, (c)1546 nm, (d)1554 nm, (e)1561 nm, (f)1562 nm, (g)1560 nm; (h) a typical output pulse train of the mode-locked fibre laser from the oscilloscope showing a repetition rate of ~10.34MHz.

The measured pulse width and time-bandwidth product (TBP) as a function of the wavelength are shown in Figure 4.28. Since the TBP of the output pulses is larger than 0.3, the output pulses are not transform limited. However, simple optimization of

the cavity design (fibre lengths, etc.) could lead to transform limited pulses at the output coupler.
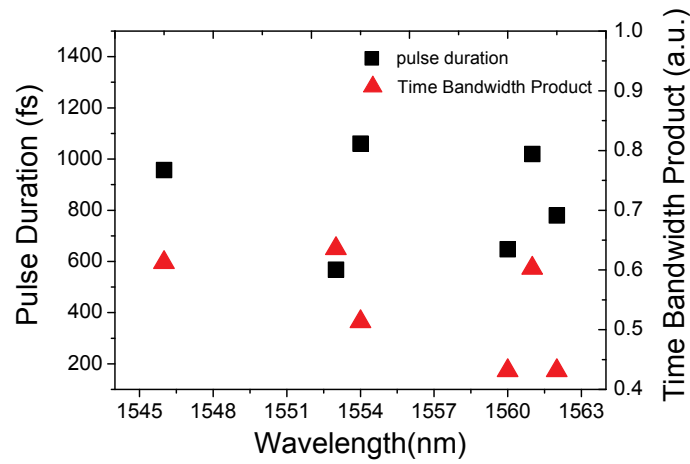
Figure 4.28 Measured pulse width and time-bandwidth products as a function of the wavelength.

We have also measured the Frequency Resolved Optical Gating (FROG) spectrogram of the output laser pulses. FROG detection can provide a more accurate measurement of the laser pulses while showing phase information. Figure 4.29 depicts the main FROG measurement results.
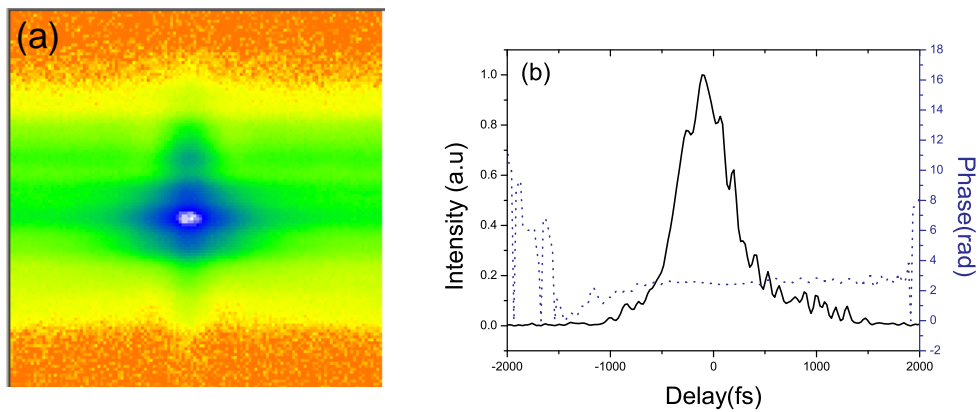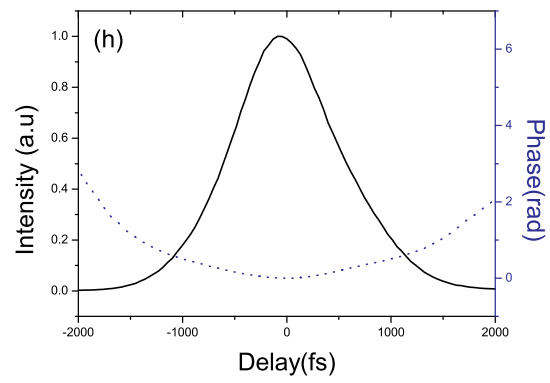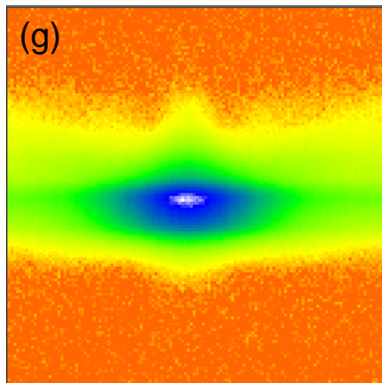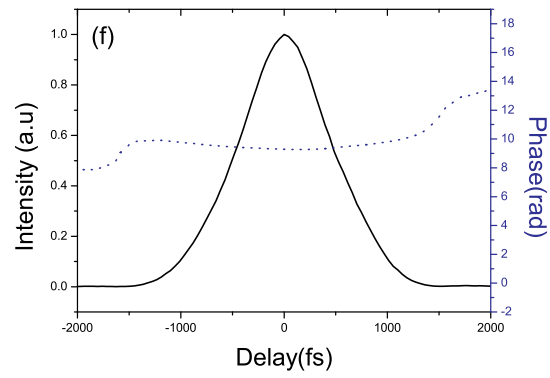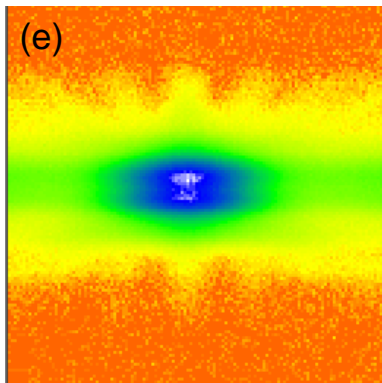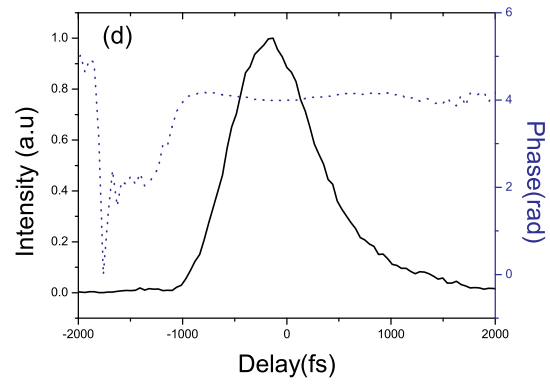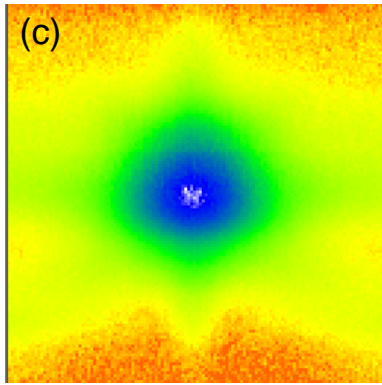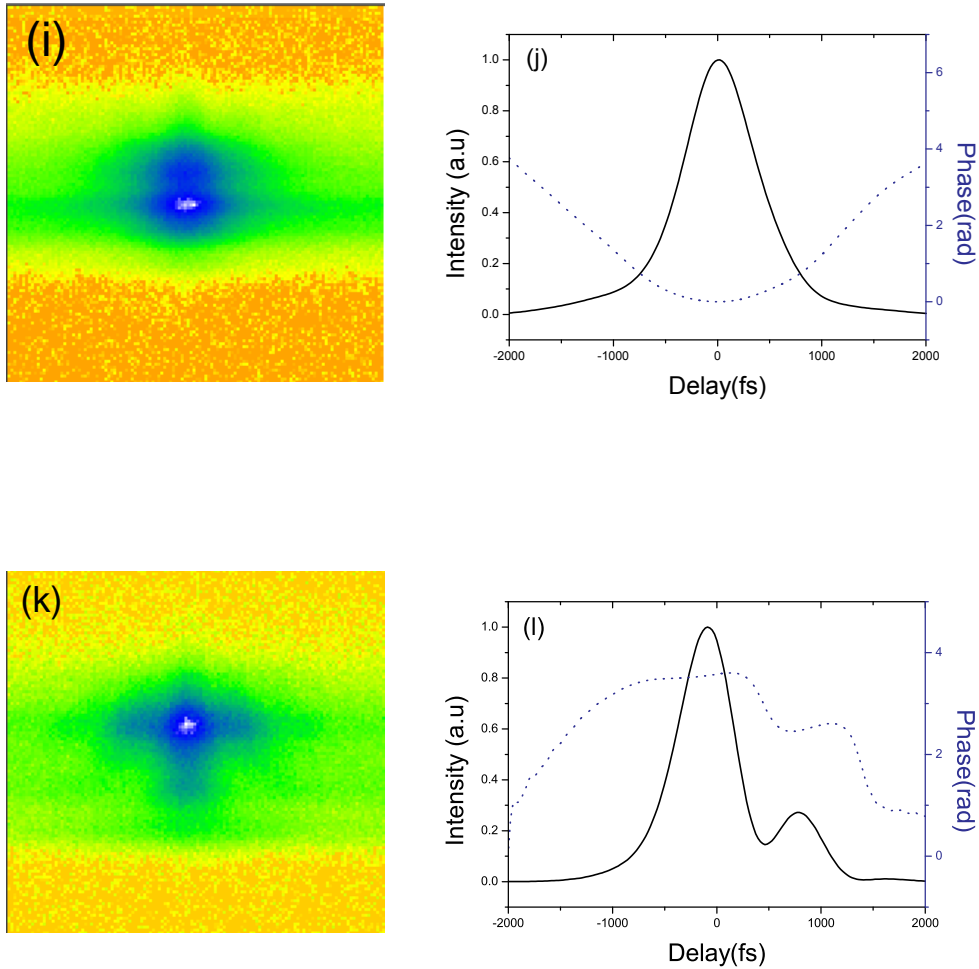
Figure 4.29 FROG traces and the corresponding retrieved pulse shape and phase information for (a)&(b)1553 nm, (c)&(d)1546 nm , (e)&(f)1554 nm, (g)&(h)1561 nm, (i)&(j)1562 nm, (k)&(l)1560 nm.

Figure 4.29 describes the FROG traces, the corresponding pulse shape and phase information of various pulses obtained in Figure 4.27. Because auto-correlation only provides the pulse duration assuming the pulse has certain shape i.e. $\sec h^2$ which is the typical soliton case, it does not give the actual pulse shape. In Figure 4.29(f), (h) and (j), the pulses we obtained were shown to be quasi-$\sec h^2$, while in Figure 4.29(b), (d) and (l) the pulses shape show distortion from $\sec h^2$. This distortion may due to the imperfect balance between SPM and GVD for different polarisation rotation. Also, Figure 4.29(h) and (j) tell that there is frequency chirp in the output pulses and the chirp effect is negligible in other situations.

Although the 45°-TFG has functioned as a high efficiency polarisation element to

achieve mode locking in a net-anomalous dispersion laser cavity, it can be used in a variety of mode locked fibre laser configurations. For example, future studies will pursue the use of this all-fibre configuration (such as all-normal dispersion fibre lasers [198-199]) to achieve higher pulse energies.

4.4 Chapter Conclusions

This chapter presents the experimental investigation of the functionality and application of 45º- and ex 45º -TFG in EDFLs emitting continuous wavelength switchable laser light of single polarisation and femtosecond pulses in the region of 1.5 μm.

The results were clearly shown that the 45º-TFG functions as an efficient device in polarising the intra-cavity laser beams. Also, the combination of both 45º-TFG and ex-45º TFG used as intra-cavity polariser and PDL filter enabled the EDFLs operating at single, dual, triple and quadruple wavelengths of with single polarisation status. The EDFLs exhibited stable output laser beam at designated wavelength with high DOP > 99.8%. This indicates a highly polarised output laser beam with good signal quality. Due to the long cavity length of the EDFLs, single mode operation was not expected at this situation. However, methods to achieve single mode operation have been proposed for further improvement of the laser performance such as by inserting a saturable absorber [200] or narrow band filters [201]. The EDFLs demonstrated in this chapter have also shown capability of tuning from which tunable EDFL or EDFL based laser sensor systems could be developed.

In addition to continuous operation, the application of 45º-TFG in a standard fibre ring cavity has successfully acted as a saturable absorber, mode locking the laser producing femtosecond scale soliton laser pulses based on the NPR effect of the cavity incorporated with the 45°-TFG. The utilisation of the 45º-TFG, this laser has demonstrated wavelength tuning within a certain range. Both auto-correlation and FROG measurement have been done with respect to the output laser pulses, showing detailed information regarding the output laser pulses. The mode-locked laser demonstrated in the chapter was an initial experiment of the 45º-TFG application in nonlinear photonics, therefore further optimisation of the laser cavity might be required to produce ideal laser pulses. Furthermore, this implementation could be

extended to 1 μm region for future investigation that could generate high energy laser pulses.

Chapter 5

45º- and Ex 45º- Tilted Fibre

Gratings –On the Application of

Optical Fibre Sensors

5.1 Introduction

As mentioned in Chapter 2, fibre gratings can offer smart solutions in test and measurement fields. They appear to be ideal candidates as sensors due to their light weight, ease of fabrication and EMI resistance. Previously, most sensing applications have been based on FBGs and LPGs. Recently, TFGs have shown potential in the domain of optical sensing. Chehura *et al* presented a temperature and strain discrimination sensor using a single TFG [202]. Shao *et al* implemented a directional bend sensor with a TFG [203]. Shao and Albert reported an inclinometer incorporating both a TFG and a section of fibre taper [134]. Guo *et al* presented a displacement sensor using non-uniform TFG showing temperature resistance [162].

Recently, optical bio-/chemical-sensors have attracted a lot of interests because they can provide real-time, accurate and low cost measurement of bio-species. TFGs have already exhibited excellent performance in refractive index (RI) measurement which is an important property of most bio/chemical samples. An etched TFG structure in multimode fibre has been shown in performing chemical-sensing application [204]. Cladding modes coupling of TFG has been used for RI sensing from which transmission spectrum change can be detected [205]. Offset splicing aiming for reflected cladding modes coupling monitoring of a TFG has been applied as a low cost in-fibre refractometer [206]. Surface Plasmon Resonance (SPR) using TFGs have also been demonstrated for RI sensing [207-208]. Miao *et al* designed a humidity sensor based on RI change of the coating layer of a TFG. A more systematic investigation of applications of TFGs at 800nm was reported by Suo *et al* including strain, temperature and RI responses [209].

So far, most of TFGs used in sensors have small tilted angle. 45°- and ex 45°-TFGs have been less investigated in sensor systems. Zhou *et al* reported an in-fibre refractometer of high responsivity with low thermal cross sensitivity using an ex 45°-TFG [15]. Chen *et al* demonstrated a twist sensor using an ex 45°-TFG [14]. In this chapter, it further explores the application 45°- and ex 45°-TFGs on the application of optical sensors. First, it will demonstrate a liquid level sensor using an ex 45°-TFG. Then, it will report a fibre laser based twist sensor and strain sensor incorporating an intracavity ex 45°-TFG, which offers low-cost time domain signal demodulation for

twist and strain sensing. Then, it will propose a fibre laser based loading sensor, which is the application of 45º-TFG based single polarisation fibre laser. Finally, the conclusion will be presented at the end of the chapter.

5.2 Liquid Level Sensing Using Ex 45º-TFG

5.2.1 Introduction to level sensing

Liquid level sensing is of great interest for a range of industrial applications. Traditional liquid level sensing is mostly based on mechanical [210] and electrical [211] techniques. Although electrical sensors are widely applied, they have the disadvantage of not being suitable for conductive and explosive environments. However, optical sensors are immune to EM interference and more desirable for such hazardous situations. Over the last decade, a range of liquid level detectors based on optical fibres have been developed, including using micro-bending optical fibre [212], a cantilever based FBG [213], a high-birefringence-fibre loop mirror [214] and a Fabry-Perot optical fibre cavity [215]. Low-cost liquid level sensor utilising the measurement of fibre total internal reflection induced intensity change is also reported [216-218]. Recently, Khaliq *et al* demonstrated a LPG based liquid level sensor utilising the detection of surrounding medium refractive index [219]. Their results showed that LPG based level sensor can provide better performance only for liquids with refractive index much higher than water based solutions. This section demonstrates an optical fibre liquid level sensor based on RI response of an ex 45º-TFG.

5.2.2 Grating characteristics

The ex 45º-TFG used in our liquid level sensing experiment was UV-inscribed in standard single mode fibre. Detailed information regarding the fabrication can be found in §3.5.2. The ex 45º-TFG has ~78º internal angle with a length of ~ 12 mm. The fabricated 78º-TFG has been annealed at a temperature of 80°C for 24hours for stabilisation. The measured optical spectrum and polarisation properties of the 78º-TFG can be referred to Figure 3.26.

As the mode coupling involving high order cladding modes, the 78º-TFG is intrinsically sensitive to RI change. Its RI response has been discussed in detail in §3.5.3.2. It is also noted that when the 78º-TFG was submerged in water, degeneration of the two orthogonal polarised modes occurred, i.e. the paired peaks merged to one strong peak and shifted to the longer wavelength side, as shown in Figure 5.1. It is this wavelength shift under water provides a capability of an ex 45°-TFG for liquid level sensing.
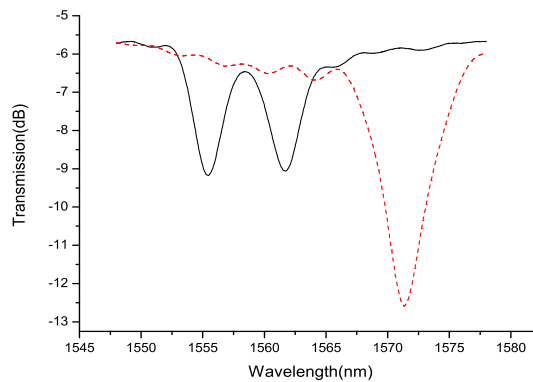
Figure 5.1 The transmission spectra of a 78º-TFG when it is in air (black solid line) and immersed in water (red dotted line).

5.2.3 Liquid level sensing experiment

In the liquid level sensing experiment, the section of the fibre containing the grating was taped to a plastic tube and then immersed into the water in a beaker. A slot was milled on the surface of the tube to house the fibre grating ensuring in full contact with water and also maintaining grating straight to eliminate any effect from bending. The beaker was mounted on a vertically driven micrometer stage to control the water level on the submerged 78º-TFG. Thus during the whole experiment, there was no fibre movement involved. The schematic diagram of the experimental setup is shown in Figure 5.2(a).

When the 78º-TFG is partially immersed in the water, it can be regarded as constituting two individual gratings surrounded by air and water, respectively. Thus, if we concentrate on one pair of cladding modes of the 78°-TFG we can see on the

spectrum a paired loss peak plus a broad peak on the longer wavelength side; the former is generated by the air-surrounded section and the latter by water-surrounded section of the grating. Because the polarisation mode dispersion (PMD) of the cladding modes will change with the water level, we have evaluated the 78º-TFG spectral response to the water level change by examining the fast- and slow-axis mode using polarised light. Figure 5.2(b) shows transmission spectra when the slow-axis mode around 1560 nm is coupled for three different liquid levels: the left peak (red solid line) indicates that the grating fully exposed to air surrounding, the middle two peaks (blue dashed line) occur when the grating is immersed in a half way to the water and the single peak (black dotted line) on the right shows that the grating is fully immersed under water.

(a)

(b)

(c)

(d)
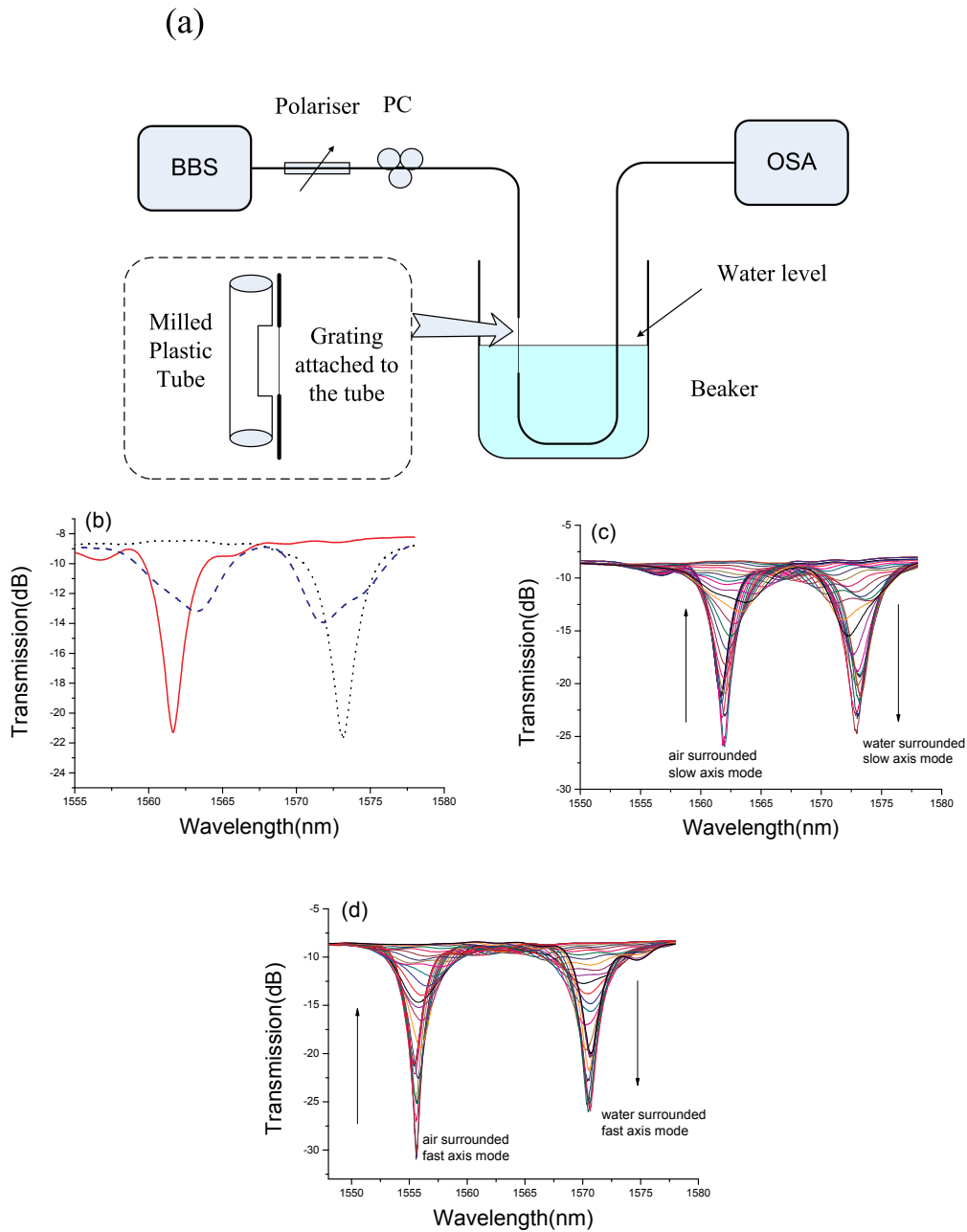
Figure 5.2 (a) schematic diagram of the experimental setup for liquid level sensing; (b) Transmission spectra of the 78°-TFG for slow-axis mode coupling around 1560 nm: the left-side (red solid line) , right-side (black dotted line) single peak and the middle dual peaks (blue dashed line) corresponding to the grating surrounded by air, water and half way in water. The air- and water-surrounded peaks evolving with increasing water level for (c) slow-axis mode and (d) fast-axis mode.

Figure 5.2(c) displays the spectral evolution of the slow-axis mode when the 78°-TFG

was surrounded from entirely by air to water. It is shown that with increasing water level, the loss of the air-surrounded mode decreases whereas the loss of the water-surrounded mode increases. The fast-axis mode showed a similar spectral evolution, as displayed in Figure 5.2(d). Figure 5.3(a) and Figure 5.3(b) plot the transmission loss against submerging length of the 78º-TFG in water for the fast- and slow-axis mode, respectively.
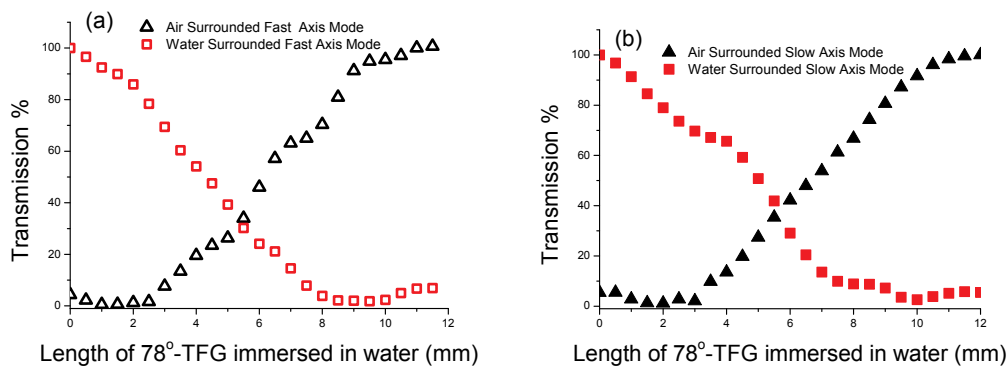
Figure 5.3 Transmission change measured for the length of the 78°-TFG in water for the grating sections surrounded by water (■,□) and by air (▲,△) for (a) fast-axis mode and (b) slow-axis mode.

By examining Figure 5.3 we can see that by monitoring the transmission loss of the fast-axis or slow-axis mode of the 78°-TFG, the water level can be measured. However, one can notice that there is an initial insensitive range from 0 mm to 3 mm for the air-surrounded modes. After this insensitive region, the grating responding to the water level from 3 mm to 10 mm is quite linear followed by a secondary insensitive region from 10 mm to 12 mm. While for the water-surrounded modes, the grating exhibits linear response to water level from 0 mm to 8 mm and becomes insensitive from 8 mm to 12 mm. The reason why the sensing range is different between the air-surrounded and water-surrounded mode is not clear so far. To get a better interpretation on the liquid level sensor, the results have been re-plotted in Figure 5.4 by excluding the insensitive region.
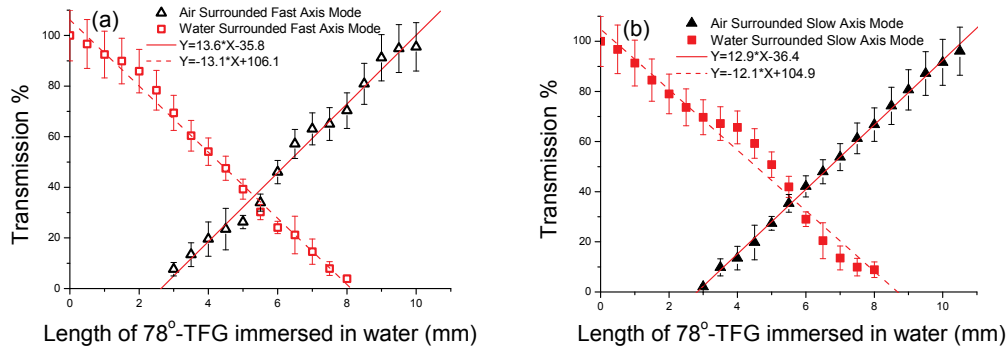
Figure 5.4 Re-plots of transmission change for the length of the 78°-TFG in water (■,□) and in air (▲,△) for (a) fast-axis mode and (b) slow-axis mode.

In Figure 5.4(a), it can be seen that although the sensing range of the air-surrounded and the water-surrounded fast-axis mode is different, the sensitivity for both modes are quite similar which is ~ 13 %/mm. While in Figure 5.4(b), the air-surrounded and the water-surrounded slow-axis mode show a sensitivity of ~ 12 %/mm. This is more than twice of the sensitivity of the LPG based liquid level sensor which is 4.8 %/mm [219]. Therefore, both fast-axis and slow-axis mode can be used for water level sensing with similar sensitivity and measurement range. The measurement uncertainties mainly arise from the OSA with a quoted accuracy of 7 % (0.3 dB) in level measurement and the environmental effect because the device is polarisation sensitive. We found that, in general, ~ 10 % gives reasonable measurement error range for linear fit of the data. Nevertheless, for water-surrounded modes, when the transmission is getting lower, the uncertainty can increase up to ~ 35 %. This is because when the transmission of the peak gets smaller, it may reach the sensitivity limit of the OSA which will generate extra reading errors to determine the transmission.

Although LPGs based liquid level sensors have been demonstrated, their intrinsic high temperature cross-sensitivity limits their use in real application and thus a temperature compensation scheme is normally required. By evaluating the temperature sensitivity of the 78°-TFG (shown in Chapter 3), it is found that the thermal sensitivity of the 78°-TFG is lower than that of a standard FBG, then much lower than that of an LPG. Therefore, temperature compensation scheme may not be necessary with the ex 45°-TFG as a water liquid level sensor. However, it must be pointed out that the

measurement range of both the LPG and ex 45°-TFG based liquid level sensor is limited by the length of the grating.

5.3 Fibre Laser Twist Sensor System Using an Ex 45º-TFG

5.3.1 Introduction

Embedded twist sensors are important devices to monitor the health condition of engineering structures and have been received considerable attention for smart structure applications. Traditional twist sensors are based on angle measurement devices like optical encoders and magnetic sensors [220]. Optical fibre grating based twist sensors are intrinsically small and easy to implement. For example, a corrugated LPG has been demonstrated for twist sensing [221]. Unfortunately, this type of sensor can not address the twist direction. Wang and Rao proposed a CO_2 laser fabricated LPG based twist sensor which can measure both twist angle and direction [222]. Tilted fibre grating using polarisation properties has also been described as a passive twist sensor with capability measuring both twist direction and rate [14]. However, so far, most of the reported optical twist sensors are all passive and need expensive optical spectrum analyser and external broadband source to demodulate the optical signal. In this section, a low-cost time domain measurement based twist sensor using an ex 45º-TFG incorporated in a fibre laser cavity will be presented. By measuring the fibre laser build-up time using a low cost photodiode and a standard oscilloscope, both twist direction and angle can be identified simply.

5.3.2 Experimental setup and operation principle

5.3.2.1 Characteristics of FBG and ex 45º-TFG

For this experiment, a uniform FBG and an ex 45º-TFG were fabricated. The internal angle of the ex 45º-TFG is ~79°. A phase mask with a period of 1.07 µm was used to UV-inscribe the normal FBG with a reflectivity of ~6 dB at 1551nm. As mentioned in Chapter 3 that ex 45º-TFGs exhibit strong polarisation mode splitting property, the fabricated 79°-TFG has shown pronounced dual-peak features on its transmission spectrum, induced by the PMD. Figure 5.5(a) gives the transmission spectra of the

79°-TFG from 1200 nm to 1700 nm showing pairs of loss bands. Figure 5.5(b) shows the transmission spectra of one paired polarisation loss peaks of the 79°-TFG for the launched light at three different polarisation states and Figure 5.5(c) shows the transmission interchange when the polarisation state changes from fast-axis mode to slow-axis mode under applied twist.
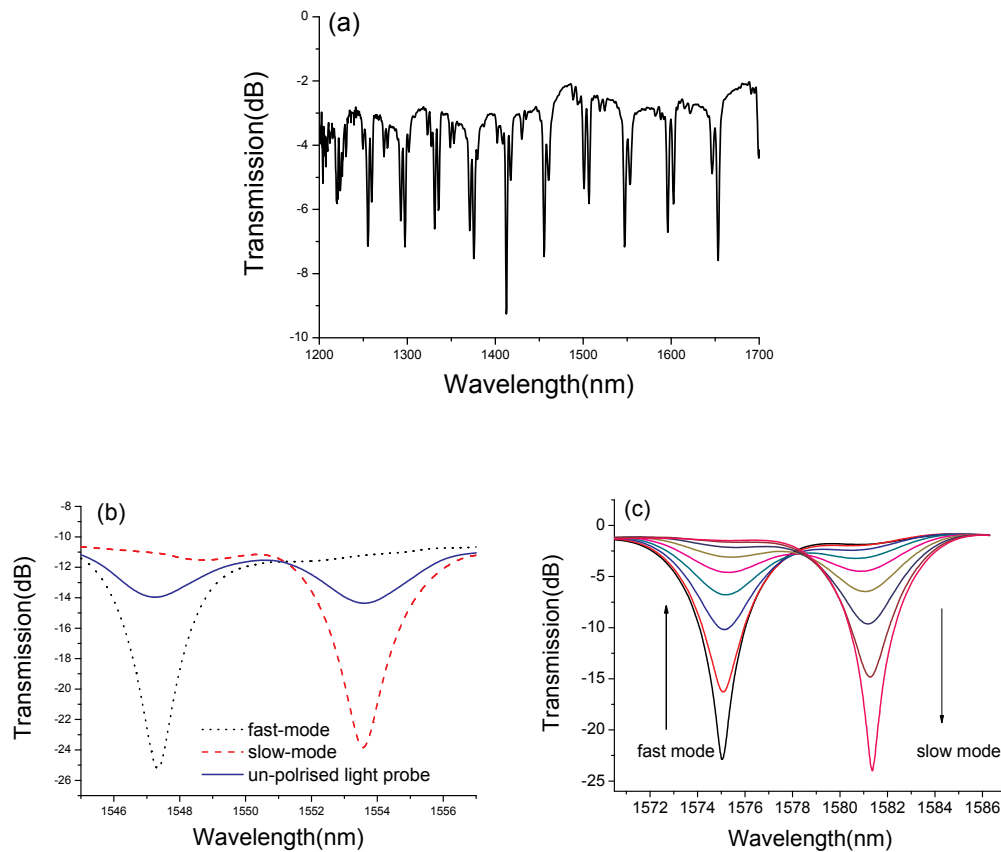
Figure 5.5 (a) Optical transmission spectra of the 79º-TFG in the range from 1200 nm to 1700 nm; (b) Spectra of the 79º-TFG probed by un-polarised light (blue solid line) and polarised light at two orthogonal states (black dotted line and red dashed line); (c) the transmission interchange between the split peaks when the polarisation state changes from fast mode to slow mode.

5.3.2.2 Ex 45º-TFG based fibre laser twist sensor system

The set-up for the proposed ex 45º-TFG based fibre laser twist sensor system is shown in Figure 5.6(a). In this configuration, the gain medium is a ~1 m Erbium/Ytterbium co-doped fibre, which is pumped by a 975 nm laser diode through

a 980/1550 nm WDM coupler. A 3 dB coupler formed a Sagnac loop is employed as the high reflection mirror in the laser cavity. The pump is modulated by a square wave through a standard function generator at 5 Hz. The laser output is connected to a low noise photodiode, and the build-up time is measured via a two-channel digital oscilloscope (Tektronix TDS2012).
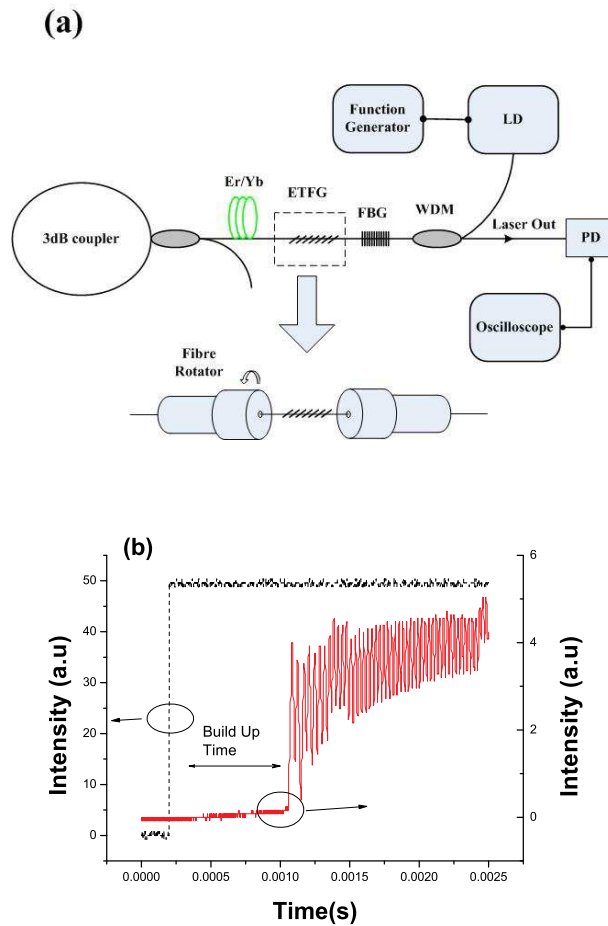
Figure 5.6 (a) Schematic diagram of the proposed ex 45°-TFG based fibre laser twist sensor system; (b) Typical build-up time trace of the fibre laser observed on a digital oscilloscope. Modulation signal is shown in dotted line; laser output signal is shown in solid line.

5.3.2.3 Twist sensing principle

In a modulated laser system, when the pump is switched on, the laser will reach a stable state after a series of relaxation oscillation. Thus, there is a finite build-up time associated with each lasing state at certain pump and loss conditions. Therefore, if the

gain medium and the pump condition are not changing, the laser build-up time is only related to the intracavity loss. Because the ex 45º-TFG itself is a PDL filter, when an ex 45º-TFG is inserted to the laser cavity and subject to twist, the intracavity loss will be modulated accordingly, hence affecting the laser build-up time. Based on this principle, the twist experienced by the grating can be monitored by measuring the build-up time of the laser cavity. Figure 5.6(b) shows a typical oscillation trace of the laser oscillation build-up process.

5.3.3 Experimental results

In the experiment, a segment of laser cavity fibre with an UV-inscribed ~12 mm 79°-TFG was fixed by a clamp on one side and the other side was mounted on a fibre rotator, as shown in Figure 5.6(a). The fibre was under a little tension to position fibre straight in order to eliminate the crosstalk induced from other effects such as axial strain, bending etc. In the experiment, the lower and upper modulation pump levels were first set at constant values of 14.6 mW and 43.3 mW, respectively, and the clamped fibre was twisted from 0 to 150° with an increment of 10° in both clockwise and anti-clockwise direction. The build-up time was measured for each twist and the normalised results are plotted in Figure 5.7(a). From the figure we can see clearly that at the initial position, i.e. under 0° twist, the 79º-TFG induced loss is at maximum, so the build-up time is at largest value. When the fibre is twisted in clockwise and anti-clockwise direction, the 79°-TFG induced loss decreases and the build-up time reduces accordingly with increasing twist. This twist experiment was repeated for a lower pump modulation level set at 24 mW and we saw that the overall twist sensitivity was decreased for this lower pump modulation level, as the lower trace shown in Figure 5.7(a). Obviously, this is because a higher pump power would provide higher gain for the laser system therefore only a shorter build up time is necessary. For a better interpretation of the results, we re-plot the results for twist applied in clockwise and anti-clockwise direction separately in Figure 5.7(b) and Figure 5.7(c). From these two figures we can see the system gives a near-linear response in the dynamic range ±140°, giving an estimated twist sensitivity of ~412 µs/(rad/m). Under the current configuration, the resolution of the oscilloscope is 10 µs, the resolution of our proposed twist sensor is therefore ~ 0.02 rad/m. One need note

that the time scale resolution of the oscilloscope depends on the range i.e. second/division due to the limited record length of 2500 points at all time bases. More importantly, we see if the system is set at a defined position, i.e. at ±80° as shown in Figure 5.7(b) and Figure 5.7(c), the twist direction can be easily identified.
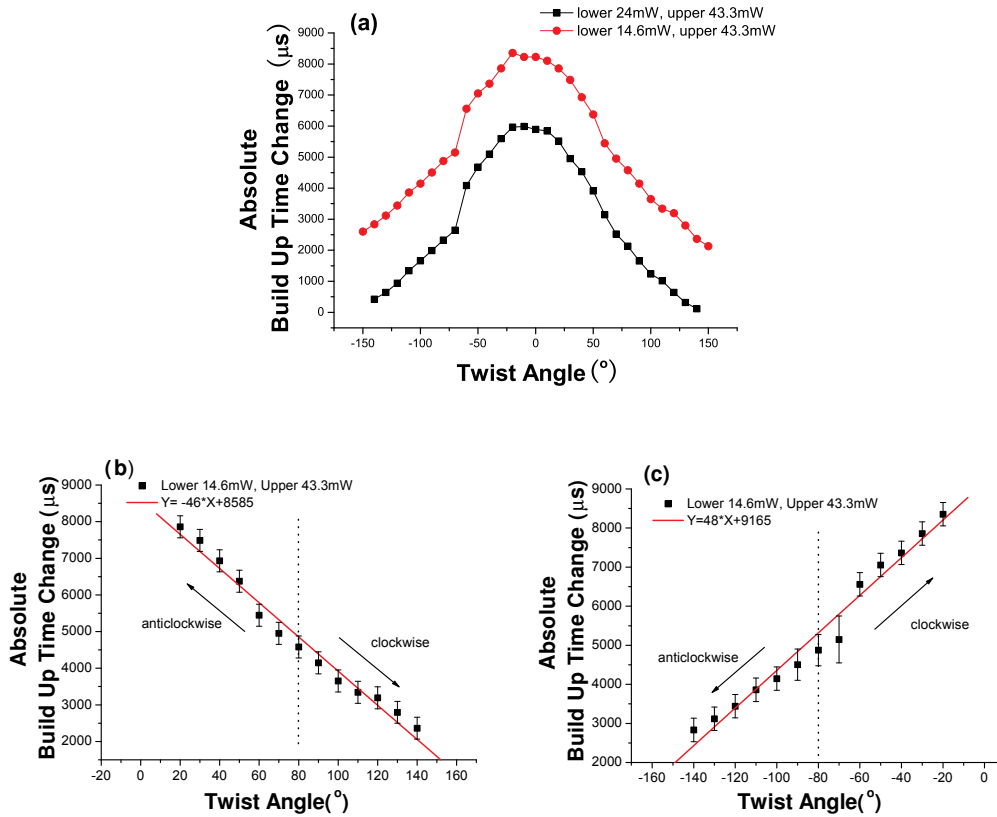
Figure 5.7 (a) Laser oscillation build-up time against twist angle for twist applied to clockwise and anti-clockwise direction for two different low modulation pump power levels, and re-plotted separately for (b) clockwise and (c) anti-clockwise direction to show the capability of identifying twist direction.

One may notice that when the twist angle varies from -80° to -60°, there is an obvious jump for the build-up time, as shown in Figure 5.7 (a). This could be attributed to the experimental error from rotating the fibre in the laser cavity, as there is no such jump for rotation angle from 0° to +140°. This is because the rotation of the grating inside the cavity could physically affect the adjacent part of the cavity which may induce unwanted polarisation effect to the output. Including the reading errors determining the build-up time, the uncertainty of the experiment could be on the level of ~500 µs.

5.4 Fibre Laser Strain Sensor System Using an Ex 45º-TFG

5.4.1 Introduction

FBG based fibre strain sensors have been extensively studied due to their intrinsic advantages and wide applications in industry. Conventional FBG strain sensors are mainly based on wavelength shift monitoring. Furthermore, various other techniques have also been developed to interrogate FBG sensors. These include direct wavelength analysis [223-224], phase and delay measurement [225] and optical intensity monitoring [226].

Although the passive detection of wavelength shift can offer smart solutions, the systems are still subjected to complexity. Normally, in this case, an additional light source is necessary. Active strain sensors using fibre laser configuration provide an alternative measurement method with higher signal to noise ratio while having a less complicated system. Ball *et al* demonstrated a laser strain and temperature sensor for single and multi point measurement [227]. A fibre laser using a chirped FBG and a mechanical strength enhanced FBG have been developed for high temperature measurement up to 300 ℃ [228]. Another approach involves a semiconductor optical amplifier which can support multiple sensor heads for simultaneous multipoint measurement [229].

Moreover, most of the active sensing systems rely on optical domain signal demodulation from which the cost is high. Time domain signal demodulation offering low system cost has been reported through integrating a conventional LPG in a linear laser cavity [230]. In this section, a fibre laser strain sensor incorporating an ex 45º-TFG will be presented and discussed. In this fibre laser sensor system, low cost time domain signal demodulation is achieved by monitoring the build-up time of the modulated laser cavity.

5.4.2 Experimental setup and sensing principle

The set-up for the proposed fibre laser strain sensor system is shown in Figure 5.8(a). The ex 45º-TFG is mounted on a fibre stretcher. As illustrated in Figure 5.8, the fibre stretcher consists of two fibre clamps which hold the fibre firmly within a fixed length.

One fibre clamp is connected with a micrometer through which various strains can be applied. The pump LD is modulated by a square wave through a standard function generator at 5 Hz. The laser output is connected to a low noise photodiode, and the build-up time is measured via a two-channel digital oscilloscope (Tektronix TDS2012).
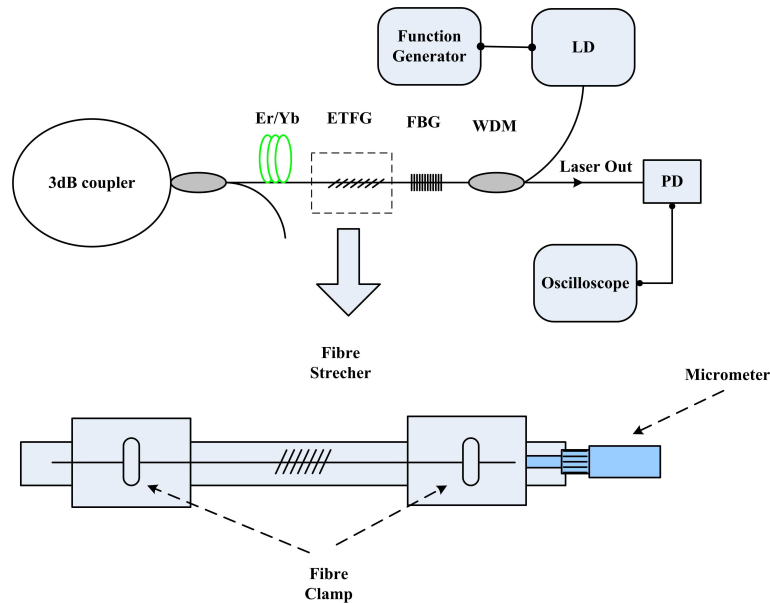
Figure 5.8 Schematic configuration of ex 45°-TFG based laser strain sensor system.

As mentioned in §5.3.2.3, the build-up time of the laser system is subject to the loss change of the cavity in a modulated laser system when gain and pump condition not varying. Because the ex 45º-TFG has spectral loss bands, when it is subjected to mechanical strain in the laser cavity, the loss band will then shift accordingly [114], so that the cavity loss is related with applied strain and the build up time of laser system will change correspondingly. Therefore the strain can be detected by monitoring the build up time of the laser system.

5.4.3 Experimental results

In the experiment, the same 79º-TFG as in §5.3 has been used. By tuning the micrometer, it can apply strain from 0 με to 2000 με on the 79º-TFG. When the 79º-TFG is at 0 με, the loss maximum in the laser cavity which gives out the longest build-up time. While the strain increases, the loss bands will have a blue shift [114]

thus decreasing the cavity loss which results in a shorter build-up time of the system. A typical laser output spectra change is illustrated in Figure 5.9(a).

The system was firstly set the lower and upper level modulation pump at constant value of 14.6 mW and 112.4 mW individually. The build-up time was then measured for the strain applied on the 79°-TFG with an increment of 100 με. The absolute build-up time change against the applied strain on the 79°-TFG is depicted in Figure 5.9(b). From Figure 5.9(b) it can be seen that, initially when the 79°-TFG is under no strain, the laser cavity suffers the maximum loss therefore exhibiting the largest build-up time. The experiment was then repeated for a lower pump level at 24 mW. In the experiment, it was found that this laser strain sensor system will subject to the saturation of the applied strain for lower pump levels. However, the system saturates in a smaller strain range when the lower pump level is set at a high value. This is mainly because when the pump power becomes higher the gain of the system also increases. The gain increase would therefore reduce the system build-up time. Furthermore, as the strain increases, the system would suffer less loss hence reduce the build-up time. Thus, this high pump level induced gain increase and strain induced loss decrease could significantly reduce the sensitivity and measurement range of the system. For a better understanding of the experimental output, the results have been re-plotted in Figure 5.9, showing the linear range of the sensor response for two different lower pump levels – 14.6 mW (c) and 24 mW (d). It can be seen from the figure that, when the lower pump level is 14.6 mW, the sensor system can measure strain from 0 με to 1000 με with a linear responsivity of ~500 ns/με. With the time scale resolution of 1 μs from the oscilloscope, the system gives out a resolution of ~ 2 με. The sensor then reaches its saturation point when the applied strain is over 1000 με. For lower pump level at 24 mW, the sensor is only capable of measuring strain from 0 με to 500 με with a linear strain responsivity of ~349 ns/με, because the time scale resolution of the oscilloscope is 0.1 μs, the system gives out a resolution of ~ ~0.3 με. We need notice that, during the experiment, the time scale of the oscilloscope corresponding to different pump level is varied i.e. from 100 ns/div to 1 μs/div thus change the time base resolution from 0.1 μs to 1 μs. This resolution change along with reading errors may lead to the build up time uncertainty of ±5 μs and ±10 μs for lower pump level at 24 mW and 14.6 mW respectively.
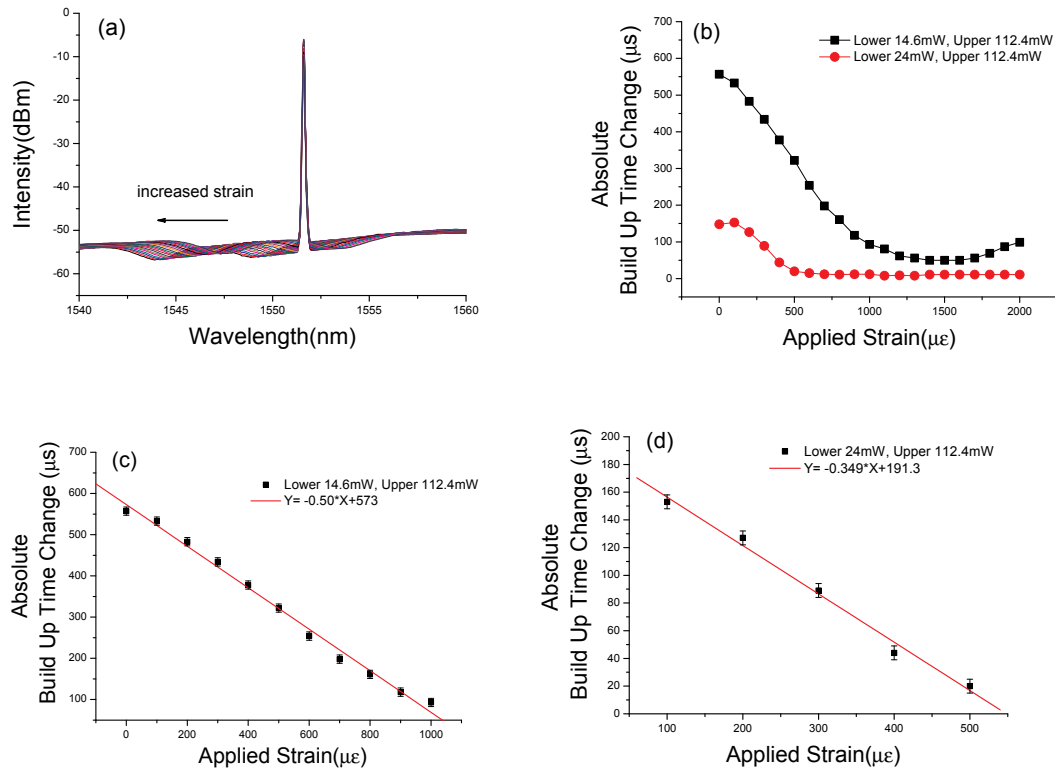
Figure 5.9 (a) Typical output spectra when the 79°-TFG is under strain; (b) Laser oscillation build-up time against applied strain on 79°-TFG for two different lower modulation pump power levels. Re-plotted build-up time against strain for (c) lower pump level 14.6 mW with applied strain from 0 με to 1000 με (d) lower pump level 24 mW with applied strain from 0 με to 500 με.

5.5 Optical Loading Sensor Based on Single Polarisation Fibre Laser Incorporating an Intracavity 45°-TFG

5.5.1 Introduction

Optical sensors for loading measurement based on fibre grating technique have been extensively studied. Their fibre format and compact size are highly desirable in hazardous situations. FBGs fabricated in low-birefringence [231] and Hi-birefringence [232] fibres have been demonstrated. Liu *et al* designed a fibre load sensor using an LPG inscribed in conventional and Hi-birefringence fibre [233].

FBGs inscribed in multicore fibres have been reported for implementation of directional load sensors [234]. Directional load sensors using ex- 45° TFG has also been reported by Rui *et al* [235].

Yet, most fibre grating type loading sensors proposed so far are based on passive operation. They require external light source and optical spectrum analyser which would increase the cost of the system. In this section, a fibre laser using a 45°-TFG is proposed for load sensing purpose.

5.5.2 Sensing principle

According to §4.2.1, due to the polarising property of the 45°-TFG, fibre laser cavity incorporating an intracavity 45°-TFG could eliminate one polarisation state thus giving out single polarisation output. Since some degree of linear birefringence can be introduced when load is applied on silica fibre [236], the load can then alternate the intracavity polarisation state of a fibre laser. Within the laser cavity, the 45°-TFG works as a polarisation filter, therefore any variation of birefringence or polarisation in the laser cavity could change the laser output power. Hence, this laser system can be used as a load sensor.

The principle of the sensor system can be described by Jones matrix method.

$$\text{Equation 5.1} \quad \vec{E}_{in} = E \cdot \begin{bmatrix} \cos \alpha \\ \sin \alpha \cdot e^{i\phi} \end{bmatrix}$$

We may assume the single polarisation light $\vec{E}_{in}$ travelling in the fibre laser cavity having a general format described in Equation 5.1 using Jones vector, where E is the amplitude of the light field, $\tan \alpha$ is the ratio between the x and y component of the electric field and ϕ is the phase difference between the two orthogonal electric fields. The intensity of the input single polarised light is then given in Equation 5.2 by multiplying its complex conjugate.

Equation 5.2 $I_{in} = \vec{E}_{in} \cdot \vec{E}_{in}{}^{*} = E^{2}$

In general situation, as shown in Figure 5.10, an elliptical polarised light travels in the laser cavity. The angle between the axis of the polariser i.e. 45°-TFG and the y axis is θ. Within the same coordinate system, the load applied on the fibre will produce linear birefringence in x direction.
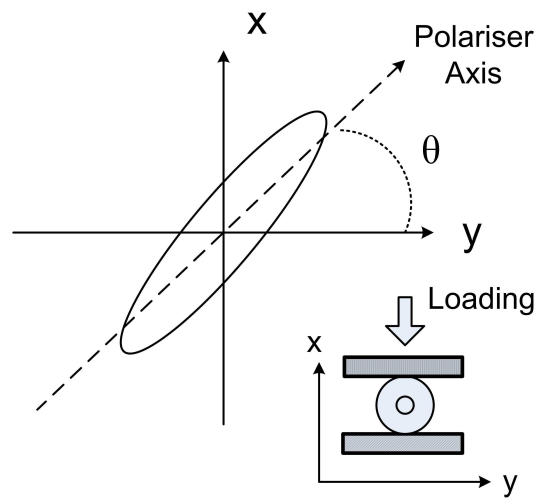
Figure 5.10 Birefringence induced by load applied to the fibre.

As a consequence, the light undergoing linear birefringence in x direction could transform to :

Equation 5.3 $\vec{E}'_{out} = E \cdot \begin{bmatrix} e^{-i\frac{\tau}{2}} & 0 \\ 0 & e^{i\frac{\tau}{2}} \end{bmatrix} \begin{bmatrix} \cos\alpha \\ \sin\alpha \cdot e^{i\phi} \end{bmatrix}$

Where $\begin{bmatrix} e^{-i\frac{\tau}{2}} & 0 \\ 0 & e^{i\frac{\tau}{2}} \end{bmatrix}$ is the Jones matrix expression of the load induced phase change,

where $\tau = \delta \cdot l$ is the phase retardation due to the applied load and δ is proportional to the load while l is interaction length. By increasing the applied load, τ can be varied between 0 and 2π. Therefore, we can write

Equation 5.4
$$\vec{E}'_{out\_x} = E \cdot cos\alpha \cdot e^{-i \cdot \frac{\tau}{2}}$$
$$\vec{E}'_{out\_y} = E \cdot sin\alpha \cdot e^{-i \cdot (\frac{\tau}{2}+\phi)}$$

When the light passes through the polariser as shown in Figure 5.10, the following relationship applies:

Equation 5.5 $\vec{E}_{Trans} = \vec{E}'_{out\_x} \cdot sin\theta + \vec{E}'_{out\_y} \cdot cos\theta$

Where $\vec{E}_{Trans}$ is the transmitted light after the polariser. By substituting Equation 5.4 into Equation 5.5 we can get:

Equation 5.6

$$I_{Trans} = \vec{E}_{Trans} \cdot \vec{E}_{Trans}^{*} = 2 \cdot E^2 \cdot \left[K^2 + M^2 + 4 \cdot M \cdot K \cdot cos\phi + K^2 \cdot cos\tau - M^2 \cdot cos(\tau + 2 \cdot \phi) \right]$$

Where $K = cos\alpha \cdot sin\theta$ and $M = sin\alpha \cdot sin\theta$. We now define the logarithm transmission loss induced by the loading induced birefringence change as:

Equation 5.7 $\delta_{loss}^{*} = \ln(\frac{I_{Trans}}{I_{in}})$

In an EDF laser, as it can be regarded as a quasi-three-level system, the output laser power can be written as in Equation 5.8 [184] :

Equation 5.8 $P_{out} = (\mu \cdot \dfrac{\Omega_b}{\Omega} \cdot \dfrac{1}{h \cdot \nu_p} - \dfrac{\Omega_b \cdot \varepsilon_a \cdot N \cdot l}{\varepsilon_e + \varepsilon_a} \cdot \dfrac{1}{\tau}) \cdot \dfrac{\delta_2}{2} \cdot (h \cdot \nu) \cdot \dfrac{1}{\delta} - \dfrac{\Omega_b}{\varepsilon_e + \varepsilon_a} \cdot \dfrac{h \cdot \nu}{\tau} \cdot \dfrac{\delta_2}{2}$

Where μ is the pump efficiency, Ω_b is the beam area in the active medium, Ω is cross section area of the active medium, ν is the frequency of the emitted photon, ν_p is the frequency of pump light, h is the Planck constant, l is the length of the active medium, N is the total number of the population in the laser level and ground level, ε_e is the effective stimulated emission cross section, ε_a is the effective absorption cross section, δ is the total logarithm loss of the laser system including cavity loss and mirror loss, δ_2 is the logarithm loss due to the output coupler of the laser system and τ is effective life time of the upper laser level. As in our laser system, only the intracavity loss varies while the loading changes, the other parameters are constant since the laser has a fixed setup. So, the output laser power is proportional to the birefringence change induced power loss.

5.5.3 Experimental configuration

The schematic of the laser sensor system is shown in Figure 5.11. The fibre laser consists of an EDFA, an isolator which ensures single direction oscillation, a PC, a circulator, a normal FBG as seeding wavelength, a 10:90 coupler and a 45º-TFG. Because the rest of the laser cavity is made of SMF-28, in principle, any part of the passive fibre before the 45º-TFG in the cavity can be used as a sensing element. The dotted circle in Figure 5.11 indicates the sensing fibre section. The sensing fibre has its plastic coating removed. The loading setup is shown in the dotted box with a stripped SMF28 fibre placed in parallel to the cavity fibre for balance.
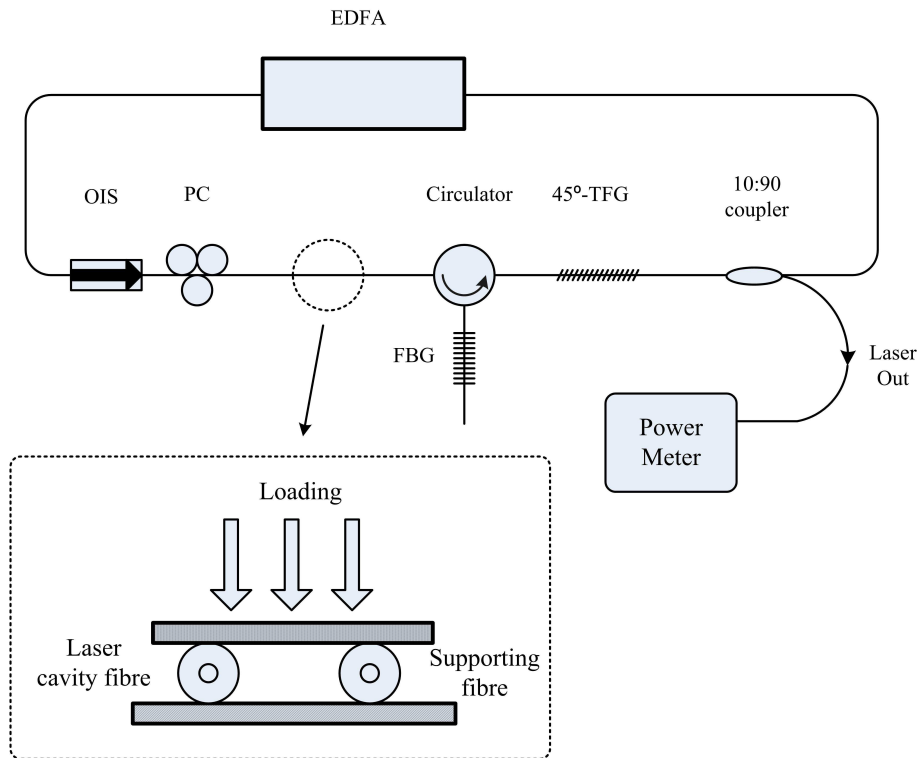
Figure 5.11 Schematic of the fibre laser loading sensor incorporating an intracavity 45°-TFG.

By switching on the EDFA, the laser gives out single wavelength output which is defined by the seeding FBG. The laser was optimised by adjusting the PC to maximise the output power. Figure 5.12 illustrates the typical output optical spectrum when no load is applied.
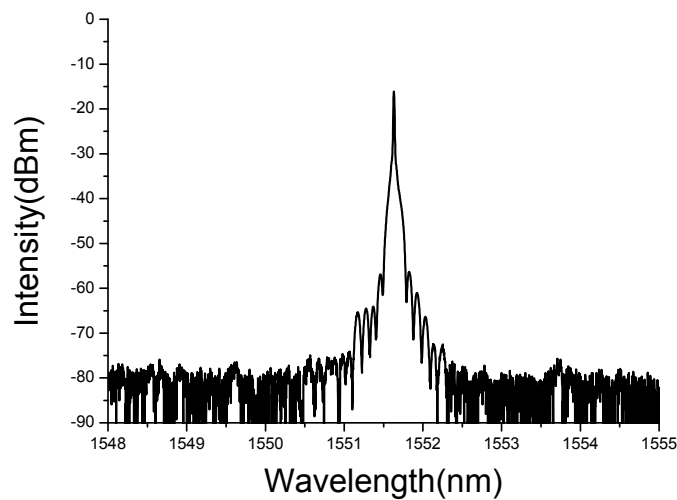
Figure 5.12 Typical output optical spectrum of the laser sensor.

When different loads were applied to the sensing fibre, the output power changes because of the alteration of polarisation state. The applied load has an increment of 500 g. The measured output optical power change against the loading weight is plotted in Figure 5.13. From Figure 5.13, it can be seen that the measured experimental results correspond well to the theoretical calculation using Equation 5.8.
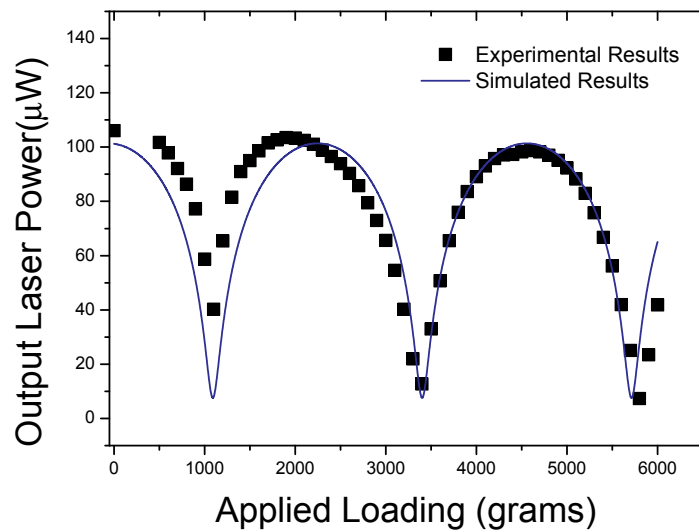
Figure 5.13 Measured output power change against loading weights

Obviously, owing to the long cavity length, this laser operates in multimode regime. Mode competition may induce instability to the measured results. A single mode operated laser may be exploited for future work. According to the principle of this laser based sensor, any type of polarisation change in the laser cavity will result in output power variation. This implies that this laser sensor is also capable of doing twist sensing. This will be investigated in future work.

5.6 Chapter Conclusions

In this chapter, the ex 45°-TFG based liquid level sensor has been demonstrated successfully. The sensor proved to be sensitive to low index liquid (i.e water) in comparison with conventional LPGs. Both the air- and the water-surrounded fast-axis modes show a linear water level sensitivity of ~ 13 %/mm, while the air- and water-

surrounded slow-axis modes exhibit a similar linear water level sensitivity of ~ 12 %/mm. The resulting water level sensitivity is more than twice of an LPG based level sensor. For the air-surrounded mode, the grating is only sensitive between 3 mm to 10 mm in a 12 mm long grating. For the water-surrounded mode, the measurement range is between 0 mm to 8 mm. Therefore, by observing both the water- and air-surrounded modes, the total water level measurement range can be 10 mm in a 12 mm long ex 45°-TFG. In general the measured liquid level is restricted to the length of the grating. The proposed liquid level sensor has smaller temperature cross responsivity compared to the LPG based sensor, temperature compensation scheme may not be necessary in some applications.

With the incorporation of the ex 45º-TFG in fibre laser system, the laser output is encoded with the twist or strain applied on the ex 45º-TFG, as it introduces loss in the laser cavity. By monitoring the build-up time change of the laser, the system can be developed into a low cost sensor system with time domain signal demodulation. Using an oscilloscope, a photodiode and a function generator, the implemented directional twist sensor obtains a sensitivity of ~412 μs/(rad/m) with a dynamic range from -150º to +150º. With 10 μs resolution from the oscilloscope, the twist sensor implies a measurement resolution of ~0.02 rad/m. While when the laser used as the strain sensor, it demonstrates a sensitivity of ~500 ns/με within the range of 1000 με and ~349 ns/με within the range of 500 με. This implies a measurement resolution of 2 με and 0.3 με individually depending on the oscilloscope resolution. As the sensitivity of the laser sensor system is related to the build-up time, further decreasing the pump power to lower level may increase the sensor sensitivity for both twist and strain sensing. However, longer time may result in tedious measurement procedure which is unwanted for some application. Optimisation of both types of sensing system will be for future investigation.

The utilisation of 45º-TFG in a fibre laser system and applying load to the laser cavity fibre, the laser output can then be encoded with the load. This type of laser sensor system can be at low cost and very robust. The experimental results correspond well with our theoretical simulation. The sensing principle also indicates that the proposed system may be able to perform twist sensing.

Chapter 6

Conclusions and Future Work

6.1 Fabrication an characterisation of 45º-TFGs and ex 45º-TFGs

This thesis details a systematic investigation on the fabrication, characterisation and application of a range of novel types of fibre gratings named 45º-TFGs and ex 45º-TFGs. For the first time, the fundamental limit on inscribing strong 45º-TFGs has been analysed, which is vitally important in guiding the design and fabrication condition for 45°-TFGs and ex 45°-TFGs with strong or controllable polarisation property. For the characterisation, both spectral and polarisation properties of 45º-TFGs in standard single mode fibres have been examined and analysed thoroughly. At 1.55 µm, three methods using single wavelength, broadband wavelength and a commercial toolkit have been developed to characterise 45º-TFGs. While at 1.06 µm, due to the availability of the equipment, only single wavelength measurement has been carried out. The most important results clearly show 45°-TFGs can be made with intrinsically high PDL, thus behaving as an in-fibre polariser. Thermal dependency is quite low for this type of grating from which PDL would decrease by a small amount when annealing at 80ºC. One major contribution is the observation of SBR from a 45º-TFG and a brief theoretical interpretation of this effect has been given. In addition, our evaluation on thermal response has shown the thermal responsivities of ~9.95 and ~9.47 pm/ºC for the ghost mode and SBR, respectively in the 45°-TFG. The SBR also shows high PDL which could serve as a polarising Bragg wavelength seed grating. The RI responses of 45º-TFGs have been investigated, showing that by applying proper RI coating, the performance of the 45º-TFG can be improved showing smooth PDL response curve.

Another contribution of this thesis is the initial exploration of inscription of the 45º-TFGs at 1.06 µm region, and more importantly for the first time, inscription of 45º-TFGs in PM fibres has been investigated. Two types of commercial PM fibres have been examined for 45º-TFGs inscription. In the commercial PM fibre, due to its low photosensitivity which is similar to standard telecom fibre, inscription of strong 45º-TFGs is usually not expected. Furthermore, another major difficulty in inscribing 45º-TFGs is the orientation of inscription owing to the intrinsic asymmetry of the PM fibres. With high UV radiation, reproducible 45º-TFGs with PDLs up to ~16 dB for

slow-axis inscription and ~8 dB for fast-axis inscription have been achieved successfully, while 45º-orientated inscription is generally difficult to obtain high PDLs. We have also developed a paraxial ray tracing analysis to explain the difference of achieved PDLs between fast- and slow-axis inscription.

As for ex 45º-TFGs, fabrication and characterisation have only been done with inscription in H_2 loaded SMF-28 fibres. This type of grating shows PM-LPG like behaviour. It exhibits polarisation mode splitting effect indicating strong birefringence has been induced through this excessively tilted grating structure. Compared to conventional FBGs and LPGs, the ex 45º-TFGs show significant lower thermal responsivites, which is an advantage as the thermal cross-sensitivity to some applications would be significant. For RI response, it is found that at longer wavelength, the coupled higher order cladding modes present higher sensitivities. It's RI response range is around 1.32 to 1.38. This range is complementary to the conventional LPGs, since the latter tend to be sensitive to RI close to that of the fibre.

6.2 Application of 45º-TFGs and ex 45º-TFGs

6.2.1 Application in fibre lasers

As a consequence of achieving successful inscription of 45º-TFGs and ex 45º-TFGs, various applications with these novel grating structures have been explored. One major domain is the application of both types of grating in fibre lasers. Utilisation of a single 45º-TFG in a fibre ring laser cavity has shown great improvement of DOP (~ 99.9 %) in conventional fibre ring laser configuration, giving almost single polarisation output. Without the integration of the 45°-TFG intracavity polariser, the output of the conventional fibre laser is nearly randomly polarised as the measured DOP is only ~ 22.6 %. This single polarisation laser also showed stable performance of the high DOP output with a variation of ~ 0.2 %. Because an external FBG was used as a wavelength seed, it was possible to tune the output laser wavelength by applying strain to the FBG, which has been demonstrated. A lower slope efficiency is

expected compared to the conventional fibre ring laser structure as some loss was induced by the integration of the 45°-TFG. An improved version of this laser is the utilisation of the SBR of the 45°-TFG. Using a single 45°-TFG with SBR, stable single wavelength, single polarisation fibre ring laser can be constructed. The output light showed high DOP (~ 99.9 %). With similar capability of tuning, this laser has an improved slope efficiency of ~13.9% which is comparable to standard fibre ring laser using a single FBG for seeding.

By combining the polarisation and spectral properties of both 45°-TFG and ex 45°-TFG, single polarisation and multiwavelength switchable fibre lasers have also been demonstrated. Initially, a dual wavelength fibre laser using one 45°-TFG and one ex 45°-TFG was implemented. This laser showed the capability of dual wavelength switching. The stable output also gave high DOP (~99.9%). A further extended version of fibre laser using one 45°-TFG and two ex 45°-TFGs was constructed and able to support single polarisation and switchable quadruple wavelength output with high DOP performance. As mentioned above, due to the intrinsic loss properties of the gratings, high slope efficiency was not expected for the multiwavelength fibre lasers.

Another major contribution of this thesis is the novel application of 45°-TFG in the area of nonlinear photonics. For the first time, a 45°-TFG was used in a fibre ring laser cavity to facilitate NPR based mode locking at 1.55 µm region. By properly adjusting the intracavity polarisation controllers, stable soliton pulse solution output was achieved. At 1553 nm, the laser could give output pulses with ~600 fs pulse duration. The laser showed a repetition rate of ~10.34 MHz with 12 mW output power. The output pulse had a FWHM of ~9 nm while the pulse energy was estimated to be ~1 nJ. A high time bandwidth product (~0.6) indicated the output pulse was chirped for which properly design of the fibre laser could give out transform limited pulses. The mode locked laser also offered a certain degree of tunability from 1548 nm to 1562 nm when adjusting the intracavity polarisation controllers. Overall, this laser represents a solution of robust design, all fibre format and compact configuration of a mode locking ultra-short pulse fibre laser.

6.2.2 Application in fibre sensors

Based on the PDL properties, both 45º-TFGs and ex 45º-TFGs have been further developed into various sensor systems. An ex 45º-TFG has been developed into a liquid level sensor which provides sensing capability in lower RI range ($\approx$ 1.33). This compensates the drawback of LPG based level sensor from which only RI >1.4 can be detected more effectively. The ex 45º-TFG based liquid level sensor also shows sensitivity of more than twice of an LPG based level sensor. Furthermore, the ex 45º-TFG based level sensor exhibited much lower thermal cross sensitivity compared to an LPG. However, the sensing range was limited by the length of the ex 45º-TFG.

By incorporating the ex 45º-TFGs into a fibre laser cavity, fibre laser based twist and strain sensors have been demonstrated. Differently to the conventional optically resolved method, this laser based sensor used time domain signal demodulation technique to achieve low cost interrogation with high sensitivity. For the twist sensor, it showed a sensitivity of ~412 μs/(rad/m) within ±140º dynamic range. With the available equipment, this corresponds to a measurement sensitivity of ~0.02 rad/m. It was also demonstrated that if the system was preset at a defined position such as ±80º, the sensor could perform direction identification as well as twist measurement. For strain measurement, the sensor showed a linear responsivity of ~500 ns/με from 0 με to 1000 με when the proper pump level was chosen. This corresponds to a measurement resolution of ~2 με. Because a modulated pump signal was using in the laser sensor, the sensitivity of the sensors would also have dependency on the modulation frequency and upper and lower level of the pump power.

Finally, the 45º-TFG based single polarisation fibre laser has been applied as an all fibre loading sensor system. It has been shown that applied loading in the laser cavity would change the birefringence of the cavity fibre, therefore, the polarisation of propagating light. It thus modulates the cavity loss by means of alternating the intracavity polarisation. The experimental results corresponded well to our theoretical calculation.

6.3 Suggested Future Work

The work in this thesis suggests many interesting directions to study in the future. In this section, a selected number of topics are briefly discussed.

6.3.1 45º-TFG based in-fibre Lyot filter

Optical filters are important in various applications. Clearly, conventional FBGs and LPGs have been widely applied as optical filters. So far, TFGs exhibiting strong coupled cladding or radiation modes behaviour have not found many applications as optical filters. It is of interest to explore TFGs for novel filtering functions.

Lyot filter is a kind of optical filter consisting of a series of birefringent plates and polarisers. The light transmitting in a birefrigent plate can be regarded as containing two orthogonal polarisation components which undergo a different phase delay. This phase delay of the two polarisation components has wavelength dependency. Therefore, the transmitted optical power is wavelength dependent.

As the PM fibres are ideal in-fibre birefringent plates and 45º-TFGs are in-fibre polarisers, an all fibre Lyot filter made with a PM fibre sandwiched between a pair of 45º-TFGs could be achieved. By properly choosing the birefringence i.e. length of PM fibre between the two 45º-TFGs, an all fibre Lyod filter with various filter bandwidths can be achieved. The proposed all fibre Lyod filter could offer compact, robust design in various applications such as signal processing and fibre lasers.

6.3.2 Detailed investigation of SBR in 45º-TFG and its application in fibre sensors

The observation of SBR of 45º-TFGs opens a new direction in the field of tilted fibre gratings. Although this thesis has presented some of the initial explanation and

primary results of this effect, further investigation will be of interest. Detailed information such as inscription condition for controllable SBR should be further studied. Moreover, SBR in TFGs with tilted structure at other angles (not at 45°) may be investigated in the future in order to understand this effect and explore its applications.

As in this thesis, only brief characterisation has been done of the SBR phenomenon. However, it is already found that this SBR exhibits some similar properties to the conventional FBG. Due to its unique polarising function, this may serve as a sensing element. Combined with conventional FBG or/and LPG, a comprehensive sensing system with multi-function may be achieved.

6.3.3 All normal dispersion high energy fibre laser incorporating a 45°-TFG at 1.06 µm

Fibre laser is one of the most rapidly developing areas of research. High energy fibre lasers are always of great interest. Recently, all normal dispersion fibre lasers which give out high energy mode locked pulses have attracted a lot of attentions [198-199]. Since the implementation of 45°-TFG in mode locked Erbium doped fibre soliton laser has been successfully presented in this thesis, it will be interesting to see the behaviour of such gratings under high energy circumstance. Currently, all normal dispersion fibre lasers all use bulk optics which undoubtedly increases the difficulties of optics alignment and induce excess insertion loss. We believe that the robustness, compactness and all-fibre format of the 45°-TFGs will make contribution to the new development of fibre lasers.

More additions to this section are possible. TFGs with unique cladding mode and polarisation features begin to emerge in the fibre sensors and lasers domain with superior performances. Moreover, the nonlinear properties of TFGs may identify them as novel platform for nonlinear dynamics research.

Publication list

Publication from results reported in this thesis

Journal papers

1. **Chengbo Mou**, Pouneh Saffari, Hongyan Fu, Kaiming Zhou, Lin Zhang, and Ian Bennion, "Single- and dual-wavelength switchable erbium-doped fiber ring laser based on intracavity polarization selective tilted fiber gratings ", *Applied Optics*, Vol.48, No.18, 3455-3459, 2009

2. **Chengbo Mou,** Kaiming Zhou, Lin Zhang and Ian Bennion, "Characterization of 45-tilted fiber grating and its polarization function in fiber ring laser", *Journal of the Optical Society of America* **B** V.26 No.10, 1905-1911, 2009

3. **Chengbo Mou**, Hua Wang, Brandon Bale, Kaiming Zhou, Lin Zhang and Ian Bennion,"All-fiber passively mode-locked femtosecond laser using a 45°-tilted fiber grating polarization element", *Optics Express* V.18, Issue 19, pp.18906-18911 (2010)

Conference papers

1. **Chengbo Mou**, Xianfeng Chen, Kaiming Zhou, Lin Zhang, Ian Bennion, Shenggui Fu, and Xiaoyi Dong "Realisation of Single Polarisation State of Fibre Ring Laser by Utilising Intracavity 45° Tilted Fibre Bragg Grating", **poster presentation**, *Bragg Gratings, Photosensitivity and Poling in Glass Waveguides (BGPP) 2007*, September 2-6, Quebec City, Quebec, Canada

2. **Chengbo Mou**, Kaiming Zhou, Lin Zhang, and Ian Bennion, "Thermal Insensitive Optical Liquid Level Sensor Based on Excessively Tilted Fibre Bragg Grating", **Oral Presentation**, *Asia Optical Fiber Communication and Optoelectronic Exposition and Conference (AOE)*, October 30- November 2, Shanghai, China.

3. **Chengbo Mou**, Kaiming Zhou, Rui Suo, Lin Zhang, and Ian Bennion, "Fibre Laser torsion sensor system using an excessively tilted fibre grating and low-cost time domain demodulation", **poster presentation**, *20th International Conference on Optical Fibre Sensors (OFS-20)*, October 5-9,2009, Edinburgh, UK

4. Pouneh Saffari, **Chengbo Mou**, Hongyan Fu, Lin Zhang and Ian Bennion, "Multi-wavelength switchable fibre ring laser based on polarisation selective tilted fibre gratings capable of strain and temperature sesning", **poster presentation**, *SPIE Europe Optics and Optoelectronics*, April 20-23,2009, Prague, Czech Republic. Proceddings Vol.7356.

5. **Chengbo Mou**, Hua Wang, Brandon Bale, Kaiming Zhou, Lin Zhang, Sergei Turitsyn and Ian Bennion, "All Fibre Femtosecond Pulse Generation Using an Intracavity 45°-Tilted Fibre Grating", **Oral presentation**, *Bragg Gratings, Photosensitivity and Poling in Glass Waveguides (BGPP2010)*, JUN21-24,2010, Karlsruhe, Germany

6. **Chengbo Mou**, Rui Suo, Kaiming Zhou, Lin Zhang, and Ian Bennion, "2nd Order Bragg Rasonance Generated In A 45° Tilted Fiber Grating And Its Application In A Fiber Laser", **Oral presentation**, *Bragg Gratings, Photosensitivity and Poling in Glass Waveguides (BGPP2010)*, JUN 21-24,2010, Karlsruhe, Germany

Other publications

Journal Papers

1. **Chengbo Mou**, Pouneh Saffari, Dezhi Li, Kaiming Zhou, Lin Zhang, Rupert Soar and Ian Bennion, "Smart structure sensors based on embedded fibre Bragg grating arrays in aluminium alloy matrix by ultrasonic consolidation", *Measurement Science and Technology*,20, 034013,2009

2. Hongyan Fu, Kaiming Zhou, Pouneh Saffari, **Chengbo Mou**, Lin Zhang, Sailing He, and Ian Bennion, "Microchanneled Chirped Fiber Bragg Grating Formed by Femtosecond Laser-Aided Chemical Etching for Refractive Index and Temperature Measurements", *IEEE Photonics Technology Letters*, Vol. 20, No. 19, 1609-1611, 2008.

3. Hongyan Fu, Wei Zhang, **Chengbo Mou**, Xuewen Shu, Lin Zhang, Sailing He, and Ian Bennion, "High-Frequency Fiber Bragg Grating Sensing Interrogation System Using Sagnac-Loop-Based Microwave Photonic Filtering", *IEEE Photonics Technology Letters*, VOL. 21, NO. 8, APRIL 15, 519-521, 2009

4. T.Allsop, R.Neal,**Chengbo Mou**, P.Brown, S.Saied, S.Rehman, K.Kalli, D.J.Webb, J.Sullivan, D.Mapps, and I.Bennion, "Exploitation of multilayer coatings for infrared surface plasmon resonance fiber sensors", *Applied Optics*, V.48, No.2, 276-286,2009

5. T.Allsop, R.Neal, **Chengbo Mou**, P.Brown, S.Rehman, K.Kalli, D.J.Webb, D.Mapps, I.Bennion, "Multilayered Coated Infra-red Surface Plasmon Resonance Fibre Sensors for Aqueous Chemical Sensing", *Fiber Optical Technology* V.15 ,477-482,2009

6. **Chengbo Mou**, Kaiming Zhou, Edward Davies, Lin Zhang and Ian Bennion, "Fiber Laser Incorporating an Intracavity Micro-channel for Refractive Index and Temperature Sensing", *IEEE Photonic Technologies Letters* V.21, No.20, 1559-1561, 2009

7. Kaiming Zhou, David J.Webb, **Chengbo Mou**, Mark Farries, Neil Hayes, and Ian Bennion, "Optical Fiber Cavity Ring Down Measurement of Refrative

Index With a Microchannel Drilled by Femtosecond Laser", *IEEE Photonic Technologies Letters* V.21, No.22, 1653-1655,2009

8. Tom Allsop, R Neal, E M Davies, **Chengbo Mou**, P Bond, S Rehman, K Kalli, D J Webb, P Calverhouse and I Bennion, "Low refractive index gas sensing using a surface plasmon resonance fibre device", *Measurement Science and Technology*, V.21, 094029,2010

Conference Papers

1. **Chengbo Mou**, Pouneh Saffari, Dezhi Li, Kaiming Zhou, Lin Zhang, Rupert Soar and Ian Bennion, "Embedded fibre Bragg grating array sensors in aluminium alloy matrix by ultrasonic consolidation", **poster presentation**, *19th International Conference on Optical Fibre Sensors (OFS-19)*, April 14-18,2008, Perth, Western Australia.

2. Hongyan Fu, Kaiming Zhou, Pouneh Saffari, **Chengbo Mou**, Lin Zhang, Sailing He, and Ian Bennion, "Microchannelled Chirped Fibre Bragg Grating Based Refractive Index Sensor Formed by Femto-Second Laser Processing and HF-etching", **Oral presentation**, *ECOC 2008*, 21st-25th, Sept., Brussels, Belgium.

3. Hongyan Fu, Wei Zhang, **Chengbo Mou**, Xuewen Shu, Lin Zhang, Sailing He and Ian Bennion, "High Frequency Sensing Interrogation System Using Fiber Bragg Grating Based Microwave Photonic Filtering", **poster presentation**, *OFC 2009*, San Diego, March 22-26, 2009.

4. **Chengbo Mou,** Kaiming Zhou, Edward Davies, Lin Zhang and Ian Bennion, "Fibre Laser Using a Microchannel Based Loss Tuning Element for Refractive Index Sensing", **Oral presentation**, *20th International Conference on Optical Fibre Sensors (OFS-20)*, October 5-9,2009, Edinburgh, UK

5. T.Allsop, R.Neal, **Chengbo Mou**, P.Brown, S.Rehman, K.Kalli, D.J.Webb, D.Mapps, I.Bennion, "Multilayed Coated Infra-red Surface Plasmon Resonance Fibre Sensors for Chemical Sensing", **Oral Presentation**, *CLEO 2009*, Munich, Germany

6. Edward Davies, Pouneh Saffari, **Chengbo Mou**, Kaiming Zhou, Rui Suo, Lin Zhang, and Ian Bennion, "Refractive index sensitivity enhancement of 81° tilted Bragg gratings by cladding etching", **poster presentation**, *20th International Conference on Optical Fibre Sensors (OFS-20)*, October 5-9,2009, Edinburgh, UK

7. Kaiming Zhou, David Webb, **Chengbo Mou**, Mark Farries, Nail Hayes and Ian Bennion, "Optical fibre cavity ring down measurement of refractive index with a microchannel drilled by femtosecond laser", **poster presentation**, *20th International Conference on Optical Fibre Sensors (OFS-20)*, October 5-9,2009, Edinburgh, UK

8. Pouneh Saffari, **Chengbo Mou**, Lin Zhang and Ian Bennion, "Single Polarisation Output Of Erbium-doped Fibre Ring Laser Utilising A Small Tilted Fibre Grating Structure" **poster presentation**, *Bragg Gratings, Photosensitivity and Poling in Glass Waveguides (BGPP2010)*, JUN21-24,2010, Karlsruhe, Germany

References

[1]   K. O. Hill, *et al.*, "Photosensitivity in Optical Fiber Waveguides - Application to Reflection Filter Fabrication," *Applied Physics Letters,* vol. 32, pp. 647-649, 1978.

[2]   K. S. Feder, *et al.*, "In-fiber spectrometer using tilted fiber gratings," *Ieee Photonics Technology Letters,* vol. 15, pp. 933-935, Jul 2003.

[3]   P. Westbrook, *et al.*, "Application of fiber Bragg grating filter/tap module to a wavelength-locked low-chirp directly-modulated 10 Gb/s Rz transmitter," in *Optical Fiber Communication Conference*, Anaheim, California, USA, 2002.

[4]   R. Kashyap, *et al.*, "Wide-Band Gain Flattened Erbium Fiber Amplifier Using a Photosensitive Fiber Blazed Grating," *Electronics Letters,* vol. 29, pp. 154-156, Jan 21 1993.

[5]   C. Jauregui, *et al.*, "Interrogation of interferometric sensors with a tilted fiber Bragg grating," *Optics Express,* vol. 12, pp. 5646-5654, Nov 15 2004.

[6]   C. Jauregui, *et al.*, "Interrogation unit for fiber Bragg grating sensors that uses a slanted fiber grating," *Optics Letters,* vol. 29, pp. 676-678, Apr 1 2004.

[7]   Y. Liu, *et al.*, "Fabricating fibre edge filters with arbitrary spectral response based on tilted chirped grating structures," *Measurement Science & Technology,* vol. 10, pp. L1-L3, Jan 1999.

[8]   A. G. Simpson, *et al.*, "Optical sensor interrogation with a blazed fiber Bragg grating and a charge-coupled device linear array," *Applied Optics,* vol. 43, pp. 33-40, Jan 1 2004.

[9]   J. Peupelmann, *et al.*, "Fibre-polarimeter based on grating taps," *Electronics Letters,* vol. 38, pp. 1248-1250, Oct 10 2002.

[10]   P. S. Westbrook*, et al.*, "In-line polarimeter using blazed fiber gratings," *Ieee Photonics Technology Letters,* vol. 12, pp. 1352-1354, Oct 2000.

[11]   S. J. Mihailov*, et al.*, "UV-induced polarisation-dependent loss (PDL) in tilted fibre Bragg gratings: application of a PDL equaliser," *Iee Proceedings-Optoelectronics,* vol. 149, pp. 211-216, Oct-Dec 2002.

[12]   S. J. Mihailov*, et al.*, "Fabrication of tilted fibre-grating polarisation-dependent loss equaliser," *Electronics Letters,* vol. 37, pp. 284-286, Mar 1 2001.

[13]   K. M. Zhou*, et al.*, "High extinction ratio in-fiber polarizers based on 45 degrees tilted fiber Bragg gratings," *Optics Letters,* vol. 30, pp. 1285-1287, Jun 1 2005.

[14]   X. Chen*, et al.*, "In-fiber twist sensor based on a fiber Bragg grating with 81 degrees tilted structure," *Ieee Photonics Technology Letters,* vol. 18, pp. 2596-2598, Nov-Dec 2006.

[15]   K. M. Zhou*, et al.*, "Optic sensors of high refractive-index responsivity and low thermal cross sensitivity that use fiber Bragg gratings of > 80 degrees tilted structures," *Optics Letters,* vol. 31, pp. 1193-1195, May 2006.

[16]   P. S. Russell*, et al.*, "Frequency Doubling, Absorption and Grating Formation in Glass-Fibers - Effective Defects or Defective Effects," *Fiber Laser Sources and Amplifiers Ii,* vol. 1373, pp. 126-139, 1991.

[17]   L. J. Poyntzwright*, et al.*, "Nonlinear Transmission and Color-Center Dynamics in Germanosilicate Fibers at 420-540 Nm," *Optics Letters,* vol. 13, pp. 1023-1025, Nov 1988.

[18]   D. P. Hand and P. S. Russell, "Solitary Thermal-Shock Waves and Optical-Damage in Optical Fibers - the Fiber Fuse," *Optics Letters,* vol. 13, pp. 767-769, Sep 1988.

[19]   D. P. Hand and P. S. Russell, "Photoinduced Refractive-Index Changes in Germanosilicate Fibers," *Optics Letters,* vol. 15, pp. 102-104, Jan 15 1990.

[20]   R. Weeks, "Paramagnetic resonance of lattice defects in irradiated quartz," *Journal of Applied Physics,* vol. 27, pp. 1376-1381, 1956.

[21]   C. Nelson and R. Weeks, "Trapped Electrons in Irradiated Quartz and Silica: I, Optical Absorption," *Journal of the American Ceramic Society,* vol. 43, pp. 396-399, 1960.

[22]   D. L. Griscom, "Defect Structure of Glasses - Some Outstanding Questions in Regard to Vitreous Silica," *Journal of Non-Crystalline Solids,* vol. 73, pp. 51-77, 1985.

[23]   P. Kaiser, "Drawing-Induced Coloration in Vitreous Silica Fibers," *Journal of the Optical Society of America,* vol. 64, pp. 475-481, 1974.

[24]   E. J. Friebele*, et al.*, "Defect Centers in a Germanium-Doped Silica-Core Optical Fiber," *Journal of Applied Physics,* vol. 45, pp. 3424-3428, 1974.

[25]   E. Friebele and D. Griscom, "Color Centers in Glass Optical Fiber Waveguides," *Defects in Glasses; Boston, Massachusetts; USA,* pp. 319-331, 1985.

[26]   H. Hosono*, et al.*, "Correlation between Ge E' centers and optical absorption bands in SiO2:GeO2 glasses," *Japanese Journal of Applied Physics Part 2-Letters,* vol. 35, pp. L234-L236, Feb 15 1996.

[27]   M. J. Yuen, "Ultraviolet-Absorption Studies of Germanium Silicate-Glasses," *Applied Optics,* vol. 21, pp. 136-140, 1982.

[28]   N. M. Lawandy, "Light-Induced Transport and Delocalization in Transparent Amorphous Systems," *Optics Communications,* vol. 74, pp. 180-184, Dec 15 1989.

[29] A. Miotello and R. Kelly, "Laser Irradiation Effects in Si+-Implanted Sio2," *Nuclear Instruments & Methods in Physics Research Section B-Beam Interactions with Materials and Atoms,* vol. 65, pp. 217-222, Mar 1992.

[30] A. E. Attard, "Fermi Level Shift in Bi12sio20 Via Photon-Induced Trap Level Occupation," *Journal of Applied Physics,* vol. 71, pp. 933-937, Jan 15 1992.

[31] D. Wong*, et al.*, "Stress-Birefringence Reduction in Elliptic-Core Fibers under Ultraviolet-Irradiation," *Optics Letters,* vol. 17, pp. 1773-1775, Dec 15 1992.

[32] D. L. Williams*, et al.*, "Photosensitive Index Changes in Germania Doped Silica Glass-Fibers and Wave-Guides," *Photosensitivity and Self-Organization in Optical Fibers and Waveguides,* vol. 2044, pp. 55-68, 1993.

[33] C. Fiori and R. A. B. Devine, "Evidence for a Wide Continuum of Polymorphs in a-Sio2," *Physical Review B,* vol. 33, pp. 2972-2974, Feb 15 1986.

[34] D. P. Hand, "Periodic structures in optical fibres. ," Ph.D Thesis, University of Southampton, 1990.

[35] K. D. Simmons*, et al.*, "Correlation of Defect Centers with a Wavelength-Dependent Photosensitive Response in Germania-Doped Silica Optical Fibers," *Optics Letters,* vol. 16, pp. 141-143, Feb 1 1991.

[36] D. L. Williams*, et al.*, "Direct Observation of Uv Induced Bleaching of 240-Nm Absorption-Band in Photosensitive Germanosilicate Glass-Fibers," *Electronics Letters,* vol. 28, pp. 369-371, Feb 13 1992.

[37] R. M. Atkins and V. Mizrahi, "Observations of Changes in Uv Absorption-Bands of Singlemode Germanosilicate Core Optical Fibers on Writing and Thermally Erasing Refractive-Index Gratings," *Electronics Letters,* vol. 28, pp. 1743-1744, Aug 27 1992.

[38]   R. M. Atkins*, et al.*, "248 Nm Induced Vacuum Uv Spectral Changes in Optical-Fiber Preform Cores - Support for a Color Center Model of Photosensitivity," *Electronics Letters,* vol. 29, pp. 385-387, Feb 18 1993.

[39]   T. E. Tsai*, et al.*, "Thermal-Stability of Photoinduced Gratings and Paramagnetic Centers in Ge-Doped and Ge/P-Doped Silica Optical Fibers," *Optics Letters,* vol. 18, pp. 935-937, Jun 15 1993.

[40]   L. Dong*, et al.*, "Photoinduced Absorption Change in Germanosilicate Preforms - Evidence for the Color-Center Model of Photosensitivity," *Applied Optics,* vol. 34, pp. 3436-3440, Jun 20 1995.

[41]   T. E. Tsai*, et al.*, "Index structure of fiber Bragg gratings in Ge-SiO2 fibers," *Optics Letters,* vol. 22, pp. 224-226, Feb 15 1997.

[42]   B. Leconte*, et al.*, "Analysis of color-center-related contribution to Bragg grating formation in Ge:SiO2 fiber based on a local Kramers-Kronig transformation of excess loss spectra," *Applied Optics,* vol. 36, pp. 5923-5930, Aug 20 1997.

[43]   W. X. Xie*, et al.*, "Experimental-Evidence of 2 Types of Photorefractive Effects Occurring during Photoinscriptions of Bragg Gratings within Germanosilicate Fibers," *Optics Communications,* vol. 104, pp. 185-195, Dec 15 1993.

[44]   P. Cordier*, et al.*, "Tem Characterization of Structural-Changes in Glass Associated to Bragg Grating Inscription in a Germanosilicate Optical-Fiber Preform," *Optics Communications,* vol. 111, pp. 269-275, Oct 1 1994.

[45]   P. Niay*, et al.*, "Behavior of Spectral Transmissions of Bragg Gratings Written in Germania-Doped Fibers - Writing and Erasing Experiments Using Pulsed or Cw Uv Exposure," *Optics Communications,* vol. 113, pp. 176-192, Dec 15 1994.

[46] C. Fiori and R. Devine, "Ultraviolet irradiation induced compaction and photoetching in amorphous, thermal SiO2," in *Material Research Society Symposium*, 1986, pp. 187-195.

[47] M. Rothschild*, et al.*, "Effects of Excimer Laser Irradiation on the Transmission, Index of Refraction, and Density of Ultraviolet Grade Fused-Silica," *Applied Physics Letters,* vol. 55, pp. 1276-1278, Sep 25 1989.

[48] D. C. Allan*, et al.*, "193-nm excimer-laser-induced densification of fused silica," *Optics Letters,* vol. 21, pp. 1960-1962, Dec 15 1996.

[49] B. Poumellec*, et al.*, "Uv Induced Densification during Bragg Grating Inscription in Ge-Sio2 Preforms - Interferometric Microscopy Investigations," *Optical Materials,* vol. 4, pp. 404-409, Jan 1995.

[50] B. Poumellec*, et al.*, "Uv Induced Densification during Bragg Grating Inscription Ge-Sio2 Preforms," *Optical Materials,* vol. 4, pp. 441-449, Mar 1995.

[51] P. Cordier*, et al.*, "Evidence by transmission electron microscopy of densification associated to Bragg grating photoimprinting in germanosilicate optical fibers," *Applied Physics Letters,* vol. 70, pp. 1204-1206, Mar 10 1997.

[52] P. Y. Fonjallaz*, et al.*, "Tension Increase Correlated to Refractive-Index Change in Fibers Containing Uv-Written Bragg Gratings," *Optics Letters,* vol. 20, pp. 1346-1348, Jun 1 1995.

[53] H. G. Limberger*, et al.*, "Compaction- and photoelastic-induced index changes in fiber Bragg gratings," *Applied Physics Letters,* vol. 68, pp. 3069-3071, May 27 1996.

[54] M. Douay*, et al.*, "Densification involved in the UV-based photosensitivity of silica glasses and optical fibers," *Journal of Lightwave Technology,* vol. 15, pp. 1329-1342, Aug 1997.

[55]   M. Sceats*, et al.*, "Photolytic index changes in optical fibers," *Annual Review of Materials Science,* vol. 23, pp. 381-410, 1993.

[56]   P. J. Lemaire*, et al.*, "High-Pressure H-2 Loading as a Technique for Achieving Ultrahigh Uv Photosensitivity and Thermal Sensitivity in Geo2 Doped Optical Fibers," *Electronics Letters,* vol. 29, pp. 1191-1193, Jun 24 1993.

[57]   D. L. Williams*, et al.*, "Enhanced Uv Photosensitivity in Boron Codoped Germanosilicate Fibers," *Electronics Letters,* vol. 29, pp. 45-47, Jan 7 1993.

[58]   F. Bilodeau*, et al.*, "Photosensitization of Optical-Fiber and Silica-on-Silicon Silica Wave-Guides," *Optics Letters,* vol. 18, pp. 953-955, Jun 15 1993.

[59]   G. Brambilla and V. Pruneri, "Enhanced photosensitivity in silicate optical fibers by thermal treatment," *Applied Physics Letters,* vol. 90, Mar 12 2007.

[60]   P. J. Lemaire*, et al.*, "Thermally Enhanced Ultraviolet Photosensitivity in Geo2 and P2o5 Doped Optical Fibers," *Applied Physics Letters,* vol. 66, pp. 2034-2036, Apr 17 1995.

[61]   K. Noguchi*, et al.*, "Loss Increase for Optical Fibers Exposed to Hydrogen Atmosphere," *Journal of Lightwave Technology,* vol. 3, pp. 236-243, 1985.

[62]   R. M. Atkins*, et al.*, "Mechanisms of Enhanced Uv Photosensitivity Via Hydrogen Loading in Germanosilicate Glasses," *Electronics Letters,* vol. 29, pp. 1234-1235, Jul 8 1993.

[63]   R. M. Atkins and P. J. Lemaire, "Effects of Elevated-Temperature Hydrogen Exposure on Short-Wavelength Optical Losses and Defect Concentrations in Germanosilicate Optical Fibers," *Journal of Applied Physics,* vol. 72, pp. 344-348, Jul 15 1992.

[64]   J. Stone, "Interactions of Hydrogen and Deuterium with Silica Optical Fibers - a Review," *Journal of Lightwave Technology,* vol. 5, pp. 712-733, May 1987.

[65]   V. Mizrahi, *et al.*, "Ultraviolet-Laser Fabrication of Ultrastrong Optical-Fiber Gratings and of Germania-Doped Channel Wave-Guides," *Applied Physics Letters,* vol. 63, pp. 1727-1729, Sep 27 1993.

[66]   I. Camlibel, *et al.*, "Optical Aging Characteristics of Borosilicate Clad Fused Silica Core Fiber Optical-Waveguides," *Applied Physics Letters,* vol. 26, pp. 185-187, 1975.

[67]   D. Kato, "Fused-silica-core glass fiber as a low-loss optical waveguide," *Applied Physics Letters,* vol. 22, pp. 3-4, 1973.

[68]   L. Cognolato, "Chemical-vapor-deposition for optical-fiber technolgoy," *Journal De Physique Iv,* vol. 5, pp. 975-987, Jun 1995.

[69]   M. N. S. Bonino, E. Riccardi, and M. Schiano, "Measurement of polarization properties of chirped fiber gratings," in *Optical Fiber Measurement Conference (OFMC 97)*, Teddington, UK, 1997, pp. 10-13.

[70]   S. R. Baker, *et al.*, "Thermal decay of fiber Bragg gratings written in boron and germanium codoped silica fiber," *Journal of Lightwave Technology,* vol. 15, pp. 1470-1477, Aug 1997.

[71]   L. Dong, *et al.*, "Enhanced Photosensitivity in Tin-Codoped Germanosilicate Optical Fibers," *Ieee Photonics Technology Letters,* vol. 7, pp. 1048-1050, Sep 1995.

[72]   K. Oh, *et al.*, "Ultraviolet photosensitive response in an antimony-doped optical fiber," *Optics Letters,* vol. 27, pp. 488-490, Apr 1 2002.

[73]   A. Yariv, "Coupled-Mode Theory for Guided-Wave Optics," *IEEE Journal of Quantum Electronics,* vol. Qe 9, pp. 919-933, 1973.

[74]   A. Yariv, *et al.*, *Photonics : optical electronics in modern communications*, 6th ed. ed. Oxford: Oxford University Press, 2007.

[75]   T. Erdogan, "Fiber grating spectra," *Journal of Lightwave Technology,* vol. 15, pp. 1277-1294, Aug 1997.

[76]   D. Marcuse, *Theory of dielectric optical waveguides*, 2nd ed. ed.: Academic, 1991.

[77]   M. Yamada and K. Sakuda, "Analysis of Almost-Periodic Distributed Feedback Slab Wave-Guides Via a Fundamental Matrix Approach," *Applied Optics,* vol. 26, pp. 3474-3478, Aug 15 1987.

[78]   L. Weller-Brophy and D. Hall, "Analysis of waveguide gratings: application of Rouard's method," *Journal of the Optical Society of America A,* vol. 2, pp. 863-871, 1985.

[79]   M. Rouard, "Etudes des propriétés optiques des lames métalliques très minces," *Ann. Phys.(Paris) Ser. II,* vol. 7, pp. 291-384, 1937.

[80]   P. S. Russell, "Bloch Wave Analysis of Dispersion and Pulse-Propagation in Pure Distributed Feedback Structures," *Journal of Modern Optics,* vol. 38, pp. 1599-1619, Aug 1991.

[81]   O. Xu*, et al.*, "Analysis of spectral characteristics for reflective tilted fiber gratings of uniform periods," *Optics Communications,* vol. 281, pp. 3990-3995, Aug 2008.

[82]   O. Xu*, et al.*, "Theoretical analysis of polarization properties for tilted fiber Bragg gratings," *Science China-Information Sciences,* vol. 53, pp. 390-397, Feb 10 2010.

[83]   S. H. Lu*, et al.*, "Analysis of coupling from core mode to counter-propagating radiation modes in tilted fiber Bragg gratings," *Science China-Information Sciences,* vol. 53, pp. 1078-1088, May 2010.

[84]   Y. F. Li*, et al.*, "Volume current method for analysis of tilted fiber gratings," *Journal of Lightwave Technology,* vol. 19, pp. 1580-1591, Oct 2001.

[85]   B. S. Kawasaki, *et al.*, "Narrow-Band Bragg Reflectors in Optical Fibers," *Optics Letters,* vol. 3, pp. 66-68, 1978.

[86]   G. Meltz, *et al.*, "Formation of Bragg Gratings in Optical Fibers by a Transverse Holographic Method," *Optics Letters,* vol. 14, pp. 823-825, Aug 1 1989.

[87]   D. Z. Anderson, *et al.*, "Production of in-Fiber Gratings Using a Diffractive Optical-Element," *Electronics Letters,* vol. 29, pp. 566-568, Mar 18 1993.

[88]   K. O. Hill, *et al.*, "Bragg Gratings Fabricated in Monomode Photosensitive Optical-Fiber by Uv Exposure through a Phase Mask (Vol 62, Pg 1035, 1993)," *Applied Physics Letters,* vol. 63, pp. 424-424, Jul 19 1993.

[89]   B. Malo, *et al.*, "Point-by-point fabrication of micro-Bragg gratings in photosensitive fibre using single excimer pulse refractive-index modification techniques," *Electronics Letters,* vol. 29, pp. 1668-1669, Sep 1993.

[90]   R. Kashyap, *et al.*, "All-fibre narrowband reflection gratings at 1500 nm," *Electronics Letters,* vol. 26, pp. 730-732, 1990.

[91]   B. Eggleton, *et al.*, "Experimental demonstration of compression of dispersed optical pulses by reflection from self-chirped optical fiber Bragg gratings," *Optics Letters,* vol. 19, pp. 877-879, 1994.

[92]   H. G. Limberger, *et al.*, "Olcr Characterization of Efficient Bragg Gratings in Optical-Fiber," *Photosensitivity and Self-Organization in Optical Fibers and Waveguides,* vol. 2044, pp. 272-283, 1993.

[93]   K. C. Byron, *et al.*, "Fabrication of Chirped Bragg Gratings in Photosensitive Fiber," *Electronics Letters,* vol. 29, pp. 1659-1660, Sep 2 1993.

[94]   K. Sugden, *et al.*, "Chirped Gratings Produced in Photosensitive Optical Fibers by Fiber Deformation during Exposure," *Electronics Letters,* vol. 30, pp. 440-442, Mar 3 1994.

[95]   K. Zhou, *et al.*, "Side detection of strong radiation-mode out-coupling from blazed FBGs in single-mode and multimode fibers," *IEEE Photonics Technology Letters,* vol. 15, pp. 936-938, Jul 2003.

[96]   K. O. Hill, *et al.*, "Birefringent Photosensitivity in Monomode Optical Fiber - Application to External Writing of Rocking Filters," *Electronics Letters,* vol. 27, pp. 1548-1550, Aug 15 1991.

[97]   D. C. Johnson, *et al.*, "Long-Length, Long-Period Rocking Filters Fabricated from Conventional Monomode Telecommunications Optical Fiber," *Optics Letters,* vol. 17, pp. 1635-1637, Nov 15 1992.

[98]   F. Bilodeau, *et al.*, "Efficient, narrowband LP01 LP02 mode convertors fabricated in photosensitive fibre: spectral response," *Electronics Letters,* vol. 27, pp. 682-684, 1991.

[99]   K. O. Hill, *et al.*, "Efficient Mode Conversion in Telecommunication Fiber Using Externally Written Gratings," *Electronics Letters,* vol. 26, pp. 1270-1272, Aug 2 1990.

[100]   R. Kashyap, *Fiber Bragg gratings*. San Diego ; London: Academic Press, 1999.

[101]   R. Kashyap, *et al.*, "Novel Method of Producing All-Fiber Photoinduced Chirped Gratings," *Electronics Letters,* vol. 30, pp. 996-998, Jun 9 1994.

[102]   J. Albert, *et al.*, "Apodization of the Spectral Response of Fiber Bragg Gratings Using a Phase Mask with Variable Diffraction Efficiency," *Electronics Letters,* vol. 31, pp. 222-223, Feb 2 1995.

[103]   J. Albert, *et al.*, "Moire phase masks for automatic pure apodisation of fibre Bragg gratings," *Electronics Letters,* vol. 32, pp. 2260-2261, Nov 21 1996.

[104] R. Kashyap*, et al.*, "Uv Written Reflection Grating Structures in Photosensitive Optical Fibers Using Phase-Shifted Phase Masks," *Electronics Letters,* vol. 30, pp. 1977-1978, Nov 10 1994.

[105] J. Canning and M. G. Sceats, "Pi-Phase-Shifted Periodic Distributed Structures in Optical Fibers by Uv Post-Processing," *Electronics Letters,* vol. 30, pp. 1344-1345, Aug 4 1994.

[106] L. Zhang*, et al.*, "Wide-Stopband Chirped Fiber Moire Grating Transmission Filters," *Electronics Letters,* vol. 31, pp. 477-479, Mar 16 1995.

[107] B. J. Eggleton*, et al.*, "Long Periodic Superstructure Bragg Gratings in Optical Fibers," *Electronics Letters,* vol. 30, pp. 1620-1622, Sep 15 1994.

[108] J. D. Prohaska*, et al.*, "Magnification of Mask Fabricated Fiber Bragg Gratings," *Electronics Letters,* vol. 29, pp. 1614-1615, Sep 2 1993.

[109] Q. Zhang*, et al.*, "Tuning Bragg Wavelength by Writing Gratings on Prestrained Fibers," *IEEE Photonics Technology Letters,* vol. 6, pp. 839-841, Jul 1994.

[110] A. D. Kersey*, et al.*, "Fiber grating sensors," *Journal of Lightwave Technology,* vol. 15, pp. 1442-1463, Aug 1997.

[111] V. Bhatia and A. M. Vengsarkar, "Optical fiber long-period grating sensors," *Optics Letters,* vol. 21, pp. 692-694, May 1 1996.

[112] V. Bhatia, "Applications of long-period gratings to single and multi-parameter sensing," *Optics Express,* vol. 4, pp. 457-466, May 24 1999.

[113] X. W. Shu*, et al.*, "Sampled fiber Bragg grating for simultaneous refractive-index and temperature measurement," *Optics Letters,* vol. 26, pp. 774-776, Jun 1 2001.

[114] K. M. Zhou, *et al.*, "Low thermal sensitivity grating devices based on Ex-45 degrees tilting structure capable of forward-propagating cladding modes coupling," *Journal of Lightwave Technology,* vol. 24, pp. 5087-5094, Dec 2006.

[115] X. F. Chen, *et al.*, "Real-time detection of DNA interactions with long-period fiber-grating-based biosensor," *Optics Letters,* vol. 32, pp. 2541-2543, Sep 1 2007.

[116] H. S. Jang, *et al.*, "Sensitive DNA biosensor based on a long-period grating formed on the side-polished fiber surface," *Optics Express,* vol. 17, pp. 3855-3860, Mar 2 2009.

[117] T. Allsop, *et al.*, "Application of long-period-grating sensors to respiratory plethysmography," *Journal of Biomedical Optics,* vol. 12, p. 064003, Nov-Dec 2007.

[118] T. Allsop, *et al.*, "Application of long-period grating sensors to respiratory function monitoring," *Smart Medical and Biomedical Sensor Technology Ii,* vol. 5588, pp. 148-156, 2004.

[119] G. Wehrle, *et al.*, "Fibre optic Bragg grating strain sensor used to monitor the respiratory spectrum," *14th International Conference on Optical Fiber Sensors,* vol. 4185, pp. 310-313, 2000.

[120] X. G. Qiao and M. Fiddy, "Distributed optical fiber Bragg grating sensor for simultaneous measurement of pressure and temperature in the oil and gas downhole," *Active and Passive Optical Components for Wdm Communications Ii,* vol. 4870, pp. 554-558, 2002.

[121] X. D. Zhang, *et al.*, "Pressure and temperature sensing system based on fiber-optic Bragg gratings for the oil and gas downhole," *APOC 2003: Asia-Pacific Optical and Wireless Communications; Optical Fibers and Passive Components,* vol. 5279, pp. 636-640, 2003.

[122] P. LoPresti, *et al.*, "Characterization of a differential fiber Bragg grating sensor for oil-water boundary detection," *Isa Transactions,* vol. 44, pp. 3-13, Jan 2005.

[123] R. C. Kamikawachi, *et al.*, "Thermal characterization of etched FBG for applications in oil and gas sector," *2007 Sbmo/Ieee Mtt-S International Microwave and Optoelectronics Conference, Vols 1 and 2,* pp. 280-283, 2007.

[124] G. Fusiek, *et al.*, "Design of a highly accurate optical sensor system for pressure and temperature monitoring in oil wells," *I2mtc: 2009 IEEE Instrumentation & Measurement Technology Conference, Vols 1-3,* pp. 555-559, 2009.

[125] J. R. Casas and P. J. S. Cruz, "Fiber Optic Sensors for Bridge Monitoring," *Journal of Bridge Engineering,* vol. 8, pp. 362-373, Nov-Dec 2003.

[126] C. Wang, *et al.*, "Construction control of mass concrete of Nanjing 3rd Yangtze bridge using FRP-packaged FBG sensors," *17th International Conference on Optical Fibre Sensors, Pts 1 and 2,* vol. 5855, pp. 1012-1015, 2005.

[127] L. Ren, *et al.*, "Application of FBG sensors in rolled concrete dam model - art. no. 617436," *Smart Structures and Materials 2006: Sensors and Smart Structures Technologies for Civil, Mechanical , and Aerospace Systems, Pts 1 and 2,* vol. 6174, pp. 17436-17436, 2006.

[128] H. H. Zhu, *et al.*, "Monitoring Internal Displacements of a Model Dam Using FBG Sensing Bars," *Advances in Structural Engineering,* vol. 13, pp. 249-261, Apr 2010.

[129] Y. M. Gebremichael, *et al.*, "A field deployable, multiplexed Bragg grating sensor system used in an extensive highway bridge monitoring evaluation tests," *IEEE Sensors Journal,* vol. 5, pp. 510-519, Jun 2005.

[130] H. L. Bao*, et al.*, "Temperature-insensitive FBG tilt sensor with a large measurement range," *Optics Communications,* vol. 283, pp. 968-970, Mar 15 2010.

[131] H. J. Chen*, et al.*, "Temperature-insensitive fiber Bragg grating tilt sensor," *Applied Optics,* vol. 47, pp. 556-560, Feb 1 2008.

[132] B. O. Guan*, et al.*, "Temperature-independent fiber Bragg grating tilt sensor," *IEEE Photonics Technology Letters,* vol. 16, pp. 224-226, Jan 2004.

[133] B. J. Peng*, et al.*, "Tilt sensor with FBG technology and matched FBG demodulating method," *IEEE Sensors Journal,* vol. 6, pp. 63-66, Feb 2006.

[134] L. Y. Shao and J. Albert, "Compact fiber-optic vector inclinometer," *Optics Letters,* vol. 35, pp. 1034-1036, Apr 1 2010.

[135] J. Wang*, et al.*, "Strain and tilt measurement using multi-point diffraction strain sensor," *Optics and Laser Technology,* vol. 40, pp. 1099-1103, Nov 2008.

[136] Y. Zhao*, et al.*, "Experimental research on a novel fiber-optic cantilever-type inclinometer," *Optics and Laser Technology,* vol. 37, pp. 555-559, Oct 2005.

[137] E. Brinkmeyer*, et al.*, "Fiber Bragg Reflector for Mode Selection and Line-Narrowing of Injection-Lasers," *Electronics Letters,* vol. 22, pp. 134-135, Jan 30 1986.

[138] J. L. Zyskind*, et al.*, "Short Single Frequency Erbium-Doped Fiber Laser," *Electronics Letters,* vol. 28, pp. 1385-1387, Jul 16 1992.

[139] Y. Mizrahi*, et al.*, "Stable Single-Mode Erbium Fiber-Grating Laser for Digital-Communication," *Journal of Lightwave Technology,* vol. 11, pp. 2021-2025, Dec 1993.

[140] W. H. Loh and R. I. Laming, "1.55-Mu-M Phase-Shifted Distributed-Feedback Fiber Laser," *Electronics Letters,* vol. 31, pp. 1440-1442, Aug 17 1995.

[141] M. Sejka*, et al.*, "Distributed-Feedback Er3+-Doped Fiber Laser," *Electronics Letters,* vol. 31, pp. 1445-1446, Aug 17 1995.

[142] D. Pureur*, et al.*, "Single-Polarization Fiber Lasers Using Bragg Gratings in Hi-Bi Fibers," *Journal of Lightwave Technology,* vol. 13, pp. 350-355, Mar 1995.

[143] R. P. Davey*, et al.*, "Mode-Locked Erbium Fiber Laser with Wavelength Selection by Means of Fiber Bragg Grating Reflector," *Electronics Letters,* vol. 27, pp. 2087-2088, Oct 24 1991.

[144] M. E. Fermann*, et al.*, "High-Power Soliton Fiber Laser-Based on Pulse-Width Control with Chirped Fiber Bragg Gratings," *Optics Letters,* vol. 20, pp. 172-174, Jan 15 1995.

[145] P. N. Kean*, et al.*, "Dispersion-Modified Actively Modelocked Erbium Fiber Laser Using a Chirped Fiber Grating," *Electronics Letters,* vol. 30, pp. 2133-2135, Dec 8 1994.

[146] G. A. Ball and W. W. Morey, "Efficient Integrated Nd3+ Fiber Laser," *IEEE Photonics Technology Letters,* vol. 3, pp. 1077-1078, Dec 1991.

[147] J. Y. Allain*, et al.*, "Ytterbium-Doped Silica Fiber Laser with Intracore Bragg Gratings Operating at 1.02 Mu-M," *Electronics Letters,* vol. 29, pp. 309-310, Feb 4 1993.

[148] M. Douay*, et al.*, "Birefringence Effect of Optical Fiber Laser with Intracore Fiber Bragg Grating," *IEEE Photonics Technology Letters,* vol. 4, pp. 844-846, Aug 1992.

[149] J. T. Kringlebotn*, et al.*, "Highly-Efficient, Low-Noise Grating-Feedback Er3+Yb3+ Codoped Fiber Laser," *Electronics Letters,* vol. 30, pp. 972-973, Jun 9 1994.

[150] D. U. Noske*, et al.*, "Dual-Wavelength Operation of a Passively Mode-Locked Figure-of-8 Ytterbium-Erbium Fiber Soliton Laser," *Optics Communications,* vol. 108, pp. 297-301, Jun 1 1994.

[151] J. T. Kringlebotn*, et al.*, "Er3+Yb3+ Codoped Fiber Distributed-Feedback Laser," *Optics Letters,* vol. 19, pp. 2101-2103, Dec 15 1994.

[152] S. Boj*, et al.*, "High-Efficiency Diode-Pumped Thulium-Doped Silica Fiber Lasers with Intracore Bragg Gratings in the 1.9-2.1-Mu-M-Band," *Electronics Letters,* vol. 30, pp. 1019-1020, Jun 23 1994.

[153] J. Alonso and E. Bernabeu, "A method for the measurement of the refractive index of dielectric cylinders," *Pure and Applied Optics,* vol. 6, pp. 147-152, Mar 1997.

[154] A. E.Siegman, *Lasers*: University Science Books, U.S, 1990.

[155] P. Lu*, et al.*, "Polarization mode dispersion and polarization dependent loss for a pulse in single-mode fibers," *Journal of Lightwave Technology,* vol. 19, pp. 856-860, Jun 2001.

[156] W. X. Xie*, et al.*, "2nd-Order Diffraction Efficiency of Bragg Gratings Written Within Germanosilicate Fibers," *Optics Communications,* vol. 101, pp. 85-91, Aug 1993.

[157] G. P. Brady*, et al.*, "Simultaneous measurement of strain and temperature using the first- and second-order diffraction wavelengths of Bragg gratings," *IEE Proceedings-Optoelectronics,* vol. 144, pp. 156-161, Jun 1997.

[158] A. Carballar, *et al.*, "Second-order fiber gratings," in *2004 IEEE LEOS Annual Meeting Conference Proceedings, Vols 1 and 2*, ed New York: Ieee, 2004, pp. 719-720.

[159] W. W. Morey, *et al.*, "Mode-Coupling Characteristics of Uv-Written Bragg Gratings in Depressed-Cladding Fiber," *Electronics Letters,* vol. 30, pp. 730-732, Apr 28 1994.

[160] S. J. Hewlett, *et al.*, "Coupling characteristics of photo-induced Bragg gratings in depressed- and matched-cladding fibre," *Optical and Quantum Electronics,* vol. 28, pp. 1641-1654, Nov 1996.

[161] C. Caucheteur, *et al.*, "Use of weakly tilted fiber Bragg gratings for strain sensing purposes," *Proc. of IEEE/LEOS Benelux Chapter, Eindhoven,* pp. 61-64, 2006.

[162] T. Guo, *et al.*, "Non-uniform-tilt-modulated fiber Bragg grating for temperature-immune micro-displacement measurement," *Measurement Science & Technology,* vol. 20, p. 034007, Mar 2009.

[163] B. O. Guan, *et al.*, "Simultaneous strain and temperature measurement using a single fibre Bragg grating," *Electronics Letters,* vol. 36, pp. 1018-1019, Jun 8 2000.

[164] K. Kieu, *et al.*, "Sub-100 fs pulses at watt-level powers from a dissipative-soliton fiber laser," *Optics Letters,* vol. 34, pp. 593-595, Mar 1 2009.

[165] T. Y. Fan, "Laser beam combining for high-power, high-radiance sources," *IEEE Journal of Selected Topics in Quantum Electronics,* vol. 11, pp. 567-577, May-Jun 2005.

[166] S. W. James and R. P. Tatam, "Optical fibre long-period grating sensors: characteristics and application," *Measurement Science and Technology,* vol. 14, pp. R49-R61, 2003.

[167] M. J.F.Digonnet, *Rare-Earth-Doped Fiber Lasers and Amplifiers*, 2nd ed.: Marcel Dekker Inc., 2002.

[168] J. L. Wagener*, et al.*, "A mueller matrix formalism for modeling polarization effects in erbium-doped fiber," *Journal of Lightwave Technology,* vol. 16, pp. 200-206, Feb 1998.

[169] J. T. Lin and W. A. Gambling, "Polarisation effects in fibre lasers: phenomena, theory and applications," *Fiber Laser Sources and Amplifiers II,* vol. 1373, pp. 42-43, 1990.

[170] A. S. Kurkov*, et al.*, "Fibre laser with an intracavity polariser based on a long-period fibre grating," *Quantum Electronics,* vol. 31, pp. 421-423, May 2001.

[171] F. C. McNeillie*, et al.*, "Highly polarized photonic crystal fiber laser," *Optics Express,* vol. 12, pp. 3981-3987, Aug 2004.

[172] M. Delgado-Pinar*, et al.*, "Linearly polarized all-fiber laser using a short section of highly polarizing microstructured fiber," *Laser Physics Letters,* vol. 5, pp. 135-138, Feb 2008.

[173] Y. W. Song*, et al.*, "40-nm-wide tunable fiber ring laser with single-mode operation using a highly stretchable FBG," *IEEE Photonics Technology Letters,* vol. 13, pp. 1167-1169, Nov 2001.

[174] S. Yamashita and K. Hotate, "Multiwavelength erbium-doped fibre laser using intracavity etalon and cooled by liquid nitrogen," *Electronics Letters,* vol. 32, pp. 1298-1299, Jul 1996.

[175] K. J. Zhou*, et al.*, "Room-temperature multiwavelength erbium-doped fiber ring laser employing sinusoidal phase-modulation feedback," *Optics Letters,* vol. 28, pp. 893-895, Jun 2003.

[176] S. L. Pan*, et al.*, "Switchable single-longitudinal-mode dual-wavelength erbium-doped fiber ring laser incorporating a semiconductor optical amplifier," *Optics Letters,* vol. 33, pp. 764-766, Apr 2008.

[177] Y. Yao*, et al.*, "Dual-wavelength erbium-doped fiber laser with a simple linear cavity and its application in microwave generation," *IEEE Photonics Technology Letters,* vol. 18, pp. 187-189, Jan-Feb 2006.

[178] X. M. Liu and C. Lu, "Self-stabilizing effect of four-wave mixing and its applications on multiwavelength erbium-doped fiber lasers," *IEEE Photonics Technology Letters,* vol. 17, pp. 2541-2543, Dec 2005.

[179] Y. G. Han*, et al.*, "Wavelength-spacing tunable multi wavelength erbium-doped fiber laser based on four-wave mixing of dispersion-shifted fiber," *Optics Letters,* vol. 31, pp. 697-699, Mar 2006.

[180] S. L. Pan*, et al.*, "Multiwavelength erbium-doped fiber laser based on inhomogeneous loss mechanism by use of a highly nonlinear fiber and a Fabry-Perot filter," *Optics Express,* vol. 14, pp. 1113-1118, Feb 2006.

[181] D. Liu*, et al.*, "A dual-wavelength fiber laser sensor system for measurement of temperature and strain," *IEEE Photonics Technology Letters,* vol. 19, pp. 1148-1150, Jul-Aug 2007.

[182] Z. Y. Liu*, et al.*, "Switchable triple-wavelength erbium-doped fiber laser using a single fiber Bragg grating in polarization-maintaining fiber," *Optics Communications,* vol. 279, pp. 168-172, Nov 2007.

[183] L. Sun*, et al.*, "Beating frequency tunable dual-wavelength erbium-doped fiber laser with one fiber bragg grating," *IEEE Photonics Technology Letters,* vol. 16, pp. 1453-1455, Jun 2004.

[184] O. Svelto, *Principles of Lasers*, 4th ed.: Springer, 1998.

[185] K. Tamura*, et al.*, "Self-Starting Additive Pulse Mode-Locked Erbium Fiber Ring Laser," *Electronics Letters,* vol. 28, pp. 2226-2228, Nov 19 1992.

[186] M. E. Fermann*, et al.*, "Passive-Mode Locking by Using Nonlinear Polarization Evolution in a Polarization-Maintaining Erbium-Doped Fiber," *Optics Letters,* vol. 18, pp. 894-896, Jun 1 1993.

[187] H. A. Haus*, et al.*, "Additive-Pulse Modelocking in Fiber Lasers," *Ieee Journal of Quantum Electronics,* vol. 30, pp. 200-208, Jan 1994.

[188] I. N. Duling, "All-Fiber Ring Soliton Laser Mode-Locked with a Nonlinear Mirror," *Optics Letters,* vol. 16, pp. 539-541, Apr 15 1991.

[189] A. G. Bulushev*, et al.*, "Passive-Mode Locking of a Laser with a Nonlinear Fiber Reflector," *Optics Letters,* vol. 15, pp. 968-970, Sep 1 1990.

[190] U. Keller*, et al.*, "Semiconductor saturable absorber mirrors (SESAM's) for femtosecond to nanosecond pulse generation in solid-state lasers," *IEEE Journal of Selected Topics in Quantum Electronics,* vol. 2, pp. 435-453, Sep 1996.

[191] F. X. Kartner*, et al.*, "Mode-locking with slow and fast saturable absorbers - What's the difference?," *IEEE Journal of Selected Topics in Quantum Electronics,* vol. 4, pp. 159-168, Mar-Apr 1998.

[192] U. Keller, "Recent developments in compact ultrafast lasers," *Nature,* vol. 424, pp. 831-838, Aug 14 2003.

[193] A. G. Rozhin*, et al.*, "Sub-200-fs pulsed erbium-doped fiber laser using a carbon nanotube-polyvinylalcohol mode locker," *Applied Physics Letters,* vol. 88, p. 051118, Jan 30 2006.

[194] K. Kieu and M. Mansuripur, "Femtosecond laser pulse generation with a fiber taper embedded in carbon nanotube/polymer composite," *Optics Letters,* vol. 32, pp. 2242-2244, Aug 1 2007.

[195]   F. Shohda, *et al.*, "A passively mode-locked femtosecond soliton fiber laser at 1.5 mu m with a CNT-doped polycarbonate saturable absorber," *Optics Express,* vol. 16, pp. 21191-21198, Dec 22 2008.

[196]   A. Y. a. P. Yeh, *Photonics: Optical Electronics in Modern Communications*: Oxford Unveristy Press, 2006.

[197]   C. B. Mou, *et al.*, "Characterization of 45 degrees-tilted fiber grating and its polarization function in fiber ring laser," *Journal of the Optical Society of America B-Optical Physics,* vol. 26, pp. 1905-1911, Oct 2009.

[198]   A. Chong, *et al.*, "All-normal-dispersion femtosecond fiber laser," *Optics Express,* vol. 14, pp. 10095-10100, Oct 16 2006.

[199]   A. Chong, *et al.*, "All-normal-dispersion femtosecond fiber laser with pulse energy above 20 nJ," *Optics Letters,* vol. 32, pp. 2408-2410, Aug 15 2007.

[200]   Y. Cheng, *et al.*, "Stable single-requency travelling-wave fibre loop laser with integral saturable-absorber based tracking narrow-band-filter," *Optics Letters,* vol. 20, pp. 875-877, Apr 1995.

[201]   X. F. Chen, *et al.*, "Single-longitudinal-mode fiber ring laser employing an equivalent phase-shifted fiber Bragg grating," *IEEE Photonics Technology Letters,* vol. 17, pp. 1390-1392, Jul 2005.

[202]   E. Chehura, *et al.*, "Temperature and strain discrimination using a single tilted fibre Bragg grating," *Optics Communications,* vol. 275, pp. 344-347, Jul 15 2007.

[203]   L. Y. Shao, *et al.*, "Directional Bend Sensor Based on Re-Grown Tilted Fiber Bragg Grating," *Journal of Lightwave Technology,* vol. 28, pp. 2681-2687, Sep 2010.

[204] X. F. Chen*, et al.*, "Optical chemsensor based on etched tilted Bragg grating structures in multimode fiber," *Ieee Photonics Technology Letters,* vol. 17, pp. 864-866, Apr 2005.

[205] C. F. Chan*, et al.*, "Optical fiber refractometer using narrowband cladding-mode resonance shifts," *Applied Optics,* vol. 46, pp. 1142-1149, Mar 1 2007.

[206] T. Guo*, et al.*, "Reflective tilted fiber Bragg grating refractometer based on strong cladding to core recoupling," *Optics Express,* vol. 17, pp. 5736-5742, Mar 2009.

[207] Y. Y. Shevchenko and J. Albert, "Plasmon resonances in gold-coated tilted fiber Bragg gratings," *Optics Letters,* vol. 32, pp. 211-213, Feb 1 2007.

[208] T. Allsop*, et al.*, "Generation off infared surface plasmon resonances with high refractive index sensitivity utilizing tilted fiber Bragg grafings," *Applied Optics,* vol. 46, pp. 5456-5460, Aug 1 2007.

[209] R. Suo*, et al.*, "800 nm WDM interrogation system for strain, temperature, and refractive index sensing based on tilted fiber Bragg grating," *Ieee Sensors Journal,* vol. 8, pp. 1273-1279, Jul-Aug 2008.

[210] B. W. Northway*, et al.*, "Liquid-Level Sensors Using Thin-Walled Cylinders Vibrating in Circumferential Modes," *Measurement Science & Technology,* vol. 6, pp. 85-93, Jan 1995.

[211] F. Toth*, et al.*, "A new capacitive precision liquid-level sensor," in *Precision Electromagnetic Measurements*, 1996, pp. 356-357.

[212] S. F. Knowles*, et al.*, "Multiple microbending optical-fibre sensors for measurement of fuel quantity in aircraft fuel tanks," *Sensors and Actuators a-Physical,* vol. 68, pp. 320-323, Jun 15 1998.

[213] T. Guo, *et al.*, "Temperature-insensitive fiber Bragg grating liquid-level sensor based on bending cantilever beam," *Ieee Photonics Technology Letters,* vol. 17, pp. 2400-2402, Nov 2005.

[214] B. Dong, *et al.*, "Liquid-level sensor with a high-birefringence-fiber loop mirror," *Applied Optics,* vol. 45, pp. 7767-7771, Oct 20 2006.

[215] T. Lu and S. P. Yang, "Extrinsic Fabry-Perot cavity optical fiber liquid-level sensor," *Applied Optics,* vol. 46, pp. 3682-3687, Jun 20 2007.

[216] P. Raatikainen, *et al.*, "Fiber-optic liquid-level sensor," *Sensors and Actuators a-Physical,* vol. 58, pp. 93-97, Feb 1997.

[217] I. K. Ilev and R. W. Waynant, "All-fiber-optic sensor for liquid level measurement," *Review of Scientific Instruments,* vol. 70, pp. 2551-2554, May 1999.

[218] F. Perez-Ocon, *et al.*, "Fiber-optic liquid-level continuous gauge," *Sensors and Actuators a-Physical,* vol. 125, pp. 124-132, Jan 10 2006.

[219] S. Khaliq, *et al.*, "Fiber-optic liquid-level sensor using a long-period grating," *Optics Letters,* vol. 26, pp. 1224-1226, Aug 15 2001.

[220] V. Lemarquand, "Synthesis study of magnetic torque sensors," *Ieee Transactions on Magnetics,* vol. 35, pp. 4503-4510, Nov 1999.

[221] L. A. Wang, *et al.*, "A torsion sensor made of a corrugated long period fibre grating," *Measurement Science & Technology,* vol. 12, pp. 793-799, Jul 2001.

[222] Y. P. Wang and Y. J. Rao, "Long period fibre grating torsion sensor measuring twist rate and determining twist direction simultaneously," *Electronics Letters,* vol. 40, pp. 164-166, Feb 5 2004.

[223] S. H. Yun, *et al.*, "Interrogation of fiber grating sensor arrays with a wavelength-swept fiber laser," *Optics Letters,* vol. 23, pp. 843-845, Jun 1 1998.

[224] G. A. Johnson*, et al.*, "Fiber Bragg grating interrogation and multiplexing with a 3 x 3 coupler and a scanning filter," *Journal of Lightwave Technology,* vol. 18, pp. 1101-1105, Aug 2000.

[225] S. Abad*, et al.*, "Interrogation of wavelength, multiplexed fiber Bragg gratings using spectral filtering and amplitude-to-phase optical conversion," *Journal of Lightwave Technology,* vol. 21, pp. 127-131, Jan 2003.

[226] R. W. Fallon*, et al.*, "All-fibre optical sensing system: Bragg grating sensor interrogated by a long-period grating," *Measurement Science & Technology,* vol. 9, pp. 1969-1973, Dec 1998.

[227] G. A. Ball*, et al.*, "Single Tone Polarimetric Bragg Grating Fiber Laser Sensor," *Leos '93 Conference Proceedings,* pp. 712-713832, 1993.

[228] J. Mandal*, et al.*, "Bragg grating-based fiber-optic laser probe for temperature sensing," *Ieee Photonics Technology Letters,* vol. 16, pp. 218-220, Jan 2004.

[229] S. Kim*, et al.*, "Multiplexed strain sensor using fiber grating-tuned fiber laser with a semiconductor optical amplifier," *Ieee Photonics Technology Letters,* vol. 13, pp. 350-351, Apr 2001.

[230] X. F. Yang*, et al.*, "Fiber Bragg grating strain sensor based on fiber laser," *Optics Communications,* vol. 271, pp. 203-206, Mar 1 2007.

[231] R. B. Wagreich*, et al.*, "Effects of diametric load on fibre Bragg gratings fabricated in low birefringent fibre," *Electronics Letters,* vol. 32, pp. 1223-1224, Jun 20 1996.

[232] I. Abe*, et al.*, "Superimposed Bragg gratings in high-birefringence fibre optics: three-parameter simultaneous measurements," *Measurement Science & Technology,* vol. 15, pp. 1453-1457, Aug 2004.

[233] L. Zhang*, et al.*, "Design and realization of long-period grating devices in conventional and high birefringence fibers and their novel applications as

fiber-optic load sensors," *Ieee Journal of Selected Topics in Quantum Electronics,* vol. 5, pp. 1373-1378, Sep-Oct 1999.

[234] M. Silva-Lopez*, et al.*, "Transverse load and orientation measurement with multicore fiber Bragg gratings," *Applied Optics,* vol. 44, pp. 6890-6897, Nov 10 2005.

[235] R. Suo*, et al.*, "In-fibre directional transverse loading sensor based on excessively tilted fibre Bragg gratings," *Measurement Science & Technology,* vol. 20, Mar 2009.

[236] A. M. Smith, "Single-mode fiber pressure sensitivity," *Electronics Letters,* vol. 16, pp. 773-774, 1980.

Appendix

This section shows the detailed information on the fibres used for the work of this thesis.

    1.   Standard single mode fibre

Product code	SMF 28	Manufacture	Corning Inc.
Cutoff wavelength	≤1260 nm	Core Diameter	8.2 µm
Mode Field Diameter	@1550 nm, 10.4 ±0.8µm	Cladding Diameter	125 ±1 µm
Attenuation	@1150, <1 dB/km	Coating Diameter	245± 5 µm
Numerical Aperture	0.14		

    2.   Photosensitive single mode fibre

Product code	PS1250/1500	Manufacture	Fibercore Ltd
cutoff wavelength	< 1260 nm	Core Diameter	N/A
Mode Field Diameter	@1550 nm,9.6 µm	Cladding Diameter	125 ±1 µm
Attenuation	@1550 nm,120 dB/km	Coating Diameter	245± 5% µm
Numerical Aperture	0.12 - 0.14		

    3.   Polarisation maintaining fibre-PM125L

Product code	552 HPWR 037	Manufacture	OFS Specialty Photonics Division
cutoff wavelength	1024 nm	Core Diameter	7.5 µm
Mode Field Diameter	@1060 nm, 7.7µm	Cladding Diameter	125 µm
Attenuation	@1150, <1 dB/km	Coating Diameter	247 µm
Birefringence	$4.3 \times 10\text{-}4$		
Numerical Aperture	0.11		

4. Polarisation maintaining fibre-Truephase 980

Product code	#F9920-01	Manufacture	OFS Specialty Photonics Division
cutoff wavelength	<970 nm	Core Diameter	4.8 µm
Mode Field Diameter	@980 nm, 6.6±1.0µm	Cladding Diameter	125±1.0µm
Attenuation	@980nm, 1.32 dB/km	Coating Diameter	250±10µm
Beat Length	@980 nm, ≤2.8 mm		
Numerical Aperture	0.13		